Network Effect in Geocentre Motion

Umma Jamila Zannat

February 2019

A thesis submitted for the degree of
Doctor of Philosophy of
The Australian National University

Statement of Originality

The work contained in this thesis is my own original research. No part of it has been submitted, or is being submitted, for any other degree. To the best of my knowledge, all sources used and any guidance received in preparation of this thesis have been duly acknowledged.

Umma Jamila Zannat

February 2019

Acknowledgements

First of all, I would like to express my gratitude to my supervisory panel. I am grateful to Dr. Paul Tregoning for giving me the opportunity to study under his supervision, for navigating me through the daze of postgraduate research, and for believing in me. I also thank Dr. Simon McClusky, Dr. Achraf Koulali, and Dr. Herb McQueen for their constant support, help and guidance. It was a pleasure and an honour working with the team for the past few years.

I would also like to thank the administrative team here at the ANU for their enthusiastic support. Especially, I am indebted to Maree Coldrick for always being there for me. I also sincerely thank Jochen Brocks for his moral support during a difficult time for me.

My immensely enjoyable time at the Research School of Earth Sciences was a gift from my fellow students and colleagues that I will cherish forever. I am grateful for the friendship of Sebastian Allgeyer, Evan Gowan, Siyuan Tian, Veronika Emetc, Bianca Kallenberg, Salim Masoumi, and Michael Moore. I would turn to Anthony Purcell whenever I needed help with my mathematics, and I was also fortunate enough to attend a statistics course by Malcolm Sambridge that was instrumental to this work.

Finally, I am thankful for the love and the encouragement from my family: my parents, my husband, and my little angel Bongo.

Abstract

Geocentre motion is the motion of the centre of mass of the Earth system with respect to the geometric centre of figure of the solid Earth surface because of the continual deformation of the Earth by geophysical processes. This motion is important both in theory and in practice to understand and interpret various mass transport phenomena and their consequences, such as sea level rise, postseismic relaxation, polar ice melting, and glacial isostatic adjustment.

Global reference frames for space geodetic point positioning are realised using measurements of the relative motion between satellites orbiting around the centre of mass on one hand and stations placed on the Earth's surface on the other. Therefore, reliable modelling of the geocentre motion is vital for the stability and the accuracy of these reference frames. In turn, the interpretation of many geodynamical quantities of current interest, such as the mean sea level, depends heavily on the quality of the adopted reference frame.

Space geodetic measurement of the true geocentre motion, however, is difficult due to the discrete and therefore incomplete sampling of the Earth's surface by geodetic stations. In other words, there is a discrepancy between the centre of figure of the Earth surface and the centre of network of the stations, called the network effect, arising from the sampling bias of the geodetic network.

In this work, we develop a method to estimate the magnitude of the network effect for a network of a given size N. For a given crustal deformation model, we consider the Helmert parameters of transformation, that is, the parameters characterising a Euclidean similarity transformation, between the centre of figure frames before and after the deformation event. Our proposed estimate for the network effect, which we call the 'expected bias', is the standard deviations of the changes in these parameters by the event as measured by a random network of

the size N. We show that, in accordance with probability theory, the expected bias scales as $1/\sqrt{N}$, and we provide an explicit formula for this estimate in terms of the vector spherical harmonics expansion of the displacement field.

We assess the effectiveness of the expected bias as an estimate of the network effect by simulating the displacement fields for two illustrative geodynamical processes: (instantaneous) coseismic deformation due to great earthquakes, and (time-dependent) elastic deformation due to surface water movements. We accordingly concentrate on the instantaneous changes and the secular drifts in the Helmert parameters for the two cases respectively.

We found that, in both case studies, the network effect is often as large as the changes in the Helmert parameters themselves. Hence, current space geodetic networks are indeed inadequate for verifying the geocentre motion predictions by geophysical models accurately. Nevertheless, our simulations validate the expected bias to be a reasonable estimate of the network effect.

Finally, we propose an alternative definition of the centre of network frame that assigns a weight proportional to the area a station represents to its measurements. We show that it can significantly reduce the network effect and improve the detection of geocentre motion in most cases.

Contents

List of Publications

The bulk of the original research is contained in Chapters 3, 4 and 5. These results have been reported in:

- Zannat, U. J., and P. Tregoning (2017a), Estimating network effect in geocenter motion: Theory, *Journal of Geophysical Research: Solid Earth*, *122*, doi: 10.1002/2017JB014246
- Zannat, U. J., and P. Tregoning (2017b), Estimating network effect in geocenter motion: Applications, *Journal of Geophysical Research: Solid Earth*, *122*, doi: 10.1002/2017JB014247

List of Figures

List of Tables

List of Abbreviations

CE	Centre of solid Earth
CF	Centre of Figure
CLT	Central Limit Theorem
CMB	Core-Mantle Boundary
CM	Centre of Mass
CMT	Centroid Moment Tensor
CN	Centre of Network
CSR	Center of Space Research
CWN	Centre of Weighted Network
DORIS	Doppler Orbitography and Radiopositioning Integrated by Satellite
ECCO	Estimating the Circulation and Climate of the Ocean
ECEF	Earth Centred, Earth Fixed
EOP	Earth Orientation Parameter
GC	Geocentre
GCMT	Global CMT Project
GGM03	GRACE Gravity Model 03
GGRF	Global Geodetic Reference Frame
GIA	Glacial Isostatic Adjustment
GNSS	Global Navigation Satellite Systems
GOCE	Gravity Field and Steady-State Ocean Circulation Explorer
GPS	Global Positioning System
GRACE	Gravity Recovery and Climate Experiment
GSM	GRACE Satellite-only Model
HP	Helmert Parameter
IAG	International Association of Geodesy

ICRF	International Celestial Reference Frame
ITRF	International Terrestrial Reference Frame
JPL	Jet Propulsion Laboratory
LLN	Law of Large Numbers
LOD	Length Of the Day
MSL	Mean Sea Level
NE	Network Effect
NNR	No-Net-Rotation
OMCT	Ocean Model for Circulation and Tides
OM	Ocean Model
PDMT	Present-Day surface Mass Trend
PODAAC	Physical Oceanography Distributed Active Archive Center
PREM	Preliminary Reference Earth Model
PSR	Post-Seismic Relaxation
RF	Reference Frame
RL05	Release-05
SA	Sumatra–Andaman
SLR	Satellite Laser Ranging
SOPAC	Scripps Orbit and Permanent Array Center
TO	Tōhoku–Oki
TRF	Terrestrial Reference Frame
TRS	Terrestrial Reference System
USGS	United States Geological Survey
VLBI	Very-Long-Baseline Interferometry

to my parents

Chapter 1

Introduction

It has been over half a century since we started sending artificial satellites into orbit around the Earth. These satellites have enabled exciting new technologies that revolutionised not only communication and navigation, but also the venerable science of geodesy. Today, with the help of a constellation of space geodetic satellites, we can monitor the geodynamical processes sculpting the Earth crust in near real-time.

These processes vary widely in their characteristic timescales. On one hand, oceanic and atmospheric tides deform the surface of the Earth on a subdaily basis. However, the mostly periodic motions they induce generally have much smaller drift components at larger timescales. On the other hand, in a few thousand years the viscoelastic response of the Earth to earthquakes and climate change becomes significant, Earth surface area is created and destroyed in volcanic activity and tectonic motion, and redistribution of mass on and inside the Earth crust changes the length of the day, to name just a few. Needless to say, modelling and predicting the shape of the Earth accurately over such a long period, if attempted, would be a truly formidable task.

Space geodetic measurements are carried out with respect to reference frames. Our focus in this thesis will be on reference frames that need to be stable over time intervals spanning decades. Therefore, we will primarily study the effect of disruptions to the secular linear motion of the points on the Earth surface at the decadal timescale. That is, we will assume that the higher-frequency processes (such as tidal loading) have already been modelled and taken into account. Likewise,

we will also assume that the influence of lower-frequency processes are already included in the secular motion during our period of interest.

Most importantly for this thesis, the overall motion of the crust, called the geocentre motion, due to these disruptions is only partially captured by the movements of the geodetic stations on Earth. That is, it is quite probable that due to the uneven geographical distribution of the stations, the average movement recorded by the stations will differ considerably from the true geocentre motion. This difference, called the "network effect", has implications for the realisation of global terrestrial reference frames from the position timeseries of these stations.

Our principle contribution in this thesis is a method to estimate the magnitude of the network effect. We will see that generally we expect the network effect to decrease when the number of stations on the Earth surface is increased. However, for the currently active network of geodetic stations around the world, we will also show that in some cases of interest the network effect may be as large in magnitude as the geocentre motion itself. Hence, the problem posed by the network effect persists in these cases even with the unprecedented coverage we have today. Consequently, it will have to be carefully addressed if we are to reconcile the geocentre motion predicted by geophysical theories with their space geodetic measurements at the millimetre (mm) level.

1.1 Space geodesy and the ITRF

One of the principal tasks of geodesy, measuring point positions and velocities on the Earth surface, requires a reference frame (RF) to enable us to report and interpret geospatial data. The RF establishes a one-to-one correspondence between points in space, which are physical, and their designated coordinates, which are numbers can be stored in a disk, processed by a computer, and transmitted over the Internet. A geodetic measurement site, in effect, acts as a label on one of the mass elements forming the Earth whose idealised motion as a point particle in space can then be described by its time-dependent coordinates.

In order to retain the identities of the locations on Earth surface, we need our RFs to remain attached to the Earth as it orbits around the Sun and spins around its axis. If the Earth were perfectly spherical and homogeneous, it would be

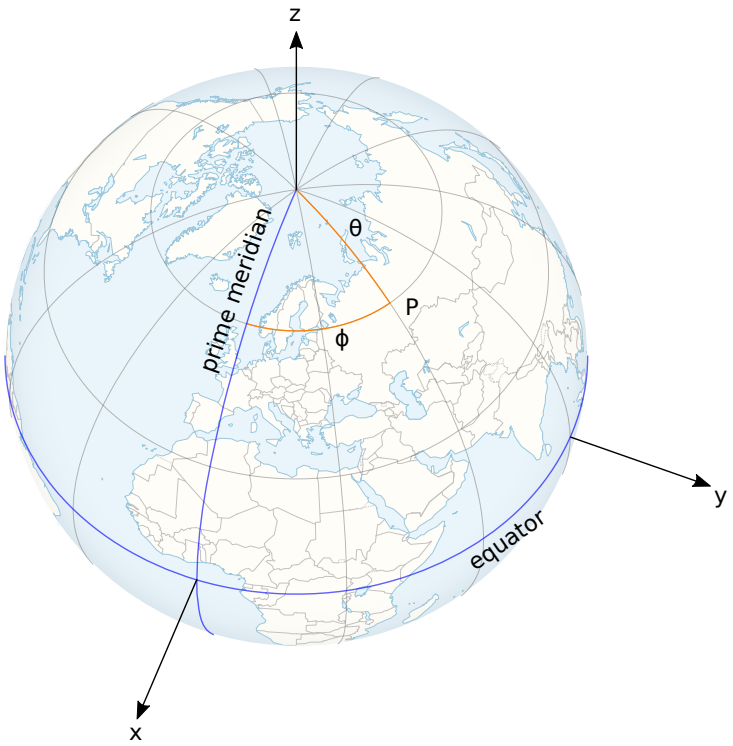

Figure 1.1: Geocentric coordinate systems for a spherical Earth: Cartesian and spherical. The angular coordinates θ and ϕ are the co-latitude and the longitude, respectively, of the point P. See Appendix A for our conventions.

natural to set up our coordinate system with the origin at its centre and to locate the points on the surface using angular coordinates (Figure 1.1). Our RF would then also rotate uniformly with the Earth around its axis. It would then enable us to assign reference coordinates to known locations, or stations, and to follow their motion in time as deviations from their reference positions. Even though our Earth is slightly ellipsoidal in reality, we continue to follow this program, making appropriate modifications to the concepts when necessary.

A useful characterisation for the centre of the real Earth is to imagine the entire mass of the planet to be condensed into that single point. This representation

of the Earth as a point particle, known as the Centre of Mass (CM) of the Earth system (solid Earth, oceans and atmosphere), moves under the influence of the Sun and other celestial objects, but is unaffected by processes internal to Earth. If we model and thereby remove the external influences from consideration, which we will assume to have been done already from now on, the CM moves at a constant velocity in a straight line through inertial space.

It is not difficult to show that the CM is not affected by internal geodynamical processes. For notational simplicity, consider the Earth to be a collection of N point particles where the kth particle has mass m_k and position $\mathbf{r}_k$ with respect to some inertial reference frame. Then the CM of the system is defined to be:

$$\mathbf{r}_{\mathrm{CM}} = \frac{\sum_k m_k \mathbf{r}_k}{\sum_k m_k} \tag{1.1}$$

Also, let the force that the jth particle exerts on the kth particle be denoted by $\mathbf{F}_{jk}$, so that the total force on the kth particle is $\sum_j \mathbf{F}_{jk}$, and by Newton's third law, $\mathbf{F}_{jk} = -\mathbf{F}_{kj}$. Differentiating Equation 1.1 twice with respect to time gives,

$$\frac{d^2}{dt^2}\mathbf{r}_{\mathrm{CM}} = \frac{\sum_k m_k \frac{d^2}{dt^2}\mathbf{r}_k}{\sum_k m_k} = \frac{\sum_{j,k} \mathbf{F}_{jk}}{\sum_k m_k} = \mathbf{0} \tag{1.2}$$

since opposing forces occur in pairs in the sum in the numerator. Thus the velocity of the CM is constant.

Since the CM moves uniformly with respect to some inertial RF, a non-rotating RF with the CM at the origin is itself inertial. A primary advantage of an inertial RF is that the laws of physics, such as the conservation of momentum, angular momentum, and energy, hold with respect to it. Note, however, that in reality the terrestrial frame rotates with the Earth and therefore is non-inertial. We sometimes refer to this rotating frame as the "Earth Centred, Earth Fixed" (ECEF) frame.

The arrival of various space geodetic techniques has brought about unprecedented improvements in the accuracy and the precision of global positioning and, consequently, of reference frames. The International Terrestrial Reference Frame (ITRF) [*Altamimi et al.*, 2002, 2007, 2011, 2016] is the standard ECEF RF mandated by the International Association of Geodesy (IAG) for communicating, comparing and combining geodetic data from different space geodesy analysis centres for

diverse Earth science applications. It is designed to draw from the strengths of the individual techniques, and to be reproducible, stable, accurate and accessible to the research communities worldwide. Its state-of-the-art accuracy and precision are maintained by the geodetic community by continual improvements to its measurements and methodology. For overviews of the infrastructure around the ITRF, see, for example, *Plag and Pearlman* [2009] and *Altamimi and Collilieux* [2013].

For its realisation, the ITRF uses combined measurements and observations from four space geodetic techniques: Satellite Laser Ranging (SLR), Very-Long-Baseline Interferometry (VLBI), Doppler Orbitography and Radiopositioning Integrated by Satellite (DORIS), and Global Navigation Satellite Systems (GNSS) such as the Global Positioning System (GPS). The unique characteristics of the different geodetic techniques are advantageous for measuring different ITRF parameters.

The ITRF takes its origin to be the time average of the SLR realisation of the CM over several decades of observations. SLR satellites here have the advantage of a mostly spherical design that enables their orbits to be modelled precisely over weeks. The orbit modelling for GPS is relatively less accurate since its satellites are subject to more complex non-gravitational forces due to their complex geometry [*Blewitt et al.*, 2010]. The spatio-temporal coverage of the Earth surface by GPS, on the other hand, is much denser. Moreover, GNSS binds the different techniques together through co-location ties between stations of different techniques at the same location [*Altamimi et al.*, 2011].

Since the space geodetic techniques employ several different methods to measure distances for positioning by trilateration, the ITRF also considers scale transformations between the RFs. The ITRF scale parameter is obtained by taking the average of the scale parameters of the SLR and the VLBI frames through stacking their observations together *Altamimi et al.* [2016].

VLBI uses signals from extra-galactic radio sources for the trilateration of its ground stations. Moreover, the equatorial coordinates of these distant stellar bodies, mainly quasars, are used to orient the Earth with respect to inertial space. That is, VLBI connects the ITRF to the International Celestial Reference Frame (ICRF) [*Ma et al.*, 1998], through the Earth Orientation Parameters (EOPs) that describe the Earth's polar motion (as observed principally by the GPS), and the universal time (typically UT1) [see, for example, *Rothacher et al.*, 1999].

DORIS has the most homogeneous station distribution but contributes less to the spatial resolution. GNSS, DORIS and SLR are used together in the ITRF to position the orbiting satellites.

1.2 Relevance of the ITRF to geophysical research

Earth observations from space have become integral to diverse aspects of our life ranging from weather forecast to public policy. Because of their global coverage and low latency, they provide us with vital, and potentially life-saving, timely information on meteorological and geological hazards such as cyclones, floods, earthquakes, volcano eruptions, wildfires, tsunamis, landslides, and subsidence.

Naturally, satellite observations also serve as invaluable sources of primary data to geophysics and geodesy. They have been instrumental to our evolving understanding of the complex interactions between the lithosphere, the hydrosphere, the cryosphere, and the atmosphere, as well as the mantle and the core. Space observations also provide critical validation, justification and constraints for the geodynamical models that codify this understanding.

Terrestrial RFs, however, are especially relevant to the analysis of global trends in mass transport processes over timespans of decades or even centuries. Unfortunately, the signals indicative of these trends are often embedded in much larger local variations (such as local hydrological loading). Moreover, these signals are, more often than not, of the order of parts-per-billion (ppb) when compared to the planetary scale. Understandably, satisfactory quantification of such tiny effects require staggeringly high quality measurements. Currently one of the principal factors limiting further understanding of phenomena such as mean sea level (MSL) rise, plate tectonics, anthropogenic land subsidence, present-day surface mass trend (PDMT), or polar ice melting is the uncertainty in the realisation of the RF itself, thanks to the impressive accuracy and resolution of modern satellite techniques [*Blewitt et al.*, 2010; *Wu et al.*, 2011].

On the other hand, given that these processes are of great significance in geophysics, and also are intimately related to politically contentious issues such as climate change, there is little room for errors and uncertainties. Since inaccuracies or discontinuities in the RF limit the quality of our interpretation of these phe-

nomena, it is imperative to realise a global terrestrial RF of the highest accuracy, precision and stability presently achievable. The ITRF is the embodiment of just such a concerted international effort.

Consider, as an example, the case of global sea level rise. Reliable and comprehensive historical records of sea level changes over the last century have been derived from measurements by tide gauges. Traditionally, a tide gauge measures the relative vertical movements of the ocean surface with respect to a horizontal reference level fixed to the land. The problem here, of course, is that for a mostly spherical planet like ours, the notion of a flat horizontal reference plane is only local, and cannot be extended to cover the whole planet so as to obtain a global measure of sea level change. It is more appropriate, in the global case, to measure the height of the sea surface from some fixed point at the planet's centre, which we may conveniently pick to be the origin of a geocentric reference system. Unfortunately, the interpretation of the mean sea level (MSL), and therefore, the MSL change, has now become inextricably tied to the choice of that reference frame, and our ability to realise it in practice [*Kovalevsky et al.*, 2012]. On the other hand, provided that we express all our observations in this frame, we can now collate and compare measurements from various sources, including those from space geodesy.

The MSL rise is especially interesting in that its determination involves all the "three pillars of geodesy" [*Rummel et al.*, 2005]:

geometry of the solid Earth, including ocean bottom, serves as a reference for measuring relative sea level changes

orientation of the Earth with respect to the celestial frame changes as a result of mass exchange between the oceans and the polar ice caps

gravity field due to the mass distribution of the Earth determines the shape of the geoid that the sea surface follows in static equilibrium

Space observations of the MSL accordingly involve not only satellite altimetry with missions such as TOPEX/Poseidon, Jason-1, Jason-2, and Jason-3, but also gravimetry missions such as the the Gravity Recovery and Climate Experiment (GRACE), and the Gravity Field and Steady-State Ocean Circulation Explorer (GOCE), in addition to the satellite techniques we have already introduced. The choice of RF here can

have a significant effect on the measurement of MSL [see, for example, *Beckley et al.*, 2007].

The ITRF thus provides a framework to connect and to combine the observational data and their analysis from different regions, different missions, different methods, and different decades consistently and meaningfully. Currently, the estimated uncertainty of the ITRF2014 origin is less than 3 mm and that of the origin velocity is less than 0.2 mm per year (yr) [*Altamimi et al.*, 2016]. For comparison, the resolutions of the altimetry- and gravimetry-based observations of sea level are also around that level [*Blewitt et al.*, 2010]. Clearly, the uncertainty in the RF realisation presents us with a road-block, among others, towards improving our measurements of changes in MSL. Incidentally, the precision of GPS measurements of point position of the sites stationed on the solid crust is believed to be much better at ∼1 mm, whereas the precision of the velocity is ∼1 mm/yr.

Using terrestrial as well as space measurements of sea level, *Collilieux and Wöppelmann* [2011] calculated the average MSL rise over the past century to be ∼1.6 mm/yr, for instance. Their analysis there also show that the uncertainty in the scale rate of the ITRF, currently estimated to be equivalent to 0.1 mm/yr, propagates directly into this estimate. In addition, up to 50% of the origin velocity uncertainty, currently estimated to be 0.2 mm/yr, also makes it into the uncertainty in the final result, depending on the network geometry. Note, however, that these recent uncertainty estimates are not too far from the requirement in *Blewitt et al.* [2010] of frame stability of 0.1 mm/yr and scale stability of the equivalent of 0.05 mm/yr spanning decades for reliable MSL change observations, owing to the rapid increase of accuracy of geodetic RFs by roughly an order of magnitude per decade since their introduction.

Besides, improving the stability of the ITRF is also important for providing tighter observational constraints and stricter validation for global climate models that predict MSL change. Additionally, the high quality and stability of the ITRF facilitates the identification and separation of different geophysical phenomena simultaneously at work. Its fields of practical applications include surveying, national geodetic datum definition, satellite navigation, and measurement of satellite orbits.

The pivotal role that the ITRF plays in current geophysical research has recently been recognised by the General Assembly of the United National in the form of

a resolution on the Global Geodetic Reference Frame (GGRF) for Sustainable Development[1] encouraging its adoption.

1.3 Realisation of the ITRF

It is sometimes useful to maintain a distinction between a terrestrial reference system (TRS) on one hand and a terrestrial reference frame (TRF) on the other. The TRS is an idealisation: a theoretical and mathematical construct that comprises of conventions for the origin and the orientation, physical units and constants, geodetic datum, and self-consistent modelling of the Earth's shape, rotation, and gravity [*Blewitt et al.*, 2010]. The TRF, however, is a concrete realisation of the TRS, specified by assigning position and velocity coordinates at a reference epoch to a set of globally distributed reference marks on the solid Earth's surface.

In practice, because of ongoing theoretical, methodological, and technological improvements, these assignments get upgraded with each new incarnation of the ITRF. There have been twelve such incarnations so far, starting from ITRF88 to the present ITRF2014. Considerable care is taken to ensure that discontinuities in the frame origin and alignment at the transition from one version to the next are as limited as possible.

The ITRF is currently derived from the station position timeseries of a global network of reference geodetic sites that nevertheless show non-linear motion from various loading phenomena or instrumental changes [see, for example, *Bevis and Brown*, 2014]. From a slightly different perspective, the presumed (piecewise) linearity of the station position timeseries in the realisation of the ITRF is, in reality, the result of the linearisation of a more general non-linear estimation problem [*Dermanis*, 2004].

In addition, the ITRF also relates the orientation parameters of the RF to polar motion and universal time EOPs in order to connect to the ICRF. Initially, the ITRF2000 adopted the no-net-rotation (NNR) condition for the orientation time evolution of the Earth's tectonic plates using the NNR-NUVEL-1A plate model [*Argus and Gordon*, 1991]. This entails aligning the RF with the so-called Tisserand frame that minimises the kinetic energy of the lithosphere and, as a consequence, the total

[1] http://www.un.org/ga/search/view_doc.asp?symbol=A/69/L.53

angular momentum of the crust in this RF becomes zero. Successive ITRF versions continued to inherit this alignment of the RF from their predecessors [*Altamimi et al.*, 2012].

Nevertheless, note that the RF parameters themselves are being defined only indirectly through the coordinates of geodetic sites, and thus the measurement of the point positions of the reference sites and the realisation of the RF are closely intertwined. Mathematically, RF realisation is a vastly over-specified problem that in general admits no exact solutions, only approximate ones. The number of unknown RF parameters here is only 14: 3 origin components, 1 scale factor, 3 orientation parameters, and their corresponding 7 time derivatives. In contrast, each of the more than a thousand reference sites contribute 6 equations, 3 for the position and 3 for the velocity components, at each epoch of observation for these parameters.

1.4 Impact of geophysical processes on the ITRF

The non-linear motion of the ground stations is caused by a complicated network of processes: tidal displacements, atmospheric loading, hydrological mass movements, earthquakes, plate tectonics, and even internal mass movements. Since the satellite observations of station positions are not fully compatible with the simple linear trajectory model that the ITRF realisation hypothesises, the RF realised from the reference sites in general undergoes what is referred to as RF deformation as a result of this motion. The resulting internal geometric inconsistency, in turn, damages the accuracy of positioning of the non-reference geodetic sites as well. Imperfections in our modelling of satellite orbits or satellite signal propagation also contribute to this inconsistency.

We discuss here two geodynamical processes whose consequences can be observed from space: coseismic deformation due to great earthquakes with moment magnitude $M_W \geq 8.0$ and elastic deformation due to surface water loading. In Chapters 4 and 5 respectively, they will serve as two qualitatively different case studies for the methods of estimating the network effect that we will introduce in Chapter 3.

In *Altamimi et al.* [2016], it was reported that taking these two processes into account, alongside a few others, can vastly improve the quality of the reference

frame. Still, the impact of imperfections in our modelling of crustal deformation, satellite orbits, or satellite signal propagation on the ITRF continues to be the focus of active research. In fact, *Altamimi et al.* [2016] found that published geophysical models of crustal deformations, especially for postseismic relaxation, are unavailable in many cases, and are difficult to assess for quality for the purposes of RF construction in general, and settled for fitting parametric models to the observed timeseries instead.

1.4.1 Great earthquakes

Significant earthquakes leave their marks on the face of the Earth. Naturally, the elastic as well as the viscoelastic deformations of the Earth due to earthquakes have been the subject of studies for decades. Since, in general, the surface displacement gradually diminishes with distance from the epicentre, the far field signature of an earthquake is difficult to detect. However, great earthquakes like the Sumatra–Andaman earthquake in December 2004 or the Tōhoku–Oki earthquake in March 2011 are violent enough for the deformation to occur not only near the earthquake but all over the world. Again, thanks to the incredible resolution of modern space geodetic observation and analysis, it is now possible to measure this far field offset, despite it being in the mm order, systematically across the globe.

Great earthquakes are generally defined to be those with $M_W \geq 8.0$ and are somewhat rare. For instance, the United States Geological Survey (USGS)[2] lists 22 such earthquakes in this century. Considerable effort has been spent on modelling and analysing the Sumatra–Andaman earthquake [see, for example, *Ammon et al.*, 2005; *Fu and Sun*, 2006; *Han et al.*, 2006; *Panet et al.*, 2007], since it was the first great earthquake with $M_W \geq 9.0$ whose signals were observable by GPS technology and space gravity (Figure 1.2). Geodetic data show that there was a coherent surface motion roughly directed towards the earthquake rupture as far as 4500 km away from the epicentre, with measurable static coseismic offsets greater than 1 mm up to 7800 km away [see, for instance, *Banerjee et al.*, 2005; *Kreemer et al.*, 2006]. The Tōhoku–Oki earthquake, being just as devastating if not more, also

[2] https://earthquake.usgs.gov/earthquakes/search/

received significant attention [see, for example, *Nishimura et al.*, 2011; *Nettles et al.*, 2011; *Shestakov et al.*, 2012].

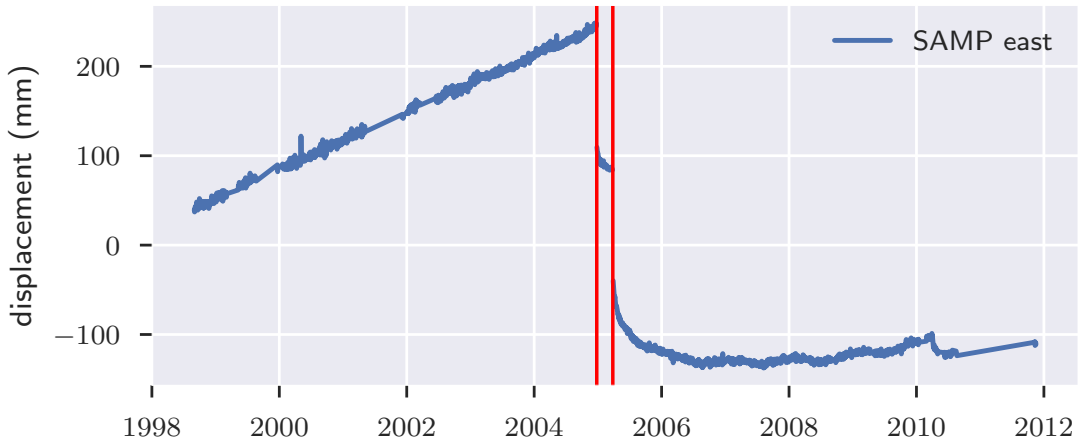

Figure 1.2: The east component of the position timeseries of the GPS station SAMP located at Sampali, Medan City, Indonesia. The red vertical lines mark the December 2004 Sumatra–Andaman earthquake as well as the March 2005 Nias-–Simeulue earthquake where coseismic discontinuities can be seen. Non-linear postseismic rebound signals are also visible here. The GLOBK [*Herring et al.*, 2002] processed timeseries shown here is from *Bock and Webb* [2012, SOPAC archive].

The potential of the great earthquakes to cause measurable displacements of every geodetic station on Earth, including in particular the reference stations, poses a serious challenge to the integrity of the ITRF. It is not immediately obvious in this case how to calculate the coseismic offsets in the first place without the "fixed" far field [*Kreemer et al.*, 2006]. Also, since the space geodetic technique with the best spatial resolution, GPS, is less sensitive to the CM than it is to the shape of its network, an overall movement of the whole network with respect to the CM is difficult to measure accurately with GPS. We will come back to this issue of GPS measurement of the geocentre motion momentarily in Section 1.5. Nevertheless, due to the global nature of the disruption, the time-dependent reference coordinates in the ITRF would ideally have to be recalibrated after each great earthquake [*Blewitt et al.*, 2010].

In practice, unmodelled far field deformations accumulate into site velocity er-

rors that may reach up to ∼0.2–0.4 mm/yr. Furthermore, the sustained postseismic relaxation considerably far into the plates obfuscates plate boundaries, and contradicts the assumption of linearity of the velocity of the plates in the implementation of the NNR condition [*Tregoning et al.*, 2013].

We are primarily interested in coseismic displacements in this thesis as an example process that we may model to be instantaneous. That is, we will ignore the viscoelastic properties of the mantle, and therefore its postseismic response, and concentrate solely on the Earth's elasticity here.

Because of the global scale, the traditional dislocation theories in an elastic homogeneous half-space, such as *Okada* [1985], are not sufficient here. Instead, radially heterogeneous spherical Earth models, such as *Pollitz* [1996], have proved to be valuable in modelling far field coseismic offsets. Failing to take into account the layered structure, along with the curvature, that is, the sphericity, of the Earth can introduce up to 25% error in the static displacement calculated in the far field [*Fu and Sun*, 2006; *Banerjee et al.*, 2005].

There are, of course, other interesting effects that are not captured by the instantaneous surface displacement field. In general, earthquakes tend to deform the Earth towards a less oblate shape [*Chao and Gross*, 1987]. For instance, the Sumatra–Andaman earthquake is calculated to have reduced the oblateness of the Earth by $\sim 2 \times 10^{-11}$, a subtle signal but nevertheless possibly measurable by space geodesy. It is also estimated to have decreased the length of a day by ∼7 milliseconds (ms), and shifted the pole of rotation by ∼2 milli-arc-seconds (mas) [*Gross and Chao*, 2006].

1.4.2 Water movements and GRACE

The station position timeseries of the geodetic stations on the ground often show prominent seasonal signals, in particular in the vertical component (Figure 1.3). These signals provide us with valuable information about their sources, including changes in the hydrological and the atmospheric loading of the Earth. Being quasi-periodic, their impact on the reference coordinates of the position and the velocity of the ITRF reference stations, calculated by averaging over many cycles, is not too drastic in general, despite their centimetre (cm) scale amplitudes. However, they

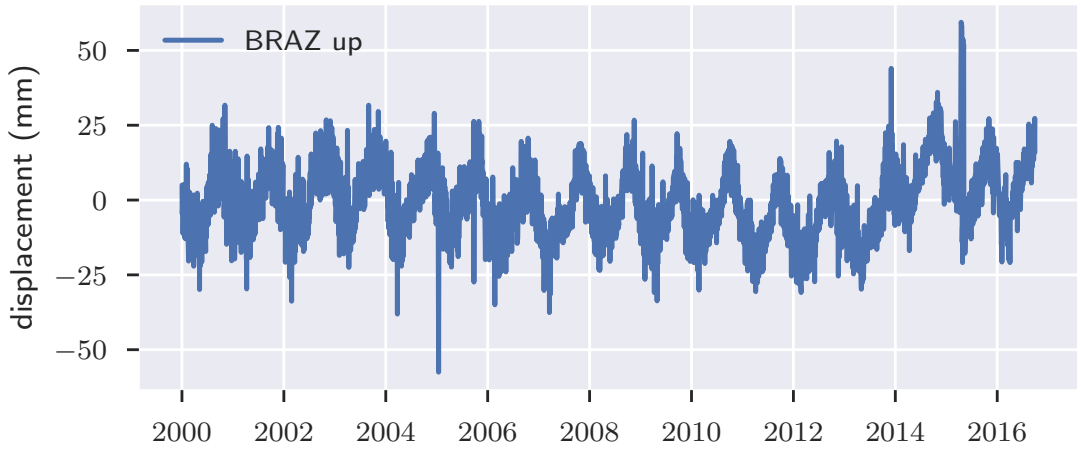

Figure 1.3: The vertical component of the position timeseries of the GPS station BRAZ. The quasi-periodic signal here comes mostly from the Earth's elastic response to the seasonal water mass movement in and out of the Amazon river basin. The GLOBK [*Herring et al.*, 2002] processed timeseries shown here is from *Bock and Webb* [2012, SOPAC archive].

still need to be understood and systematically accounted for to ensure mm-level accuracy, precision and stability of the ITRF [see, for example, *Collilieux et al.*, 2010].

A truly enormous amount of surface water gets moved around seasonally. To support its massive weight, the Earth undergoes elastic deformation that is measurable by satellite geodesy. For stations in regions of high hydrological activity such as river basins, or in areas with significant anthropogenic water mass movement, the displacements of the sites caused by the loading can be particularly significant. Fortunately, satellite gravimetry allows us to independently track movements of hydrological mass, in the forms of surface water, groundwater, ice or snow, by measuring the time-variable gravity field it creates. We can then deduce the contribution of the Earth's elastic response to the weight of the redistributed water, assuming the rheology of the Earth is known, to the seasonal signals in the station position timeseries.

The Gravity Recovery And Climate Experiment (GRACE) [*Tapley et al.*, 2004] has been monitoring the Earth's gravity field for more than 15 years since its launch

in 2002. It has been instrumental in studying and analysing long-term trends in the water cycle over the years because of its ability to detect mass variations of cm-level equivalent water heights. Its geospatial resolution, ~400 km, is however somewhat coarse. Nevertheless, the elastic deformation corresponding to the mass movements observed by GRACE correlates well with GPS site position measurements [*Tregoning et al.*, 2009; *Zou et al.*, 2014].

Hence, in this thesis, we will adopt the time-variability of the mass distribution of the Earth, as seen by GRACE, as our model for surface water movement that serves as our illustrative case study of a continuous process deforming the Earth surface. Note, however, that in theory, the integrity of the RF suffers from neither the periodic component nor the linear trend in the station position timeseries, but is deteriorated only by non-linear trends that may result from, for instance, local water or oil extraction, or viscoelastic glacial isostatic adjustment (GIA).

1.5 Geocentre motion

The choice of the CM as the origin of our RF, as attractive as it is in theory, has a serious problem: being buried at the centre of the Earth, the CM is not physically accessible. We can "sense" the CM though via its gravitational influence. For example, it is possible to deduce its location from the orbits of the SLR satellites as they revolve around it.

Technologically advanced signal transmitters or receivers placed firmly on the Earth surface have been continually operating for decades. Naturally, space measurements of the positions of the ground stations, complemented by high-precision land survey at the co-location ties, can often be more accurate than the CM realisation, although site-specific errors can also introduce large biases [*Moore et al.*, 2014]. In fact, since GPS is a differential technique, it can determine the internal geometry of its network polyhedron even better [*Bevis and Brown*, 2014]. Here, the internal geometry of the network is specified by the set of distances between the stations that are independent of the RF.

Therefore, a critical part of ensuring the accuracy of an RF realisation is positioning and orienting the geodetic network polyhedron in inertial space precisely (Figure 1.4). But, from our perspective, it is perhaps more natural to approach the

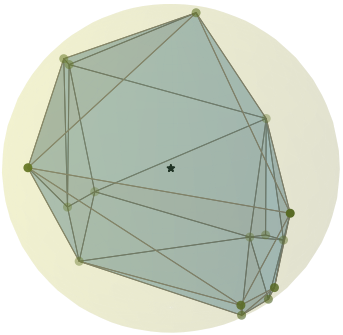

Figure 1.4: Schematic diagram of the network polyhedron of the geodetic stations (green dots) and the Centre of Mass (black star). The network polyhedron may be viewed as an approximation of the solid Earth surface (filled circle).

problem the other way around, and to try to locate and orient the CM frame with respect to the network. In this context, the CM is often referred to as the geocentre (GC), and hence, we are interested here in the precise determination of GC motion.

However, this network-dependent version of GC motion is theoretically rather inconvenient. In order to make contact with surface deformation models, for example, we need to characterise the GC motion in terms of the surface geometry alone, without references to specific networks. One such characterisation would be as the motion of the GC with respect to the entire surface of the solid Earth. The geodetic observation of the CM motion with respect to the network could then be viewed as the realisation of this theoretical construct, since the solid Earth surface is closely approximated by the surface of the network polyhedron.

But the surface of the Earth is not rigid, making it troublesome to interpret this characterisation in practice. We can circumvent this technical difficulty by introducing the Centre of Figure (CF) of the solid Earth surface [*Trupin et al.*, 1992; *Dong et al.*, 1997]:

$$\mathbf{r}_{\mathrm{CF}} = \frac{1}{4\pi} \int_{\partial \oplus} \mathbf{r}'(\theta, \phi)\, d\Omega \tag{1.3}$$

Here, we have identified a point on the surface by its spherical coordinates (θ, ϕ) on the perfectly spherical undeformed Earth, and $\mathbf{r}'$ is its actual measured position on the deformed Earth. Mathematically, we have adopted the Lagrangian description

from continuum mechanics. The Earth surface is here denoted by $\partial\oplus$, and $d\Omega = \sin\theta\, d\theta\, d\phi$ is the differential solid angle. The GC motion can be then defined as the motion of the CM with respect to the CF frame [see, for example, *Wu et al.*, 2012]. Note that the CF frame, in general, is not inertial.

GC motion is a key quantity of interest in geophysics in its own right because it signifies mass redistribution at the planetary scale. As such, careful measurements of GC motion can validate or constrain models of mass transport phenomena such as ocean and groundwater circulation, glaciation, or postseismic relaxation.

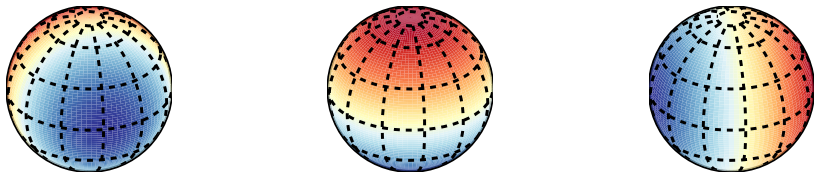

Figure 1.5: The three linearly independent modes of the (real, as opposed to complex) degree-1 spherical harmonics. Here, m denotes the order of spherical harmonics. The colours red and blue signify positive and negative values of the functions, respectively. Linear combinations of these three functions can express net transport across any plane that divides the sphere into equal halves.

Mathematically, GC motion is given by the degree-1 components of the spherical harmonic decomposition of the surface displacement field. For surface water movements, the GC motion is the response to the corresponding degree-1 component of the surface water density that characterises a net transport of water from one hemisphere to the other (Figure 1.5), for instance. Part of the GC motion in this case results from the rigid translation of the solid Earth because of the recoil it experiences due to this net water transfer, and the rest may be attributed to the elastic deformation of the surface due to the loading of the redistributed water.

In the coseismic deformation case, however, most of the mass movement takes place inside the Earth. Another subtlety in this case is that, even though the variations in the degree-1 modes are hemisphere-scale, the displacement field that produces a significant GC motion may itself be quite localised. We will return to

the special role of the degree-1 spherical harmonics in the theory of GC motion in Section 2.4.

Naturally, an error in the GC motion measurement translates to a hemisphere-scale correlated errors in the height of sea level [see, for instance, *Beckley et al.*, 2007; *Melachroinos et al.*, 2013]. The impact of such an error on MSL becomes particularly significant if it happens to be roughly orthogonal to the nodal plane of the degree-1 component of the ocean function[3], that is, the plane that divides the Earth into two equal halves with the highest discrepancy in the oceanic areas.

Because of its special relationship with the inertial frame, the algorithm to calculate the degree-1 components of the displacement field predicted by a crustal deformation model often differs from the one to calculate the higher degrees. Regrettably, popular implementations often omit this exceptional case for simplicity [*Xu and Chao*, 2015]. For example, ITRF2014, in a commendable attempt at incorporating models of non-linear station motions into the ITRF, adopted the analytical formulae in *Okada* [1985] to model coseismic crustal deformation. But, being a half-space model, it not only fails to account for the sphericity of the Earth, it is completely unable to predict GC motion due to earthquakes.

Some space techniques (such as SLR) are more sensitive to the CM than others (such as VLBI). Accurate determination of the GC motion helps, alongside co-location ties, to bind them together and to link them to satellite orbits. In particular, understanding GC motion is crucial for maintaining the stability of the RF over several decades. In addition, the precision of the GC measurement is a robust system performance indicator for space geodetic systems [*Crétaux et al.*, 2002; *Moore and Wang*, 2003; *Kang et al.*, 2009].

Finally, we note that practical space geodetic measurement of GC motion has been difficult so far. Currently, it is hard to distinguish the SLR realisation of the GC motion from the background noise [*Collilieux et al.*, 2009]. One of the principal hindrances here is the strong network effect of the relatively sparse SLR network. We, therefore, turn to the network effect next.

[3] the function that takes the value 1 on the oceans and the value 0 on the continents

1.6 Network effect in geocentre motion measurements

We may view the GC motion, defined as the motion of the CM with respect to the figure of the solid Earth, as the physical quantity we want to measure. From this point of view, the motion of the CM with respect to the geodetic station network is a measurement, or a realisation, of the true GC motion. We will call the "error" in this measurement, that is, the discrepancy between the theoretical value of the GC motion and its practical measurement, the network effect (NE).

Just as we did in the last section, we get around the complications of defining motion with respect to a deforming network here by finding a point representative of the network called the Centre of Network (CN). As will be discussed further in Chapter 3, it turns out that there are several distinct sensible definitions for CN. Perhaps the simplest one is the average of the positions of the stations [see, for example, *Wu et al.*, 2012],

$$\mathbf{r}_{\mathrm{CN}} = \frac{1}{N}\sum_{k=1}^{N}\mathbf{r}'_k \tag{1.4}$$

Here, N is the number of stations in the network, and $\mathbf{r}'_k$ is the position of the kth station on the deformed Earth. The theoretical GC motion is then the motion of CM with respect to the CF frame, or, the CM–CF motion, whereas its measurement by a geodetic network is the motion of the CM with respect to the CN frame, or, the CM–CN motion. The network effect, in this case, would be the CN–CF motion.

We should clarify that the CM–CN motion is of considerable value for RF realisation since it specifies how to position and orient the network in inertial space. In fact, it may appear that the true GC motion, that is, the CM–CF motion, is irrelevant to RF realisation, since the positions of the points other than the stations are not being measured anyway. However, the TRF is merely a realisation of the TRS that is self-consistently defined through geophysical modelling of the whole Earth, which inevitably involves consideration of the true GC motion.

Moreover, the definition of NE is not universally agreed upon in the literature. For instance, while our usage here follows that in *Collilieux et al.* [2009], the usage

of the term in *Collilieux et al.* [2010] seems to align more closely to the CM–CN motion itself.

The network effect, as defined here, arises because the geodetic network only samples the total displacement field of the crustal deformation processes at discrete, isolated points. If we could uniformly cover the entire Earth surface with geodetic stations then there would be no network effect. The NE therefore characterises the sampling bias that the finite network introduces. Intuitively, an evenly distributed set of sites that covers the whole Earth, although discrete, would reduce this bias, and therefore, the NE, if the network is sufficiently dense.

In practice, it is often not feasible to set up a dense network with an even coverage of the Earth surface. Most of the surface of the Earth is covered by oceans with practically inaccessible floors. Furthermore, the southern hemisphere has a greater share of oceanic area than the northern hemisphere. Even the continents do not have the same level of spatial coverage due to geographical and economical constraints. Also, reliable RF realisation requires well-understood trajectory models for its sites, so stations close to active volcanoes or tectonically deforming zones are not too helpful here.

Of course, the relatively sparser geodetic networks such as SLR and VLBI suffer more from the network effect. Unfortunately these two networks also happen to contribute the most to the realisation of the ITRF origin and scale. Thus the possibility of unmodelled or poorly modelled CM–CN motion aliasing into site coordinates remains a risk to the integrity and the stability of the ITRF [*Wu et al.*, 2011].

An exact determination of the NE in magnitude and direction, in principle, would allow us to measure the true GC motion within the current precision of space geodesy. Nevertheless, merely constraining the magnitude of NE effectively, as we propose to do in this thesis, helps us compare the predictions of deformation models with geodetic observations. When the models contain unknown parameters, the constraints on the magnitude of NE in turn restricts the domain of possible values for those parameters.

Furthermore, where there are multiple geodetic networks involved, such as in the case of the ITRF, the CNs of different networks are not directly comparable, especially without some measure of the acceptable range of discrepancy. When

these CNs are viewed as realisations of the same CF, the estimated magnitudes of the NE can serve as such a measure. Since network configurations change from time to time, we may also need to compare the temporal variation of CNs of the same network.

Lastly, despite our presentation of the NE here as an error, depending on the use case, NE of measurable size may not necessarily be detrimental to RF realisation. A case in point is coseismic deformation where a network of sites in the far field may remain virtually unaffected by the earthquake. The network in this case, in fact, facilitates the reconstruction of the RF, even though the calculated NE here is practically the same as the true GC motion.

1.7 Thesis outline

In this chapter, we presented the broader context in which this research takes place. In Chapter 2, we outline the theoretical and mathematical background needed for the modelling of the geophysical processes that we consider in this thesis, and in Chapter 3 we develop methods for estimating the network effect in geocentre motion that results from these processes. In Chapters 4 and 5 we validate our approach by applying it to simulations of the example crustal deformation processes. Then in Chapter 6 we briefly document our implementation of the methods introduced here as algorithms to be executed on computers. Lastly, we summarise our findings and explore possible future directions for this research in Chapter 7.

Chapter 2

Background

Here we introduce some of the ideas and results that our work builds upon. The goal is to establish terminology and notation, to set up the theoretical framework needed to model the geophysical processes of interest, and to present the mathematical consequences of the physical considerations that play key roles.

2.1 Helmert parameters of coordinate transform

Consider the relationship between the position vectors $\mathbf{r}$ and $\mathbf{r}'$ of an arbitrary point with respect to two different Cartesian coordinate systems. There are two basic transformations that preserve the Euclidean distances between points,

$$\text{translation:} \quad \mathbf{r}' = \mathbf{r} + \mathbf{T} \tag{2.1a}$$

$$\text{rotation:} \quad \mathbf{r}' = \mathscr{O}\mathbf{r} \tag{2.1b}$$

and thus can be used to transform $\mathbf{r}$ to $\mathbf{r}'$. Here, $\mathbf{T}$ is an arbitrary vector and $\mathscr{O}$ represents an orthogonal matrix. Space geodetic techniques also consider an overall scale change,

$$\text{scaling:} \quad \mathbf{r}' = (1 + D)\mathbf{r} \tag{2.2}$$

When we include scaling, we are in effect considering Euclidean similarity transformations rather than just the rigid transformations. In general, the transformed coordinates depend on the order in which the three different transformations are carried out. However, when the transformations are infinitesimally close to the

identity transform, the error associated with the choice of order is even smaller and hence can be neglected. In this case, $\mathscr{O} = 1 + \mathscr{A}$ where $\mathscr{A}$ is an infinitesimal anti-symmetric matrix. Thus,

$$\mathbf{r}' = \mathbf{r} + \mathbf{T} + D\,\mathbf{r} + \mathscr{A}\mathbf{r} = \mathbf{r} + \mathbf{T} + D\,\mathbf{r} + \mathbf{R} \times \mathbf{r} \tag{2.3}$$

where $\mathbf{R}$ is the vector dual to the anti-symmetric matrix $\mathscr{A}$. The parameters $\mathbf{T}$, D, and $\mathbf{R}$ are the (instantaneous) Helmert parameters (HPs) of transformation between the two frames. Here, $\mathbf{T}$, D, $\mathbf{R}$, and the displacement $\mathbf{u} = \mathbf{r}' - \mathbf{r}$ experienced by the point under the transformation are all infinitesimals, or at least,

$$|\mathbf{T}| \ll |\mathbf{r}|, \quad |D| \ll 1, \quad |\mathbf{R}| \ll 1, \quad |\mathbf{u}| \ll |\mathbf{r}| \tag{2.4}$$

These conditions are well satisfied for the transformations between the reference frames of the different geodetic techniques, or the transformation between the undeformed and the deformed Centre of Figure (CF) frames that we consider next.

2.2 Shifts in Helmert parameters due to surface deformation

For simplicity, we will consider here the effect of an arbitrary crustal deformation process in isolation. Our simplified model starts with an undeformed Earth that is spherically stratified, non-rotating, elastic, and isotropic, usually abbreviated as the SNREI Earth in the literature [*Dahlen*, 1968, see, for example]. Thus, the CF frame initially coincides with the Centre of Mass (CM) frame. The process under consideration then deforms the surface of the Earth, creating a displacement field $\mathbf{u}(\mathbf{r})$, and consequently, the CF frame moves (Figure 2.1). As in Section 1.5, we will adhere to the Lagrangian description in which the position vector $\mathbf{r}$ refers to the position of the point on the undeformed Earth. Also, in the following, we will measure physical quantities, such as the displacement $\mathbf{u}$ here, with respect to the inertial CM frame unless indicated otherwise.

Since the CM frame does not move in inertial space due to the conservation of linear and angular momenta, we can describe the motion of the CF frame by the transformation from the unchanged CM frame to the altered CF frame. Thus, the

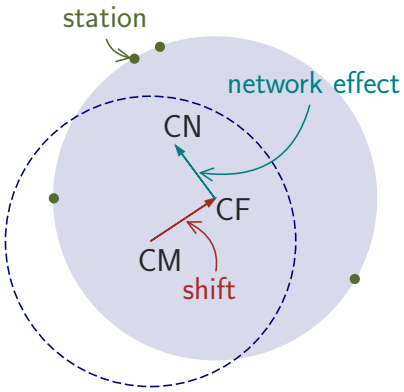

Figure 2.1: Schematic diagram of the shift in the CF frame parameters of the deformed Earth (filled circle) with respect to the CM frame of the total undeformed Earth system (dotted circle), and the accompanying network effect, that is, the difference between the CN of geodetic stations (green dots) and the CF. The GC motion is the negative of the shifts in the CF frame parameters.

deformation of the Earth surface results in shifts in HPs of transformation from the CM frame to the CF frame. When several different processes are active on an already deformed Earth surface, as is the actual case, the observed changes in the CF frame parameters may be thought of as the sum of the shifts due to each of the processes.

In order to find expressions for the translational parameters $\mathbf{T}_{\mathrm{CF}}$, the scale parameter D_{CF}, and the rotational parameters $\mathbf{R}_{\mathrm{CF}}$, we consider the displacement fields $\mathbf{v}$ that the corresponding transformations would induce on the undeformed Earth surface. That is, as before, we consider the corresponding fields for the three groups of parameters,

$$\mathbf{v}_T = \mathbf{T}_{\mathrm{CF}} \tag{2.5a}$$

$$\mathbf{v}_D = D_{\mathrm{CF}}\,\mathbf{r} \tag{2.5b}$$

$$\mathbf{v}_R = \mathbf{R}_{\mathrm{CF}} \times \mathbf{r} \tag{2.5c}$$

where $\mathbf{r}$ is the position vector drawn from the CM frame origin at the centre of the Earth. The goal is to approximate the original displacement field $\mathbf{u}$ with these fields as accurately as possible, or in other words, to minimise the overall error

$\int_{\partial\oplus}(\mathbf{u}-\mathbf{v})^2\,d\Omega$ in the transformed coordinates. The resulting expressions are,

$$\mathbf{T}_{\mathrm{CF}} = \frac{1}{4\pi}\int_{\partial\oplus}\mathbf{u}\,d\Omega \tag{2.6a}$$

$$D_{\mathrm{CF}} = \frac{1}{4\pi r_\oplus^2}\int_{\partial\oplus}\mathbf{r}\cdot\mathbf{u}\,d\Omega \tag{2.6b}$$

$$\mathbf{R}_{\mathrm{CF}} = \frac{3}{8\pi r_\oplus^2}\int_{\partial\oplus}\mathbf{r}\times\mathbf{u}\,d\Omega \tag{2.6c}$$

where $r_\oplus$ is the radius of the undeformed spherical Earth, $\partial\oplus$ denotes the Earth surface, and $d\Omega = \sin\theta\,d\theta\,d\phi$ is the differential solid angle. The first of these is essentially the definition of the CF [*Trupin et al.*, 1992], the third appears in *Zhou et al.* [2016] but, even though the derivation is straightforward, we have not come across the second in the literature yet.

For example, to derive the expressions for D_{CF}, we set

$$\frac{\partial}{\partial D_{\mathrm{CF}}}\int_{\partial\oplus}\left(\mathbf{u}-\mathbf{v}_D\right)^2 d\Omega = 0 \tag{2.7}$$

or,

$$\int_{\partial\oplus}\mathbf{u}\cdot\mathbf{r}\,d\Omega = \int_{\partial\oplus}\mathbf{v}_D\cdot\mathbf{r}\,d\Omega = D_{\mathrm{CF}}\int_{\partial\oplus}\mathbf{r}^2\,d\Omega = 4\pi\,r_\oplus^2\,D_{\mathrm{CF}} \tag{2.8}$$

The derivations for the other two are more involved and therefore we relegate them to Appendix B.2.

As we discussed in Section 1.5, the geocentre (GC) motion is traditionally defined to be the motion of the CM with respect to the CF. We can justify this choice by noting that, although in inertial space it is really the surface of the Earth (along with the geodetic stations on it) that moves, from our point of view it is the CM that appears to move with respect to the network of geodetic stations. Therefore, the GC motion due to a surface deformation is the opposite of the CF frame motion that we considered here.

As is schematically illustrated in Figure 2.1, the geodetic stations on the Earth surface also get displaced by a crustal deformation. However, because they sample the surface only discretely, the Centre of Network (CN) of the stations does not necessarily coincide with the CF, and consequently the network effect arises in the measurement of the GC motion.

2.3 Vector spherical harmonics decomposition

Any (square-integrable) vector field defined on and inside a sphere, such as the displacement field $\mathbf{u}$ in particular, can be expanded in terms of the vector spherical harmonics,

$$\mathbf{u} = \sum_{n=0}^{\infty} \sum_{m=-n}^{n} \mathbf{u}_{nm} \tag{2.9a}$$

$$\mathbf{u}_{nm} = \mathbf{u}^S_{nm} + \mathbf{u}^T_{nm} \tag{2.9b}$$

$$\mathbf{u}^S_{nm}(r,\theta,\phi) = y^S_{1,nm}(r)\,\mathbf{R}_{nm}(\theta,\phi) + y^S_{3,nm}(r)\,\mathbf{S}_{nm}(\theta,\phi) \tag{2.9c}$$

$$\mathbf{u}^T_{nm}(r,\theta,\phi) = y^T_{1,nm}(r)\,\mathbf{T}_{nm}(\theta,\phi) \tag{2.9d}$$

The field $\mathbf{u}_{nm}$ is referred to as the mode with degree n and order m. The components $\mathbf{u}^S_{nm}$ and $\mathbf{u}^T_{nm}$ are the spheroidal and toroidal parts of the $\mathbf{u}_{nm}$ mode respectively. The vector spherical harmonics themselves are

$$\mathbf{R}_{nm} = Y_{nm}\,\hat{\mathbf{r}} \tag{2.10a}$$

$$\mathbf{S}_{nm} = \frac{\partial Y_{nm}}{\partial\theta}\,\hat{\boldsymbol{\theta}} + \frac{1}{\sin\theta}\frac{\partial Y_{nm}}{\partial\phi}\,\hat{\boldsymbol{\phi}} = \nabla_1 Y_{nm} \tag{2.10b}$$

$$\mathbf{T}_{nm} = \frac{1}{\sin\theta}\frac{\partial Y_{nm}}{\partial\phi}\,\hat{\boldsymbol{\theta}} - \frac{\partial Y_{nm}}{\partial\theta}\,\hat{\boldsymbol{\phi}} = -\hat{\mathbf{r}}\times\nabla_1 Y_{nm} \tag{2.10c}$$

where the unit vectors $(\hat{\mathbf{r}}, \hat{\boldsymbol{\theta}}, \hat{\boldsymbol{\phi}})$ correspond to the spherical coordinates (r,θ,ϕ) (defined in Appendix A.1), $Y_{nm}(\theta,\phi)$ are the spherical harmonics (defined in Appendix A.2),

$$\nabla_1 = \hat{\boldsymbol{\theta}}\frac{\partial}{\partial\theta} + \hat{\boldsymbol{\phi}}\frac{1}{\sin\theta}\frac{\partial}{\partial\phi} \tag{2.11}$$

is the surface gradient operator on the surface of a sphere, and the normalisation and the orthogonality properties of the vector spherical harmonics are given in Appendix A.3. The radial functions $y^S_{1,nm}$, $y^S_{3,nm}$ and $y^T_{1,nm}$ are the coefficients that characterise $\mathbf{u}$ in this decomposition with respect to the basis consisting of the vector spherical harmonics in the space of (square-integrable) functions on the sphere. Since the displacement field $\mathbf{u}$ must be real, our conventions for the spherical harmonics imposes the relationships

$$y_{n,-m} = (-1)^m\, y^*_{nm} \tag{2.12}$$

for any of the y functions y_1^T, y_1^S, or y_3^S, where superscript $*$ denotes complex conjugation. The symbols $\mathbf{R}_{nm}$ and $\mathbf{T}_{nm}$ for the vector spherical harmonics are not to be confused with the symbols $\mathbf{R}_{\text{CF}}$ and $\mathbf{T}_{\text{CF}}$ for the Helmert parameters.

There are significant advantages to this decomposition for our purposes. Perhaps most importantly, since our model of the Earth is spherically stratified, the equations of motion for the physical processes we will consider are decoupled in this representation. That is, the task of solving the equations for the total field reduces to solving simpler equations for each mode independently of the others. In fact, for the systems we consider, these equations can further be separated into spheroidal and toroidal parts. Moreover, the characteristic length-scale of the details captured by a particular mode is given by its associated wavelength

$$\lambda_n = \frac{4\pi\, r_\oplus}{2n+1} \tag{2.13}$$

according to Jeans' formula [see, for example, *Tanimoto*, 1986]. Hence we can truncate the infinite sum on n in Equation 2.9 at the level of details we desire to get an approximate field that is still continuous as a function. On a more practical note, since the indices n and m are integers, the coefficients of this truncated expansion can be represented in the finite memory of a computer, possibly as an array.

2.4 Special role of degree-0 and degree-1 displacement fields

As far as transformations between the CM and the CF frames are concerned, the modes with $n \leq 1$ are special. Evidently, the unique $n = 0$ mode of the displacement field represents a uniform expansion or contraction, depending on the sign of the associated coefficient. Conversely, any overall scaling is represented only by the $n = 0$ mode since the other modes are orthogonal to it in the space of (square-integrable) vector fields on spheres. In other words, no mode with $n \neq 0$ can represent a global expansion or contraction.

Similarly, the $n = 1$ modes contain the uniform translations and the uniform rotations, and any global uniform translation or rotation must be represented by the $n = 1$ modes [*Farrell*, 1972]. There are three of these modes with $m \in \{-1, 0, 1\}$.

When we substitute the expansion in Equation 2.9 into Equation 2.6 for a displacement field $\mathbf{u}$ on the Earth surface $r = r_\oplus$, we obtain explicit formulae of the CF parameters in terms of the coefficients of the vector spherical harmonic expansion,

$$\mathbf{T}_{\mathrm{CF}} = \frac{1}{4\pi} \sum_{m=-1}^{1} \left(y^S_{1,1,m}(r_\oplus) + 2y^S_{3,1,m}(r_\oplus) \right) \boldsymbol{\Delta}_m \tag{2.14a}$$

$$D_{\mathrm{CF}} = \frac{1}{\sqrt{4\pi} r_\oplus} y^S_{1,00}(r_\oplus) \tag{2.14b}$$

$$\mathbf{R}_{\mathrm{CF}} = \frac{3}{8\pi r_\oplus} \sum_{m=-1}^{1} 2y^T_{1,1,m}(r_\oplus) \boldsymbol{\Delta}_m \tag{2.14c}$$

where the constant vectors $\boldsymbol{\Delta}_m$ are defined to be,

$$\boldsymbol{\Delta}_0 = \sqrt{\frac{4\pi}{3}}\, \hat{\mathbf{z}} \tag{2.15a}$$

$$\boldsymbol{\Delta}_1 = -\sqrt{\frac{2\pi}{3}}\, (\hat{\mathbf{x}} + i\hat{\mathbf{y}}) \tag{2.15b}$$

$$\boldsymbol{\Delta}_{-1} = -\boldsymbol{\Delta}_1^* = -\sqrt{\frac{2\pi}{3}}\, (-\hat{\mathbf{x}} + i\hat{\mathbf{y}}) \tag{2.15c}$$

Here, the standard Cartesian unit vectors $\hat{\mathbf{x}}$, $\hat{\mathbf{y}}$, and $\hat{\mathbf{z}}$ form a right-handed basis. Derivations of these formulae are presented in Appendix B.3. The exact expressions for $\boldsymbol{\Delta}_m$ depends on the normalisation used for the spherical harmonics, but they can also be characterised by the normalisation-independent relation

$$\hat{\mathbf{r}} = \sum_{m=-1}^{1} Y^*_{1,m}\, \boldsymbol{\Delta}_m \tag{2.16}$$

as discussed in Appendix B.1. It is interesting to note that only the degree-1 spheroidal modes contribute to the translation parameters and, likewise, only the degree-1 toroidal modes contribute to the rotation parameters, whereas only the degree-0 mode contributes to the scale parameter.

Since physical laws are independent of the reference frames used, the equations of motion, when formulated in a frame-independent manner, must be invariant under a global translation or rotation. That is, an active physical translation or

rotation of the whole system under consideration must be able to be re-interpreted as a passive change of the coordinate system instead. In our case studies, this freedom shows up as degeneracies in the associated equations. Therefore we have to supplement the equations of motion with additional external information.

For the physical cases we consider, it turns out that the physical requirement of the conservation of linear and angular momenta are precisely the needed supplements [*Okubo and Endo*, 1986]. However, these laws only hold in an inertial reference frame, and the only obvious inertial frame available to us is the CM frame. Consequently, all our calculations are carried out in the CM frame. In this frame, the conservation laws take the form [*Sun and Dong*, 2014],

$$\int_{\oplus} \rho\, \mathbf{u}\, dV = \mathbf{0} \tag{2.17a}$$

$$\int_{\oplus} \rho\, \mathbf{r} \times \mathbf{u}\, dV = \mathbf{0} \tag{2.17b}$$

Here, $\oplus$ denotes the Earth interior, $dV = r^2\, dr\, d\Omega$ is the differential volume element, and $\rho(r)$ is the density of the layered Earth. As we derive in Appendix B.4, these conditions reduce to [*Sun and Okubo*, 1993; *Xu and Chao*, 2015],

$$\int_0^{r_\oplus} \rho \left(y^S_{1,1,m} + 2y^S_{3,1,m} \right) r^2\, dr = 0 \tag{2.18a}$$

$$\int_0^{r_\oplus} \rho\, y^T_{1,1,m}\, r^3\, dr = 0 \tag{2.18b}$$

for $|m| \leq 1$, respectively, for the vector spherical harmonics expansion of the displacement field $\mathbf{u}$.

2.5 Theory of the elastic Earth

In Chapter 4, we will study the coseismic GC motion caused by earthquakes and the associated network effect. In this section we present a sketch of the physical theory that enables us to calculate the coseismic displacement field.

In reality, seismic sources have complicated dynamics and geometry, and are spread out over considerable area inside the Earth and sometimes on the Earth surface. We will, however, model them as dislocations along fault surfaces, and

simulate the Earth's elastic response to such dislocations. To be more precise, we will consider the source to be composed of infinitesimal flat fault planes, each acting as a point source, whose effects are to be integrated in order to obtain the total coseismic field.

Also, we will model the coseismic displacement field to appear instantly at a fixed moment in time. Of course, neither is the earthquake actually instantaneous nor does its influence propagate instantly everywhere on the Earth. In the GPS station position timeseries data, the coseismic displacements are often seen to take place over several minutes. Roughly though, we expect the discontinuities, or offsets, in the daily GPS timeseries at the day of the earthquake to correspond to our modelled coseismic displacements. The relatively slower process of postseismic relaxation should preferably also be taken into account when calculating the offsets [*Banerjee et al.*, 2005].

The dislocation theory of coseismic deformations was first developed for the half-space [*Steketee*, 1958; *Press*, 1965; *Mansinha and Smylie*, 1971; *Okada*, 1985], but was soon adopted to take Earth's sphericity into account [*Ben-Menahem et al.*, 1969; *Smylie and Mansinha*, 1971; *Wason and Singh*, 1972]. Despite their popularity, the half-space models are not adequate for our purpose of calculating the GC motion, since the infinite half-space is obviously infinitely massive. Our account of the theory here follows *Pollitz* [1992, 1996] in part, since our implementation is adopted from his program `STATIC1D`[1]. We augmented his code with the ability to calculate the degree-0 and the degree-1 modes crucial to the prediction of the CF frame parameters.

2.5.1 Equation of motion

Here we derive the displacement field for a point source following the Green's function approach. The continuum version of Newton's equation of motion, often called Cauchy's equation, is

$$\rho \frac{\partial^2 \mathbf{u}}{\partial t^2} = \mathbf{f} + \nabla \cdot \sigma \tag{2.19}$$

[1]available from `https://earthquake.usgs.gov/research/software/`

here, t denotes the time, ρ the density, σ the stress tensor, and $\mathbf{f}$ the body force density. The total moment tensor M for an arbitrary volume $\mathcal{V}$ in this case may be expressed as [see, for example, *Aki and Richards*, 2002, §3.4],

$$M = \int_{\mathcal{V}} \mathbf{f} \otimes \mathbf{r} \, dV \tag{2.20}$$

where $\otimes$ is the tensor product, that is, the dyadic product.

Static equilibrium is reached after the Earth responds elastically to the dislocation at the source, and hence the left hand side of Equation 2.19 is zero here. In the absence of gravity, the body force density is also zero everywhere except at the point source located at $\mathbf{r}_s$. Thus we re-write Equation 2.19 in the symbolic form [*Pollitz*, 1996],

$$\nabla \cdot \sigma = M \cdot \nabla \delta \left(\mathbf{r} - \mathbf{r}_s \right) \tag{2.21}$$

Here, M is the moment tensor at the source, ∇ is the vector differential operator, and δ is the Dirac delta. Fortunately, we will be able to incorporate the effect of the right hand side into the boundary conditions that we will consider later, rather than having to confront it directly. Hence for now, we consider the region where the right hand side of this equation is set to zero, that is, the whole Earth except the point source.

The most general linear constitutive relation between the stress and the strain for an elastic solid is often called the generalised Hooke's law. In component form, it reads,

$$\sigma_{ij} = \sum_{k,l} C_{ijkl} \, E_{kl} \tag{2.22}$$

Here, C is a tensor of elastic moduli,

$$E = \frac{1}{2} \left((\nabla \mathbf{u}) + (\nabla \mathbf{u})^T \right) \tag{2.23}$$

is the strain tensor, and superscript T denotes the transpose. Since σ and E are symmetric, the most general form that C can take for an isotropic material is [see, for example, *Ben-Menahem and Singh*, 2012, §1.3],

$$C_{ijkl} = \lambda \, \delta_{ij} \, \delta_{kl} + \mu \left(\delta_{ik} \, \delta_{jl} + \delta_{il} \, \delta_{jk} \right) \tag{2.24}$$

where λ and μ are known as the Lamé coefficients of the material. In component-free form, therefore,

$$\sigma = \lambda\,(\operatorname{tr} E)\,I + 2\mu\,E \tag{2.25}$$

Here, I is the identity tensor, and tr denotes the trace. Substituting these relations into the equation $\nabla \cdot \sigma = \mathbf{0}$ we get,

$$(\lambda + 2\mu)\nabla\,(\nabla \cdot \mathbf{u}) - \mu\nabla \times (\nabla \times \mathbf{u}) = \mathbf{0} \tag{2.26}$$

This equation, or its alternative form,

$$\alpha^2\,\nabla\,(\nabla \cdot \mathbf{u}) - \beta^2\,\nabla \times (\nabla \times \mathbf{u}) = \mathbf{0} \tag{2.27}$$

with $\alpha^2 = (\lambda + 2\mu)\,/\rho$ and $\beta^2 = \mu/\rho$, is known as (the static equilibrium version of) the Navier equation. It is customary to decompose the displacement vector field into an irrotational and a solenoidal part,

$$\mathbf{u} = \mathbf{u}_\alpha + \mathbf{u}_\beta, \qquad \nabla \times \mathbf{u}_\alpha = \mathbf{0}, \qquad \nabla \cdot \mathbf{u}_\beta = 0 \tag{2.28}$$

If they separately obey Laplace's equation,

$$\nabla^2 \mathbf{u}_\alpha = \mathbf{0}, \qquad \nabla^2 \mathbf{u}_\beta = \mathbf{0} \tag{2.29}$$

then the sum obeys the Navier equation.

In seismological terminology, $\mathbf{u}_\alpha$ and $\mathbf{u}_\beta$ correspond to P wave and S wave respectively. For a stratified Earth, however, the P wave mixes with the vertical component SV of the S wave. The horizontal component SH of S wave remains separate and is called the toroidal part, while the P–SV system is called the spheroidal part [see, for example, *Stein and Wysession*, 2009, §2.5.2]. We adopt this terminology for our static case as well. Conversely, reasonable solutions of the static Navier equation can always be separated into spheroidal and toroidal parts obeying Laplace's equation, but the proof is more involved [see, for example, *Aki and Richards*, 2002, §4.1.1].

We thus have a decomposition of the static coseismic field into a spheroidal part and a toroidal part, both of which are further decomposed into the vector spherical

harmonic modes. Similar to the displacement field in Equations 2.9c and 2.9d, we decompose the traction forces on the surface of the spherical shell at radius r,

$$\hat{\mathbf{r}} \cdot \sigma^S_{nm}(r,\theta,\phi) = y^S_{2,nm}(r)\,\mathbf{R}_{nm}(\theta,\phi) + y^S_{4,nm}(r)\,\mathbf{S}_{nm}(\theta,\phi) \tag{2.30a}$$

$$\hat{\mathbf{r}} \cdot \sigma^T_{nm}(r,\theta,\phi) = y^T_{2,nm}(r)\,\mathbf{T}_{nm}(\theta,\phi) \tag{2.30b}$$

When we express Equation 2.26 in spherical coordinates for each of these modes, we obtain a system of linear first-order ordinary differential equations for the y functions [*Takeuchi and Saito*, 1972, §II.C],

$$\frac{d\mathbf{y}_{nm}}{dr} = A_n\,\mathbf{y}_{nm} \tag{2.31}$$

where $\mathbf{y}^S_{nm} = [y^S_{1,nm} \quad y^S_{2,nm} \quad y^S_{3,nm} \quad y^S_{4,nm}]^T$ for the spheroidal modes, and similarly, $\mathbf{y}^T_{nm} = [y^T_{1,nm} \quad y^T_{2,nm}]^T$ for the toroidal modes, which explains our curious choice of subscripts for the y functions. Here, $A_n(r)$ are matrices that depend on the physical properties of the layered Earth. Because of our assumed spherical symmetry, the physical properties $\lambda(r)$ and $\mu(r)$, along with $\rho(r)$, are all functions of only the radius r of the shell. Also, note that the matrices A_n are independent of m due to a degeneracy that comes from the symmetries of the equations [*Gilbert and Dziewonski*, 1975; *Dahlen*, 1968].

Explicitly, the equations that we will refer to as the equations of motion from now on are,

$$\frac{d}{dr}\begin{bmatrix} y_1 \\ y_2 \\ y_3 \\ y_4 \end{bmatrix} = \begin{bmatrix} -\frac{2\lambda}{\sigma r} & \frac{1}{\sigma} & \frac{\lambda n(n+1)}{\sigma r} & 0 \\ \frac{4\gamma}{r^2} & \frac{2}{r}\left(\frac{\lambda}{\sigma}-1\right) & -\frac{2\gamma n(n+1)}{r^2} & \frac{n(n+1)}{r} \\ -\frac{1}{r} & 0 & \frac{1}{r} & \frac{1}{\mu} \\ -\frac{2\gamma}{r^2} & -\frac{\lambda}{\sigma r} & (\gamma+\mu)\frac{n(n+1)}{r^2} - \frac{2\mu}{r^2} & -\frac{3}{r} \end{bmatrix} \begin{bmatrix} y_1 \\ y_2 \\ y_3 \\ y_4 \end{bmatrix} \tag{2.32}$$

and

$$\frac{d}{dr}\begin{bmatrix} y_1 \\ y_2 \end{bmatrix} = \begin{bmatrix} \frac{1}{r} & \frac{1}{\mu} \\ \frac{\mu}{r^2}(n-1)(n+2) & -\frac{3}{r} \end{bmatrix} \begin{bmatrix} y_1 \\ y_2 \end{bmatrix} \tag{2.33}$$

for the spheroidal and the toroidal modes, respectively, where we have suppressed the superscripts S or T and subscripts n and m for clarity (see Appendices C.5 and C.4 for their respective derivations). Here,

$$\sigma = \lambda + 2\mu, \qquad \gamma = \lambda + \mu - \frac{\lambda^2}{\sigma} \tag{2.34}$$

are convenient elastic moduli defined in *Pollitz* [1992]. Note that the elastic modulus σ here is not to be confused with the stress tensor.

2.5.2 Matrizant matrix method

To solve the equations of motion we use the matrizant matrix method [*Haskell*, 1953]. We briefly outline the relevant aspects of the method here.

Suppose the SNREI Earth has N layers, with layer boundaries at

$$0 = r_0 < r_1 < \ldots < r_{N-1} < r_N = r_\oplus \tag{2.35}$$

that is, the points that belong to the kth layer satisfy

$$r_{k-1} \leq r \leq r_k \tag{2.36}$$

and suppose that within this layer the physical properties λ, μ, and ρ have the constant values λ_k, μ_k, and ρ_k, respectively. We will say that such a layer is a homogeneous layer. Note that for this stratified Earth the values of these physical properties are allowed to change discontinuously at the layer boundaries. The matrizant matrix method lets us solve the equations of motion for this layered Earth, provided that we know the general solution to the equations of motion, that is, Equation 2.31, for a homogeneous layer.

Briefly, there are D linearly independent solutions to the equations of motion where D is the dimension of the $\mathbf{y}$ vector. Thus $D = 4$ for the spheroidal modes, while $D = 2$ for the toroidal modes. Let these solutions be denoted by $\mathbf{c}_l$, where $l \in \{1, \ldots, D\}$. Hence the general solution to the equations of motion can be written as

$$\mathbf{y}(r) = \sum_{l=1}^{D} \alpha_l \, \mathbf{c}_l(r) \tag{2.37}$$

where the constant coefficients α_l are yet unknown. We form a matrix P whose columns are the vectors $\mathbf{c}_l$. This matrix is sometimes called the fundamental matrix. Thus, P obeys

$$\frac{dP}{dr} = A_n P \tag{2.38}$$

since each of its columns independently satisfies the same equation. Note that the general solution may now be written as

$$\mathbf{y}(r) = P(r)\,\boldsymbol{\alpha} \tag{2.39}$$

where the components of the vector $\boldsymbol{\alpha}$ are the coefficients α_l.

Since the columns of the fundamental matrix P are linearly independent, its matrix inverse P^{-1} exists. With the help of P and its inverse, we can propagate a solution $\mathbf{y}(r_{k-1})$ at the bottom of the kth homogeneous layer to the solution $\mathbf{y}(r_k)$ at its top. Let the fundamental matrix for this layer be P_k where we have set

$$\lambda = \lambda_k, \qquad \mu = \mu_k, \qquad \rho = \rho_k \tag{2.40}$$

in the matrix P, and let $\boldsymbol{\alpha}_k$ be the vector of coefficients of the general solution within this layer. Using Equation 2.39 we have,

$$\mathbf{y}(r_{k-1}) = P_k(r_{k-1})\,\boldsymbol{\alpha}_k \tag{2.41a}$$

$$\mathbf{y}(r_k) = P_k(r_k)\,\boldsymbol{\alpha}_k \tag{2.41b}$$

Eliminating $\boldsymbol{\alpha}_k$ we get

$$\mathbf{y}(r_k) = P_k(r_k)\,P_k^{-1}(r_{k-1})\,\mathbf{y}(r_{k-1}) = \Omega_k\,\mathbf{y}(r_{k-1}) \tag{2.42}$$

where the matrizant matrix, also known as the propagator matrix [see, for example, *Ben-Menahem and Singh*, 2012, §3.8],

$$\Omega_k = P_k(r_k)\,P_k^{-1}(r_{k-1}) \tag{2.43}$$

Applying Equation 2.42 repeatedly, we arrive at,

$$\mathbf{y}(r_\oplus) = \mathbf{y}(r_N) = \Omega_N\,\Omega_{N-1}\,\ldots\,\Omega_3\,\Omega_2\,\mathbf{y}(r_1) \tag{2.44}$$

That is, propagating a solution across layers amounts to multiplying it by the string of corresponding matrizant matrices.

The explicit form of the fundamental matrix P for the case of SNREI Earth without gravity is given in *Pollitz* [1992]. For the spheroidal modes,

$$P = \left[\begin{array}{c|c|c|c} \vdots & \vdots & \vdots & \vdots \\ \mathbf{c}_1 & \mathbf{c}_2 & \mathbf{c}_3 & \mathbf{c}_4 \\ \vdots & \vdots & \vdots & \vdots \end{array}\right] \tag{2.45}$$

where

$$\mathbf{c}_1 = r^{n-1}\left[\begin{array}{cccc} n & \dfrac{2\mu}{r}n(n-1) & 1 & \dfrac{2\mu}{r}(n-1) \end{array}\right]^T \tag{2.46a}$$

$$\mathbf{c}_2 = f_n^+ r^{n+1} \times \left[\begin{array}{c} (n+1)[\lambda n + \mu(n-2)] \\ \dfrac{2\mu}{r}(n+1)[\lambda(n^2-n-3)+\mu(n^2-n-2)] \\ \lambda(n+3)+\mu(n+5) \\ \dfrac{2\mu}{r}[\lambda(n^2+2n)+\mu(n^2+2n-1)] \end{array}\right] \tag{2.46b}$$

are solutions that are regular at $r = 0$, and $f_n^+ = [2(2n+3)]^{-1}$. To obtain expressions for $\mathbf{c}_3$ and $\mathbf{c}_4$, we note that the equations of motion, Equations 2.32 and 2.33, do not actually depend on n but rather depend only on $n(n+1)$. Thus, if we substitute a different n' with $n(n+1) = n'(n'+1)$ into $\mathbf{c}_1$ and $\mathbf{c}_2$, we obtain different solutions to the same equations. Solving, we see that the required transformation is,

$$n \mapsto n' = -(n+1) \tag{2.47}$$

which we will call the duality transform. Thus we can obtain $\mathbf{c}_3$ and $\mathbf{c}_4$ by applying the duality transformation to $\mathbf{c}_1$ and $\mathbf{c}_2$ respectively. Note that the latter solutions diverge at $r = 0$.

We found that the inverse of P can also be found in analytical form,

$$P^{-1} = \left[\begin{array}{ccc} \cdots & \mathbf{r}_1 & \cdots \\ \cdots & \mathbf{r}_2 & \cdots \\ \cdots & \mathbf{r}_3 & \cdots \\ \cdots & \mathbf{r}_4 & \cdots \end{array}\right] \tag{2.48}$$

where

$$\mathbf{r}_1 = \frac{1}{(4n^2-1)\sigma r^{n-1}} \times \begin{bmatrix} (\lambda+\mu)n(n+3)-\lambda \\ \frac{r}{2\mu}[\sigma+\mu+n(\lambda+\mu)] \\ -(n+1)[n^2(\lambda+\mu)-\sigma] \\ -\frac{r}{2\mu}(n+1)[n(\lambda+\mu)-2\sigma] \end{bmatrix}^T \tag{2.49a}$$

$$\mathbf{r}_2 = \frac{\begin{bmatrix} -(n+2) & -\frac{r}{2\mu} & n(n+2) & \frac{rn}{2\mu} \end{bmatrix}}{(2n+1)(2n+3)\sigma f_n^+ r^{n+1}} \tag{2.49b}$$

and $\mathbf{r}_3$ and $\mathbf{r}_4$ are found by applying the duality transformation to $\mathbf{r}_1$ and $\mathbf{r}_2$ respectively.

For the toroidal modes, we write the matrix P in *Pollitz* [1992] as,

$$P = \left[\begin{array}{c|c} \vdots & \vdots \\ \mathbf{c}_1 & \mathbf{c}_2 \\ \vdots & \vdots \end{array}\right] \tag{2.50}$$

where

$$\mathbf{c}_1 = r^n \begin{bmatrix} 1 & \frac{\mu}{r}(n-1) \end{bmatrix}^T \tag{2.51}$$

which is the solution regular at $r = 0$, and $\mathbf{c}_2$ is obtained by applying the duality transform to $\mathbf{c}_1$. We found the inverse of P to be,

$$P^{-1} = \begin{bmatrix} \cdots & \mathbf{r}_1 & \cdots \\ \cdots & \mathbf{r}_2 & \cdots \end{bmatrix} \tag{2.52}$$

where

$$\mathbf{r}_1 = \frac{\begin{bmatrix} n+2 & \frac{r}{\mu} \end{bmatrix}}{(2n+1)r^n} \tag{2.53a}$$

and $\mathbf{r}_2$ is found by applying the duality transform to $\mathbf{r}_1$.

Obviously, the physical solution of the equations of motion must be regular at $r = 0$, and thus must be a linear combination of the regular columns of P_1 inside the inner-most layer. Let this solution be called $\mathbf{y}_{\text{reg}}$. Thus,

$$\text{spheroidal modes:} \quad \mathbf{y}_{\text{reg}}(r) = \alpha_1 \, \mathbf{c}_1(r) + \alpha_2 \, \mathbf{c}_2(r) \tag{2.54a}$$

$$\text{toroidal modes:} \quad \mathbf{y}_{\text{reg}}(r) = \alpha_1 \, \mathbf{c}_1(r) \tag{2.54b}$$

for $0 = r_0 \leq r \leq r_1$, where the coefficients α_l are yet unknown, and $\mathbf{c}_l$ are columns of the corresponding P_1 matrices. Then this solution propagated to the surface is,

$$\mathbf{y}_{\text{reg}}(r_\oplus) = \mathbf{y}_{\text{reg}}(r_N) = \Omega_N \, \Omega_{N-1} \, \ldots \, \Omega_3 \, \Omega_2 \, \mathbf{y}_{\text{reg}}(r_1) \tag{2.55}$$

On the other hand, our required solution $\mathbf{y}$ undergoes a jump discontinuity at the source radius r_s that we will present in Section 2.5.4. We may assume that the source is at the top of some layer s, because if not, we can always insert an artificial boundary by splitting the layer containing the source at the source radius r_s. We can propagate the discontinuity $\Delta\mathbf{y}$ to the surface,

$$\mathbf{y}_{\text{disc}}(r_\oplus) = \mathbf{y}_{\text{disc}}(r_N) = \Omega_N \, \Omega_{N-1} \, \ldots \, \Omega_{s+1} \, \Omega_s \, \Delta\mathbf{y} \tag{2.56}$$

where we let $\mathbf{y}_{\text{disc}}(r) = \mathbf{0}$ for $0 \leq r < r_s$. Thus the final solution is,

$$\mathbf{y} = \mathbf{y}_{\text{reg}} + \mathbf{y}_{\text{disc}} \tag{2.57}$$

At the surface of the Earth, this solution must obey the free surface conditions,

$$\text{spheroidal modes:} \quad y_2^S(r_\oplus) = y_4^S(r_\oplus) = 0 \tag{2.58a}$$

$$\text{toroidal modes:} \quad y_2^T(r_\oplus) = 0 \tag{2.58b}$$

In both cases, the number of equations matches the number of unknowns, namely, the number the non-zero coefficients α_l for the inner-most layer, two for the spheroidal case and one for the toroidal case. Solving for these coefficients we obtain the required unique solution.

2.5.3 Seismic source geometry

Let the vector area of the differential fault plane be $d\mathbf{A}$. That is, the magnitude of $d\mathbf{A}$ represents the area of an infinitesimal part of the fault plane, and the direction

of $d\mathbf{A}$ is normal to that plane. If the dislocation across the plane is $\Delta\mathbf{u}$, then the differential seismic moment tensor corresponding to this dislocation in component form is [*Aki and Richards*, 2002, §3.3],

$$dM_{ij} = \sum_{kl} C_{ijkl}\, \Delta u_k\, dA_l \tag{2.59}$$

Substituting the expression for C from Equation 2.24 we get, in component-free form,

$$dM = \lambda_s\, \Delta\mathbf{u} \cdot d\mathbf{A} + \mu_s\, (\Delta\mathbf{u} \otimes d\mathbf{A} + d\mathbf{A} \otimes \Delta\mathbf{u}) \tag{2.60}$$

where λ_s and μ_s are the Lamé coefficients of the layer that the source belongs to, and $\otimes$ denotes the tensor product.

As an internal event of the Earth system, an earthquake cannot alter the total linear and angular momenta of the system. The conservation of linear momentum leads to the moment tensor being a second rank tensor, while it being symmetric is a consequence of the conservation of angular momentum.

When the second-rank symmetric moment tensor is represented as a 3×3 matrix, it has 6 independent components. In all generality, the moment tensor then can be written as a linear combination of any six symmetric matrices, as long as they are linearly independent. We will choose them to have the same scalar moment,

$$M_0 = \left(\sum_{j,k} \left(M_{jk}\right)^2 \right)^{\frac{1}{2}} \tag{2.61}$$

for easy comparison of the GC motion they induce. Specifically, we choose M_0 so that the moment magnitude

$$M_W = \frac{2}{3} \log_{10}(M_0) - 10.7 \tag{2.62}$$

is 9.0, characterising a reasonably realistic great earthquake. Here, M_0 is expressed in dyne · cm.

Gilbert and Dziewonski [1975] showed that a point seismic source described by a second-rank symmetric matrix can only excite modes with $|m| \leq 2$ in the epicentral coordinate system. Because of the enormous savings in computational resources,

we switch to epicentral coordinates for the rest of the section. This change of coordinates is achieved by rotating our Earth system by the matrix

$$\mathscr{R}(\hat{\mathbf{y}}, -\theta_s)\,\mathscr{R}(\hat{\mathbf{z}}, -\phi_s)$$

Here, (r_s, θ_s, ϕ_s) are the spherical coordinates of the point source, and the matrix $\mathscr{R}(\hat{\mathbf{n}}, \alpha)$ is the rotation matrix for a counter-clockwise rotation by an angle α around the axis $\hat{\mathbf{n}}$. Read from right to left, the first rotation brings the source to the prime meridian while the second sends it to the north pole. It is understood that we have to rotate the displacement field calculated in the epicentral coordinates back to the geographical coordinates in the end by applying the transpose of this matrix.

In the epicentral coordinate system that we have adopted here, the θ coordinate of a point is its distance from the point source, that is, its epicentral distance. The ϕ coordinate here is the source-receiver azimuth measured counter-clockwise from the geographical south [*Pollitz*, 1996]. We see that $\hat{\boldsymbol{\theta}}$ continues to point south throughout the transformation to the epicentral coordinate system and ends up lying on the prime meridian, that is, the $\phi = 0$ semi-circle. We will express the moment tensor in the spherical geographical coordinates and, due to the conventions adopted here, it has the same components in the spherical epicentral coordinates as well. The spherical and Cartesian components of the tensor in epicentral coordinates are related by,

$$\begin{bmatrix} M_{rr} & M_{r\theta} & M_{r\phi} \\ M_{\theta r} & M_{\theta\theta} & M_{\theta\phi} \\ M_{\phi r} & M_{\phi\theta} & M_{\phi\phi} \end{bmatrix} = \begin{bmatrix} M_{zz} & M_{zx} & M_{zy} \\ M_{xz} & M_{xx} & M_{xy} \\ M_{yz} & M_{yx} & M_{yy} \end{bmatrix} \tag{2.63}$$

The trace of this matrix, that is, its scalar part, is invariant under coordinate transformations, and represents an isotropic explosion or implosion, depending on its sign. Because of its special physical significance, we choose the scalar moment tensor to be one of the basic sources to investigate:

$$M_{\text{iso}} = \frac{M_0}{\sqrt{3}} \begin{bmatrix} 1 & 0 & 0 \\ 0 & 1 & 0 \\ 0 & 0 & 1 \end{bmatrix} \tag{2.64}$$

where the matrix is expressed in the epicentral spherical coordinate system of Equation 2.63. We choose the remaining five basis sources to be trace-less. Three

of these are double couples:

$$M_{\text{dc-1}} = \frac{M_0}{\sqrt{2}} \begin{bmatrix} 0 & 1 & 0 \\ 1 & 0 & 0 \\ 0 & 0 & 0 \end{bmatrix} \tag{2.65a}$$

$$M_{\text{dc-2}} = \frac{M_0}{\sqrt{2}} \begin{bmatrix} 0 & 0 & 0 \\ 0 & 0 & 1 \\ 0 & 1 & 0 \end{bmatrix} \tag{2.65b}$$

$$M_{\text{dc-3}} = \frac{M_0}{\sqrt{2}} \begin{bmatrix} 0 & 0 & 1 \\ 0 & 0 & 0 \\ 1 & 0 & 0 \end{bmatrix} \tag{2.65c}$$

Now, consider a counter-clockwise rotation of the whole system by an angle of $\pi/2$ around $\hat{\mathbf{z}}$ that sends $\hat{\mathbf{x}}$ to $\hat{\mathbf{y}}$ and $\hat{\mathbf{y}}$ to $-\hat{\mathbf{x}}$. From Equations 2.63 and 2.65, we see that this rotation sends $M_{\text{dc-1}}$ to $M_{\text{dc-3}}$. Hence, to obtain the displacement field corresponding to $M_{\text{dc-3}}$, we only need to rotate the field corresponding to $M_{\text{dc-1}}$. Therefore, we do not consider $M_{\text{dc-3}}$ separately from now on. Likewise, of the two compensated linear vector dipoles,

$$M_{\text{clvd-1}} = \frac{M_0}{\sqrt{6}} \begin{bmatrix} 1 & 0 & 0 \\ 0 & -2 & 0 \\ 0 & 0 & 1 \end{bmatrix} \tag{2.66a}$$

$$M_{\text{clvd-2}} = \frac{M_0}{\sqrt{6}} \begin{bmatrix} 1 & 0 & 0 \\ 0 & 1 & 0 \\ 0 & 0 & -2 \end{bmatrix} \tag{2.66b}$$

the second can be obtained from the first by the same rotation as before. Therefore, we do not consider $M_{\text{clvd-2}}$ separately in the tabulation of GC motion due to these sources, as it too can be obtained by applying the same rotation.

Traditionally, fault slip models are often described in terms of the local observations at the fault site on the ground. The local geographical frame consists of the directions $\hat{\mathbf{E}} = \hat{\boldsymbol{\phi}}$ (east), $\hat{\mathbf{N}} = -\hat{\boldsymbol{\theta}}$ (north), and $\hat{\mathbf{U}} = \hat{\mathbf{r}}$ (up). However, with these relationships provided, we continue to use the spherical $\hat{\mathbf{r}}$-$\hat{\boldsymbol{\theta}}$-$\hat{\boldsymbol{\phi}}$ coordinate frame. The differential vector area

$$d\mathbf{A} = \hat{\mathbf{n}}\, dA \tag{2.67}$$

where dA is the magnitude of the differential area, and the normal $\hat{\mathbf{n}}$ to the fault plane has the components in the spherical coordinates [*Stein and Wysession*, 2009, §4.2.1]

$$\hat{\mathbf{n}} = \begin{bmatrix} \cos\delta & \sin\delta\,\sin\phi_f & \sin\delta\,\cos\phi_f \end{bmatrix}^T \tag{2.68}$$

where δ is the dip angle of the fault plane from the horizontal, and ϕ_f is the strike of the fault measured clockwise from the geographical north. Similarly, let

$$\Delta\mathbf{u} = \Delta u\,\hat{\mathbf{d}} \tag{2.69}$$

where Δu is the magnitude of the slip, and $\hat{\mathbf{d}}$ is the direction of the slip. For tensile dislocations, $\hat{\mathbf{d}} = \hat{\mathbf{n}}$ for dilatations, whereas $\hat{\mathbf{d}} = -\hat{\mathbf{n}}$ for compressions. For shear dislocations, $\hat{\mathbf{n}}$ and $\hat{\mathbf{d}}$ are orthogonal, and

$$\hat{\mathbf{d}} = \begin{bmatrix} \sin\lambda\,\sin\delta \\ -\cos\lambda\,\cos\phi_f - \sin\lambda\,\cos\delta\,\sin\phi_f \\ \cos\lambda\,\sin\phi_f + \sin\lambda\,\cos\delta\,\cos\phi_f \end{bmatrix} \tag{2.70}$$

where λ is the slip angle measured counter-clockwise in the fault plane from the horizontal strike direction. The slip angle λ here is not to be confused with the Lamé coefficient with the same symbol.

2.5.4 Discontinuities at the source

As explained in Section 2.5.2, we still need to specify the discontinuity in the $\mathbf{y}$ vectors at the source radius r_s,

$$\Delta\mathbf{y} = \lim_{r\searrow r_s} \mathbf{y}(r) - \lim_{r\nearrow r_s} \mathbf{y}(r) \tag{2.71}$$

where $\searrow$ and $\nearrow$ signify taking the limits from above and below, respectively. The solutions for Δy for shear dislocations in *Ben-Menahem and Singh* [2012, §4.5.4] were complemented by those for tensile dislocations in *Pollitz* [1996]. Note, however, that these solutions are essentially the same as in *Saito* [1967], notwithstanding the slightly different notations.

Since in epicentral coordinates only the modes with $|m| \leq 2$ are excited, and since furthermore from Equation 2.12 it follows that

$$\Delta\mathbf{y}_{n,-m} = (-1)^m \Delta\mathbf{y}^*_{nm} \tag{2.72}$$

we only need to specify $\Delta\mathbf{y}$ for $m \in \{0,1,2\}$. To present them succinctly, we define the constants,

$$b_{n,0} = \lim_{\theta\to 0}\lim_{\phi\to 0} Y_{n,0} = \left(\frac{2n+1}{4\pi}\right)^{\frac{1}{2}} \tag{2.73a}$$

$$b_{n,1} = \lim_{\theta\to 0}\lim_{\phi\to 0} \frac{\partial}{\partial\theta} Y_{n,1} = -\frac{1}{2} b_{n,0}\,(n(n+1))^{\frac{1}{2}} \tag{2.73b}$$

$$b_{n,2} = \lim_{\theta\to 0}\lim_{\phi\to 0} \frac{\partial^2}{\partial\theta^2} Y_{n,2} = -\frac{1}{2} b_{n,1}\,((n-1)(n+2))^{\frac{1}{2}} \tag{2.73c}$$

and the moment tensor components,

$$M_1 = M_{rr} \tag{2.74a}$$

$$M_2 = \frac{1}{2}\left(M_{\theta\theta} + M_{\phi\phi}\right) - \frac{\lambda}{\sigma} M_{rr} \tag{2.74b}$$

$$M_3 = -M_{r\phi} - iM_{r\theta} \tag{2.74c}$$

$$M_4 = M_{\theta\theta} - M_{\phi\phi} - 2iM_{\theta\phi} \tag{2.74d}$$

Then the discontinuities for the spheroidal modes are,

$$\text{for } m=0: \quad \Delta\mathbf{y}^S_{n,0} = \frac{b_{n,0}}{r_s^2} \begin{bmatrix} \frac{1}{\sigma} M_1 \\ -\frac{2}{r_s} M_2 \\ 0 \\ \frac{1}{r_s} M_2 \end{bmatrix} \tag{2.75a}$$

$$\text{for } m=1: \quad \Delta\mathbf{y}^S_{n,1} = \frac{b_{n,1}}{r_s^2} \begin{bmatrix} 0 \\ 0 \\ \frac{1}{\mu\, n(n+1)} iM_3 \\ 0 \end{bmatrix} \tag{2.75b}$$

$$\text{for } m=2: \quad \Delta\mathbf{y}^S_{n,2} = \frac{b_{n,2}}{r_s^2} \begin{bmatrix} 0 \\ 0 \\ 0 \\ -\frac{1}{r_s} \frac{1}{n(n+1)} M_4 \end{bmatrix} \tag{2.75c}$$

Similarly, for the toroidal modes,

$$\text{for } m=1: \quad \Delta\mathbf{y}^T_{n,1} = \frac{b_{n,1}}{r_s^2}\begin{bmatrix} \dfrac{1}{\mu\, n(n+1)} M_3 \\ 0 \end{bmatrix} \tag{2.76a}$$

$$\text{for } m=2: \quad \Delta\mathbf{y}^T_{n,2} = \frac{b_{n,2}}{r_s^2}\begin{bmatrix} 0 \\ \dfrac{1}{r_s} \dfrac{1}{n(n+1)}\, iM_4 \end{bmatrix} \tag{2.76b}$$

since the $m=0$ mode is absent here.

2.5.5 The degree-0 and degree-1 modes

The degree-0 mode does not have a toroidal part, and in the spheroidal part, $\mathbf{S}_{00}$ is identically zero, so its coefficients $y^S_{3,00}$ and $y^S_{4,00}$, in Equations 2.9c and 2.30a respectively, are not relevant to the problem. Thus the equation of motion reduces to the simpler system of differential equations,

$$\frac{d}{dr}\begin{bmatrix} y_1 \\ y_2 \end{bmatrix} = \begin{bmatrix} -\dfrac{2\lambda}{\sigma r} & \dfrac{1}{\sigma} \\ \dfrac{4\gamma}{r^2} & \dfrac{2}{r}\left(\dfrac{\lambda}{\sigma}-1\right) \end{bmatrix}\begin{bmatrix} y_1 \\ y_2 \end{bmatrix} \tag{2.77}$$

Likewise, the fundamental matrix reduces to

$$P = \begin{bmatrix} \dfrac{r}{3} & -\dfrac{1}{r^2} \\ \kappa & \dfrac{4\mu}{r^3} \end{bmatrix} \tag{2.78}$$

where

$$\kappa = \lambda + \frac{2}{3}\mu \tag{2.79}$$

is the bulk modulus. The regular solution starts with the first column of this matrix inside the inner-most layer multiplied by an unknown constant, and the boundary condition at the free surface

$$y^S_{2,00}(r_\oplus) = 0 \tag{2.80}$$

fixes this constant. Thus, these conditions together with the expression of the discontinuity in Section 2.5.4 provide us with the unique solution for the degree-0 case.

As mentioned in Section 2.4, the boundary conditions for the degree-1 equations are degenerate because of the symmetry of the equations of motion under translations and rotations. For the toroidal modes, the regular solution inside the inner-most layer reads

$$\mathbf{y}_{\text{reg}} = \alpha_1 \, \mathbf{c}_1 = \alpha_1 \begin{bmatrix} r & 0 \end{bmatrix}^T \tag{2.81}$$

that is, the second component is identically zero, and continues to remain zero when propagated upwards. Similarly, the second component of the solution $\mathbf{y}_{\text{disc}}$ corresponding to the jump discontinuity remains zero as well. Thus, the boundary condition

$$y^T_{2,1,m}(r_\oplus) = 0 \tag{2.82}$$

cannot recover the coefficient α_1. Instead, we take the final solution, $\mathbf{y} = \mathbf{y}_{\text{reg}} + \mathbf{y}_{\text{disc}}$, and apply the condition for conservation of angular momentum

$$\int_0^{r_\oplus} \rho \; y^T_{1,1,m} \, r^3 \, dr = 0 \tag{2.83}$$

to it to calculate α_1, and thus construct the required solution. Note that although *Sun and Dong* [2014] provide an analytic solution in this case, their solution is only applicable to a homogeneous Earth, but our generalisation is applicable to any layered Earth model.

Likewise, for the spheroidal modes, the initial regular solution inside the inner-most shell,

$$\mathbf{y}_{\text{reg}} = \alpha_1 \, \mathbf{c}_1 + \alpha_2 \, \mathbf{c}_2 \tag{2.84}$$

from Section 2.5.2 is propagated upwards towards the surface. However, the degree-1 mode solutions, both $\mathbf{y}_{\text{reg}}$ and $\mathbf{y}_{\text{disc}}$, obey [*Farrell*, 1972]

$$y^S_{2,1,m} + 2\, y^S_{4,1,m} = 0 \tag{2.85}$$

and therefore the two boundary conditions at the surface

$$y^S_{2,1,m}(r_\oplus) = y^S_{4,1,m}(r_\oplus) = 0 \tag{2.86}$$

are not independent. Again, the extra equation that lets us solve for α_1 and α_2 and thus construct the unique solution is the condition of conservation of linear momentum

$$\int_0^{r_\oplus} \rho \left(y^S_{1,1,m} + 2y^S_{3,1,m} \right) r^2 \, dr = 0 \tag{2.87}$$

applied to the final solution $\mathbf{y} = \mathbf{y}_{\text{reg}} + \mathbf{y}_{\text{disc}}$.

2.6 The Preliminary Reference Earth Model

The SNREI Earth model that we use is the isotropic Preliminary Reference Earth Model (PREM) [*Dziewonski and Anderson*, 1981]. It is a so-called "1D model" in that the physical properties of the Earth, such as the shear modulus μ, the bulk modulus $\kappa = \lambda + \frac{2}{3}\mu$, and the density ρ are functions of only the radius r. It is stratified with clearly defined layer boundaries at radii $0 = r_0, r_1, \ldots, r_{N-1}, r_N = r_\oplus$, between which the physical properties, and therefore the seismic wave velocities, are constant. That is, we ignore the fine topographical features on the Earth surface as well as the small anisotropy and inhomogeneity of the material inside the Earth for theoretical simplicity.

The PREM was constructed by inverting seismic observations such as the travel times of earthquake signals and the normal modes of free oscillations of the Earth. Earthquakes in this respect are akin to experiments provided by nature that let us measure the properties of the Earth. Of course, these properties depend on the timescale of the experiment. For the short timescale of several minutes that the earthquakes usually take place in, the Earth behaves essentially as an elastic solid, with allowance for short-term anelasticity to model seismic wave attenuation. We note that were we to study processes that span decades such as postseismic relaxation or glacial isostatic adjustment, we would also need to adopt a model for the rheology of the mantle which is viscoelastic for that timescale.

The relevant physical properties of the Earth according to the PREM are shown in Figure 2.2. The sharp changes in the properties at the Mohorovičić discontinuity

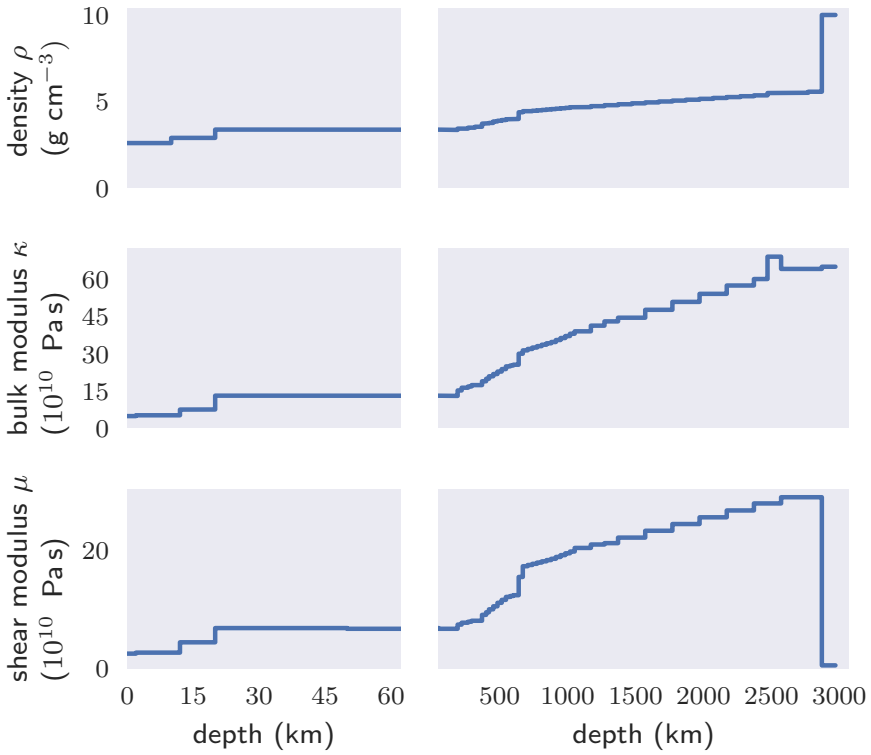

Figure 2.2: The profiles of the physical properties of the layered Earth for the PREM as a function of depth from the Earth surface. The Moho discontinuity (top) is at ~15–25 km depth and the CMB (bottom) is at ~3000 km depth. Beneath the CMB the Earth is liquid and therefore has no shear modulus.

(Moho) and the core-mantle boundary (CMB) cause corresponding sharp changes in the GC motion caused by a seismic point source as its depth varies.

2.7 Theory of the geopotential field

Here, we present the physical theory that we will use in Chapter 5 to model the elastic deformation caused by surface water movements. We imagine the Earth to be decomposed into two components: a solid elastic Earth modelled by the PREM, and a thin layer of water that acts as a load on the surface of the Earth. The layer of water is described by its surface density σ that creates, due to its own gravity, a

"load potential" field V given by Poisson's equation,

$$\nabla^2 V = 4\pi G\,\rho \tag{2.88}$$

where $\rho = \sigma\,\delta(r - r_\oplus)$ is the density of the water confined to the surface, $r_\oplus$ is the radius of the Earth, and G is the universal gravitational constant. If we expand σ and V in terms of the spherical harmonics,

$$\sigma(\theta,\phi) = \sum_{n,m} \sigma_{nm}\, Y_{nm}(\theta,\phi) \tag{2.89a}$$

$$V(\theta,\phi) = \sum_{n,m} V_{nm}\, Y_{nm}(\theta,\phi) \tag{2.89b}$$

Poisson's equation takes the form [*Blewitt*, 2003],

$$-\frac{V_{nm}}{g} = \frac{4\pi\, r_\oplus^3}{M_\oplus}\,\frac{\sigma_{nm}}{2n+1} \tag{2.90}$$

where $g = GM_\oplus/r_\oplus^2$ is the average acceleration due to gravity at the surface of the Earth, and $M_\oplus$ is the mass of the whole Earth system.

When the elastic deformation field $\mathbf{u}$ at the surface is decomposed into vector spherical harmonics as in Equation 2.9, the load Love number theory predicts [*Farrell*, 1972],

$$y^S_{1,nm} = -h_n\,\frac{V_{nm}}{g} \tag{2.91a}$$

$$y^S_{3,nm} = -l_n\,\frac{V_{nm}}{g} \tag{2.91b}$$

where h_n and l_n are the usual load Love numbers that are calculated for the PREM. The second set, l_n, are sometimes referred to as the Shida numbers as well. Note that the toroidal modes are absent for the surface loading problem. Also, *Farrell* [1972] and *Blewitt* [2003] define the gravitational potential to have the opposite sign when compared to the conventional definition that we have adopted here, resulting in corresponding sign reversals in Equations 2.88, 2.90, and 2.91.

Space geodetic satellites such as the Gravity Recovery and Climate Experiment (GRACE) measure the "space potential" that is related to the load potential via the load Love numbers k_n as

$$U_{nm} = (1 + k_n)\,V_{nm} \tag{2.92}$$

From this equation, we can solve for V_{nm} and obtain the displacement field from Equation 2.91. Thus we can calculate the elastic deformation from the loading due to surface water from the space potential measurements.

It is customary to refer to the dimensionless numbers h_n, l_n, and k_n collectively as the load Love numbers. The calculation of these numbers is quite similar in spirit with the calculation of Green's functions for the seismic sources described in Section 2.5 and uses much of the same mathematical machinery. Crucially though, gravity in this case is unavoidable, and we need to include two more components into the $\mathbf{y}$ vector. The first, y_5, comes from the expansion of the perturbation in the total gravitational potential,

$$U_1(r,\theta,\phi) = -\sum_{n,m} y^S_{5,nm}(r)\, Y_{nm}(\theta,\phi) \tag{2.93}$$

and the second, y_6, is related to the gradient of the potential and is defined by,

$$y^S_{6,nm}(r) = \frac{d}{dr} y^S_{5,nm} - 4\pi G\rho\, y^S_{1,nm} + \frac{n+1}{r} y^S_{5,nm} \tag{2.94}$$

Consequently, the $\mathbf{y}$ vector now obeys Equation 2.31 with an A_n matrix that is 6×6 in size. See, for example, *Takeuchi and Saito* [1972, §II.C], or Appendix C.5, for its explicit form.

There are now three linearly independent solutions that are regular at $r = 0$, and we propagate the linear combination of these solutions with three unknown coefficients from the inner-most shell to the surface either by the matrizant matrix method or numerically. In order to calculate the Love numbers from Equations 2.91 and 2.92, we need to choose a value for the load potential. It is easy to verify that V_{nm}/g has the dimension of length, so we can use the natural length scale of the problem and set

$$-\frac{V_{nm}}{g} = r_\oplus \tag{2.95}$$

whose corresponding boundary conditions,

$$y^S_{2,nm}(r_\oplus) = -\frac{(2n+1)\, g^2}{4\pi G} \tag{2.96a}$$

$$y^S_{4,nm}(r_\oplus) = 0 \tag{2.96b}$$

$$y^S_{6,nm}(r_\oplus) = (2n+1)\, g \tag{2.96c}$$

allow us solve for the three unknown coefficients and thus provides us with a unique solution [*Farrell*, 1972; *Saito*, 1974]. See Appendix C.6 for a derivation of Equation 2.96. The load Love numbers are then calculated from the solution using the relations,

$$y^S_{1,nm}(r_\oplus) = h_n\, r_\oplus \tag{2.97a}$$
$$y^S_{3,nm}(r_\oplus) = l_n\, r_\oplus \tag{2.97b}$$
$$y^S_{5,nm}(r_\oplus) = (1+k_n)\, g\, r_\oplus \tag{2.97c}$$

that we get by substituting Equation 2.95 into Equations 2.91 and 2.92. Note that since neither the matrix A_n nor the boundary conditions depend on m, these solutions also are independent of it.

2.7.1 The degree-0 and degree-1 modes

We assume that the total mass of the water layer is conserved, and therefore, σ_{00} is a constant in time. Consequently, so is V_{00}, and in turn, the $y^S_{1,00}$ coefficient. Thus by Equation 2.14, the load of the water surface compresses the Earth by a factor D_{CF} that never changes due to surface water movements. If we take the undeformed Earth to be the Earth in equilibrium with the load of the surface water distributed uniformly over the surface, we can effectively take D_{CF} to be zero.

Also, since there are no toroidal modes in this case, by Equation 2.14, $\mathbf{R}_{\mathrm{CF}}$ is identically zero here. However, in order to calculate the shift in geocentre $\mathbf{T}_{\mathrm{CF}}$ from the space potential observed by GRACE satellites, we would need to solve Equation 2.92 for $V_{1,m}$ for $m \in \{-1, 0, 1\}$. Unfortunately, GRACE cannot directly measure the degree-1 geopotential fields due to the water layer alone, so we need to model these modes separately. In Chapter 5, we will use the degree-1 geopotential fields from *Swenson et al.* [2008] derived from a combination of numerical ocean models and the $n \geq 2$ GRACE data. Their procedure, as expected, utilises the conservation of linear momentum of the total Earth system to obtain the degree-1 fields.

There is, however, an additional complication in calculating the degree-1 deformation field, and consequently, the GC motion, even if the degree-1 space potential field is known. We implicitly assumed that the equations of motion were derived with respect to an inertial reference frame. But in the most natural choice of inertial

reference frame, the CM frame, Equation 2.92 is not solvable for the load potential because in this frame $k_1 = -1$. Therefore, *Swenson et al.* [2008] provide their geopotential field in the CF frame. We derive the displacement fields in the CM frame from this field using a set of transformation laws for the load Love numbers obtained by *Blewitt* [2003]. We describe these transformation laws in the next section.

2.7.2 Transformation laws for the degree-1 load Love numbers

The degree-1 modes of the displacement field contain rigid translations and rotations and therefore depend on the choice of the reference frame as discussed in Section 2.4. For a completely general rigid transformation, the quantities in Equations 2.91 and 2.92 would transform in a complicated manner. However, *Blewitt* [2003] considered a special sub-group of coordinate transforms whose effect can be encoded completely into a simple set of transformation laws for the load Love numbers, provided some reasonable estimates about the surface water density field hold.

Here, it is useful to introduce the load moment vector,

$$\mathbf{m} = \int_{\oplus} \mathbf{r}\, \rho\, dV = r_{\oplus}^3 \sum_{m=-1}^{1} \sigma_{1,m}\, \boldsymbol{\Delta}_m \tag{2.98a}$$

where the constant vectors $\boldsymbol{\Delta}_m$ are defined in Appendix B.1. Thus the load moment vector depends only on the degree-1 components of the density (see Appendix B.5 for a derivation). The physical significance of this vector comes from the relation,

$$\mathbf{m} = M_L\, \mathbf{r}_L \tag{2.99}$$

where

$$M_L = \sqrt{4\pi}\, \sigma_{00}\, r_{\oplus}^2 \tag{2.100}$$

is the total mass of the liquid layer, and $\mathbf{r}_L$ is its centre of mass with respect to the inertial CM frame. The analogous quantity for the solid Earth is $M_S\, \mathbf{r}_S$, where M_S is the mass of the solid Earth, and $\mathbf{r}_S$ is its centre of mass, that is, the Centre of solid

Earth (CE) also denoted by $\mathbf{r}_{\mathrm{CE}}$, again with respect to the CM frame. Obviously,

$$M_\oplus = M_S + M_L \tag{2.101a}$$

$$M_\oplus \, \mathbf{r}_{\mathrm{CM}} = M_S \, \mathbf{r}_S + M_L \, \mathbf{r}_L \tag{2.101b}$$

and since in the CM frame, $\mathbf{r}_{\mathrm{CM}} = \mathbf{0}$, we have,

$$M_S \, \mathbf{r}_S = -\mathbf{m} \tag{2.102}$$

That is, as the centre of mass of the liquid layer moves in inertial space, the centre of mass of the solid Earth recoils in the opposite direction.

Blewitt [2003] showed that if frame A is translated without rotation to frame B by a vector parallel to the load moment vector,

$$[\mathbf{T}_B]_A = [\alpha_B]_A \frac{\mathbf{m}}{M_\oplus} \tag{2.103}$$

then the degree-1 load Love numbers transform according to the rules,

$$[h_1]_B = [h_1 - \alpha_B]_A \tag{2.104a}$$

$$[l_1]_B = [l_1 - \alpha_B]_A \tag{2.104b}$$

$$[k_1]_B = [k_1 - \alpha_B]_A \tag{2.104c}$$

See Appendix B.5 for a derivation. Note that Equation 2.103 in fact defines $[\alpha_B]_A$. We emphasise again that the load Love numbers for the other modes remain invariant under such rigid translations. Here, the quantities inside the square brackets are measured with respect to the frames indicated in the subscript. In the derivation of these transformation laws, the order of magnitude estimates of the seasonal variations,

$$\mathbf{r}_L \approx 10^6 \, \mathrm{m} \tag{2.105a}$$

$$M_L \approx 10^{16} \, \mathrm{kg} \tag{2.105b}$$

and

$$M_\oplus \approx 10^{24} \, \mathrm{kg} \tag{2.106}$$

have been used that show that $\mathbf{m}$ is approximately frame independent, provided that the origin of the frame is not too far from the CM compared to the magnitude

of $\mathbf{r}_L$. As we shall see in Chapter 5, $[\mathbf{T}_{\mathrm{CF}}]_{\mathrm{CM}}$ is actually of the order of millimetres, so this assumption is well-justified.

In *Blewitt* [2003], theoretical arguments are presented to show,

$$[\alpha_{\mathrm{CE}}]_{\mathrm{CM}} = -1 \tag{2.107a}$$

$$[\alpha_{\mathrm{CF}}]_{\mathrm{CE}} = \frac{1}{3}[h_1 + 2l_1]_{\mathrm{CE}} \tag{2.107b}$$

and hence we obtain (see Appendix B.5 for the derivation),

$$[1 + k_1]_{\mathrm{CF}} = -\frac{1}{3}[h_1 + 2l_1]_{\mathrm{CM}} \approx 1.026 \neq 0 \tag{2.108}$$

using the values

$$[h_1]_{\mathrm{CM}} \approx -1.286 \tag{2.109a}$$

$$[l_1]_{\mathrm{CM}} \approx -0.896 \tag{2.109b}$$

for the PREM. Thus, Equation 2.92 can now be solved for $V_{1,m}$ by dividing both sides by the non-zero value of $(1 + k_1)$ in this frame.

Chapter 3

Methodology

We now examine certain approaches to the practical determination of geocentre (GC) motion from space geodetic observations, and develop our theoretical framework to estimate the network effect (NE) for them. As in Section 2.2, we measure GC motion by the shifts in Helmert parameters (HPs) of transformation from the unaffected Centre of Motion (CM) frame to the deformed frame, which in this case is the Centre of Network (CN) frame of the geodetic ground stations instead of the theoretical Centre of Figure (CF) frame. We are interested here not only in the GC motion in the translational sense, but also in the changes in the scale and the orientation of the surface of the solid Earth.

In the last chapter we considered only an instantaneous change to the solid Earth surface, and therefore, shifts in the 7 Helmert parameters of Euclidean similarity transformations between coordinate systems: three components of the translation vector $\mathbf{T}$, one scale parameter D, and three components of the rotation vector $\mathbf{R}$. In the following, we will refer to these parameters as the 'instantaneous parameters'. For continuous time-varying deformations, we will also need to describe the relative uniform motion between the two reference frames by specifying the time derivatives of these parameters. We will refer to these as the 'derivative parameters', and denote them by $\dot{\mathbf{T}}$, $\dot{D}$, and $\dot{\mathbf{R}}$ respectively. The unqualified term 'Helmert parameters' will refer to the combined set of 14 parameters.

In *Zhou et al.* [2016], two methods for calculating the instantaneous CN parameters were considered which they call the summation method and the transformation method. We will introduce these methods in Section 3.1. The former method will

be useful to us for its conceptual simplicity, while the latter is advantageous in practical applications.

In recent years, several studies have evaluated the magnitude of the NE associated with GC motion determination for particular cases [see, for example, *Zhang and Jin*, 2014; *Zhou et al.*, 2016]. However, a systematic analysis of the error introduced by the NE is, to the best of our knowledge, still lacking. Therefore, in Sections 3.2 and 3.3 we will introduce our framework to estimate the magnitude of the NE due to any displacement field over the solid Earth surface.

We call our estimate the 'expected bias' in the HP in question as it is a measure of the expected magnitude of the sampling bias for a finite network. In Section 3.4, we will present a procedure to efficiently compute the expected bias from the spherical harmonic decomposition of the displacement field. In Section 3.5 we will discuss extensions of the summation method and the transformation method to the time-dependent case. Our method for estimating the NE applies to these as well.

Finally, in Section 3.6 we propose a variation of the CN frame that we will call the 'Centre of Weighted Network' (CWN) frame. As we shall see later, except some exceptional cases, the CWN frame offers a better determination of the true GC motion from the displacements at the ground stations.

3.1 Instantaneous case

The main difference between the summation method and the transformation method is that the calculations of the different CN parameters are decoupled in the summation method whereas in the transformation method they are mixed together through a system of linear equations. Our statistical interpretation of the CN frame parameters in Section 3.2 is therefore simpler for the summation method. But we consider the transformation method here as well since it is closer in spirit to the procedure employed in the actual construction of the ITRF [*Altamimi et al.*, 2002].

In Chapter 4, we will investigate coseismic displacements due to great earthquakes as a case study of instantaneous surface deformation.

3.1.1 Summation method

In the summation method, for a network of N stations at positions $\mathbf{r}_k$ on the surface of the undeformed Earth, where $1 \leq k \leq N$, the (geometric) CN is defined to be,

$$\mathbf{r}_{\mathrm{CN}} = \frac{1}{N} \sum_{k=1}^{N} \mathbf{r}'_k \tag{3.1}$$

Here, $\mathbf{r}'_k$ is the position of the kth station on the deformed Earth, and therefore its displacement is $\mathbf{u}(\mathbf{r}_k) = \mathbf{r}'_k - \mathbf{r}_k$. Note that this formula is a straightforward discretisation of

$$\mathbf{r}_{\mathrm{CF}} = \frac{1}{4\pi} \int_{\partial \oplus} \mathbf{r}'(\theta, \phi)\, d\Omega \tag{3.2}$$

that is, the definition of the CF introduced in Section 1.5.

Thus the shifts in the CN frame parameters, measured from the stationary CM frame, are the discrete counterparts of those for the CF frame parameters in Equation 2.6,

$$\mathbf{T}_{\mathrm{CN}} = \frac{1}{N} \sum_{k=1}^{N} \mathbf{u}(\mathbf{r}_k) \tag{3.3a}$$

$$D_{\mathrm{CN}} = \frac{1}{N} \frac{1}{r_\oplus^2} \sum_{k=1}^{N} \mathbf{r}_k \cdot \mathbf{u}(\mathbf{r}_k) \tag{3.3b}$$

$$\mathbf{R}_{\mathrm{CN}} = \frac{1}{N} \frac{3}{2r_\oplus^2} \sum_{k=1}^{N} \mathbf{r}_k \times \mathbf{u}(\mathbf{r}_k) \tag{3.3c}$$

The derivations of these equations, likewise, closely follow those for the CF frame parameters in Appendix B.2, with appropriate modifications to reflect the discreteness of the sampling network.

To highlight the structural similarity of these formulae, we define the auxiliary fields

$$\mathbf{w}(\mathbf{r}) = \frac{3}{2} \frac{\mathbf{r} \times \mathbf{u}(\mathbf{r})}{r_\oplus^2} \tag{3.4a}$$

$$s(\mathbf{r}) = \frac{\mathbf{r} \cdot \mathbf{u}(\mathbf{r})}{r_\oplus^2} \tag{3.4b}$$

so that the formulae can be summarised as

$$\mathbf{T}_{\mathrm{CF}} = \frac{1}{4\pi}\int_{\partial\oplus} \mathbf{u}\, d\Omega, \qquad D_{\mathrm{CF}} = \frac{1}{4\pi}\int_{\partial\oplus} s\, d\Omega, \qquad \mathbf{R}_{\mathrm{CF}} = \frac{1}{4\pi}\int_{\partial\oplus} \mathbf{w}\, d\Omega \tag{3.5a}$$

$$\mathbf{T}_{\mathrm{CN}} = \frac{1}{N}\sum_{k=1}^{N}\mathbf{u}(\mathbf{r}_k), \qquad D_{\mathrm{CN}} = \frac{1}{N}\sum_{k=1}^{N}s(\mathbf{r}_k), \qquad \mathbf{R}_{\mathrm{CN}} = \frac{1}{N}\sum_{k=1}^{N}\mathbf{w}(\mathbf{r}_k) \tag{3.5b}$$

It is then apparent that all of them have the generic form of stochastic expectation values.

3.1.2 Transformation method

The transformation method has the advantage of solving for all the Helmert parameters simultaneously to minimise the error in the transformed coordinates of a set of stations between the two frames. In this approach, each station contributes three equations to the (over-determined) linear system to solve,

$$\mathbf{u}_k = \left[\begin{array}{c:c:c} & & \\ I & \mathbf{r} & r^{\times} \\ & & \end{array}\right]_k \left[\begin{array}{c} \mathbf{T} \\ \hdashline D \\ \hdashline \mathbf{R} \end{array}\right]_{\mathrm{CN}} \tag{3.6}$$

where I is the 3×3 identity matrix, $\mathbf{u}_k = \mathbf{u}(\mathbf{r}_k)$,

$$\mathbf{r}_k = \begin{bmatrix} x \\ y \\ z \end{bmatrix}_k \tag{3.7}$$

is the position of the kth station as a 3×1 matrix, and

$$r_k^{\times} = \begin{bmatrix} 0 & z & -y \\ -z & 0 & x \\ y & -x & 0 \end{bmatrix}_k \tag{3.8}$$

is a 3×3 matrix representing the cross product operation with $\mathbf{r}_k$. We recall from Equations 2.3 and 2.5 that the sum of the displacement fields associated with the instantaneous HPs is

$$\mathbf{v} = \mathbf{v}_T + \mathbf{v}_D + \mathbf{v}_R = \mathbf{T}_{\mathrm{CN}} + D_{\mathrm{CN}}\,\mathbf{r} + \mathbf{R}_{\mathrm{CN}} \times \mathbf{r} \tag{3.9}$$

and therefore, the system is equivalent to

$$\mathbf{u}_k = \mathbf{v}_k \tag{3.10}$$

with $\mathbf{v}_k = \mathbf{v}(\mathbf{r}_k)$, and the goal is to minimise $\sum_{k=1}^{N} \left(\mathbf{u}_k - \mathbf{v}_k\right)^2$. If we now form the design matrix as in *Altamimi et al.* [2002],

$$A = \left[\begin{array}{c:c:c} I & \mathbf{r}_1 & r_1^{\times} \\ \vdots & \vdots & \vdots \\ I & \mathbf{r}_N & r_N^{\times} \end{array}\right] \tag{3.11}$$

then the error is minimised for

$$\left[\begin{array}{c} \mathbf{T} \\ \hdashline D \\ \hdashline \mathbf{R} \end{array}\right]_{\text{CN}} = (A^T A)^{-1} A^T \left[\begin{array}{c} \mathbf{u}_1 \\ \vdots \\ \mathbf{u}_N \end{array}\right] \tag{3.12}$$

which is our required solution.

If we want to associate weights to displacement measurements, we have to replace $(A^T A)^{-1} A^T$ in Equation 3.12 with $(A^T W A)^{-1} A^T W$ where W is a weight matrix. The ITRF considers the choice of $W = \Sigma^{-1}$ where Σ is the covariance matrix of the displacement observations, whereas in Section 3.6 we will consider weights proportional to the area of the Earth surface that a station represents. Of course, these choices may also be combined by taking the product of the corresponding matrices.

Note that the transformation method can minimise the error in transformation much more effectively than the summation method which only considers the HPs one at a time. For small networks, the transformation method is therefore more accurate. However, it can be plausibly argued [see, for example *Zhou et al.*, 2016] that their difference diminishes as the network grows, since both of the CN frames ultimately converge to the CF frame.

In contrast to the summation method, a direct statistical interpretation is not available for the CN parameters obtained by the transformation method. However, bearing in mind that both of the methods calculate the same physical quantities, we will be able to apply the formalism we develop in the next section for the summation method to the transformation method as well.

3.2 Stochastic interpretation of the CN frame

In Equation 3.5, the CF parameters may be regarded as the continuous averages of the $\mathbf{u}(\mathbf{r})$, the $s(\mathbf{r})$, and the $\mathbf{w}(\mathbf{r})$ fields taken over the entire Earth surface, whereas the corresponding CN parameters may be viewed as the discrete averages for a particular discrete sampling of the respective fields.

We note that we may interpret $\mathbf{u}$, s, or $\mathbf{w}$ as stochastic observables, that is, random variables, where the station position $\mathbf{r}$ is chosen at random. The probability of an observation point $\mathbf{r}$ being sampled here is taken to be uniform over the surface of the Earth. This interpretation arises naturally in the theory of Monte Carlo integration. If we were to evaluate the CF parameters in Equation 3.5a using Monte Carlo techniques, we would keep calculating the cumulative averages of the fields evaluated at randomly picked points until satisfactory convergence was reached. This convergence is guaranteed by the Law of Large Numbers (LLN) of probability theory.

The expectation value of any function $X(\mathbf{r})$ on the surface of the Earth with respect to this probability distribution is then

$$\langle X \rangle = \frac{1}{4\pi} \int_{\partial \oplus} X \, d\Omega \tag{3.13}$$

We will use the notations $\langle X \rangle$ and $\mathrm{mean}(X)$ for the expectation value, that is, the population mean, interchangeably. Note that we indeed have a probability distribution here since

$$\langle 1 \rangle = \frac{1}{4\pi} \int_{\partial \oplus} d\Omega = 1 \tag{3.14}$$

Thus Equation 3.5a may be re-written as

$$\mathbf{T}_{\mathrm{CF}} = \langle \mathbf{u} \rangle \tag{3.15a}$$

$$D_{\mathrm{CF}} = \langle s \rangle \tag{3.15b}$$

$$\mathbf{R}_{\mathrm{CF}} = \langle \mathbf{w} \rangle \tag{3.15c}$$

In other words, $\mathbf{T}_{\mathrm{CF}}$, D_{CF}, and $\mathbf{R}_{\mathrm{CF}}$ are the population mean, that is, the distribution mean of the random variables $\mathbf{u}$, s, and $\mathbf{w}$ respectively.

Next, we consider our geodetic network itself to be a random sampling of sample size N. This simplifying assumption perhaps needs justification since the station network configuration in reality is somewhat fixed. Our justification for it here is that, for instance, the locations of the earthquake epicentres are rather unpredictable and are not strongly correlated with the geodetic site locations. Thus in the epicentral coordinate system the locations of the geodetic stations may instead be regarded as randomly chosen. For the surface water loading case, this assumption may be rationalized through our expectation that the locations of the geodetic sites are not strongly correlated with the locations of hydrologically active regions. The validation of this expectation is ultimately provided by our results reported in Chapter 5.

Under this assumption, $\mathbf{T}_{\mathrm{CN}}$, D_{CN}, and $\mathbf{R}_{\mathrm{CN}}$ are themselves random variables. Their probability distributions are called, in this context, the sampling distributions of the sample means. It follows that

$$\langle \mathbf{T}_{\mathrm{CN}} \rangle = \mathbf{T}_{\mathrm{CF}} \tag{3.16a}$$

$$\langle D_{\mathrm{CN}} \rangle = D_{\mathrm{CF}} \tag{3.16b}$$

$$\langle \mathbf{R}_{\mathrm{CN}} \rangle = \mathbf{R}_{\mathrm{CF}} \tag{3.16c}$$

where definition of the expectation value in Equation 3.13 has been generalised to several observation points,

$$\langle X \rangle = \frac{1}{(4\pi)^N} \int_{\partial\oplus} \dots \int_{\partial\oplus} X(\mathbf{r}_1, \dots, \mathbf{r}_N)\, d\Omega_1 \dots d\Omega_N \tag{3.17}$$

3.3 Expected bias as standard deviation

We are however primarily interested in the network effect, that is, the deviation of a CN parameter from its corresponding CF parameter. Fortunately, a fundamental theorem of probability theory lets us estimate this deviation.

Central Limit Theorem. *Let $\{X_1, \dots, X_N\}$ be a set of independent and identically distributed random variables, that is, a random sample, drawn from a distribution with population mean μ and standard deviation σ. Then as N increases, the sampling*

distribution of the sample mean

$$\overline{X}_N = \frac{1}{N}\sum_{k=1}^{N} X_k$$

approaches the normal distribution with mean μ and standard deviation $\sigma/\sqrt{N}$.

In our case, the random variable X is any of the components of the fields $\mathbf{u}$, s, or $\mathbf{w}$. The population mean μ is the corresponding CF parameter, and the sample mean $\overline{X}_N$ is the respective CN parameter,

$$\mathbf{T}_{\mathrm{CN}} = \overline{\mathbf{u}}_N \tag{3.18a}$$

$$D_{\mathrm{CN}} = \overline{s}_N \tag{3.18b}$$

$$\mathbf{R}_{\mathrm{CN}} = \overline{\mathbf{w}}_N \tag{3.18c}$$

Thus, the network effect in the notation of the theorem is $\overline{X}_N - \mu$. As expected for an error term, its population mean is zero by Equation 3.16.

The standard deviation of the network effect therefore provides a natural measure of the expected magnitude of the network effect. Since

$$\mathrm{std}(\overline{X}_N - \mu) = \mathrm{std}(\overline{X}_N) \tag{3.19}$$

this measure is the same as the standard deviation of the sample mean itself and, therefore, we define the expected biases in the Helmert parameters to be,

$$\Delta T = \mathrm{std}(\mathbf{T}_{\mathrm{CN}}) \tag{3.20a}$$

$$\Delta D = \mathrm{std}(D_{\mathrm{CN}}) \tag{3.20b}$$

$$\Delta R = \mathrm{std}(\mathbf{R}_{\mathrm{CN}}) \tag{3.20c}$$

where $\mathrm{std}(X)$ denotes the standard deviation of a random variable X. The Central Limit Theorem (CLT) guarantees that the expected bias scales as $1/\sqrt{N}$, that is, for large N,

$$\Delta T \approx \frac{\mathrm{std}(\mathbf{u})}{\sqrt{N}} \tag{3.21a}$$

$$\Delta D \approx \frac{\mathrm{std}(s)}{\sqrt{N}} \tag{3.21b}$$

$$\Delta R \approx \frac{\mathrm{std}(\mathbf{w})}{\sqrt{N}} \tag{3.21c}$$

It is instructive here to view the CF frame parameters to be the sample means when the network is infinite and uniformly distributed so that there is no error associated with network bias.

This scaling may also be understood from an alternative viewpoint. Here, the value of a field at a single point is regarded as a measurement of the corresponding CF parameter. Then the deviation of that measurement from the true value of the CF parameter may be regarded as the error in that measurement. For N such points that are randomly chosen, the sum of these uncorrelated errors may be interpreted as a random walk of N steps. Probability theory than predicts that this sum scales as $\sqrt{N}$ and, therefore, the average of these N errors scales as $1/\sqrt{N}$.

This measure of the NE can in principle be applied to any theoretical model for crustal deformation. Besides the geodynamical processes investigated in this thesis, it could also be applied to postseismic rebound, atmospheric loading, or tectonic plate motion, for instance, to assess the agreement between the prediction of the GC motion by their theoretical models and the space geodetic observations. Such validation of geophysical models against space geodetic observations have been increasingly useful to researchers [see, for example, *Xu and Chao*, 2015].

The expected bias may be interpreted as the statistical uncertainty, or the expected error, in the determination of model-predicted GC motion due to the finite size and unevenness of the geodetic networks. Moreover, since it ignores the details of the configuration of the observing network except for the size, we may also regard it as a formal error associated with the crustal deformation model itself due to discrete sampling.

Furthermore, it is often desirable for the stability of the RF to realise it using sites that have relatively higher reliability and consistency, longer timespan of operation, and weaker non-linear signals in their motion. However, as our criteria for selection of sites get stricter, the choice of sites becomes increasingly more restricted. A possible application of the expected bias is to decide on the optimal size of the network that ensures that the NE does not overwhelm the advantages of a strict selection criteria.

In addition, geodetic observations are often compatible with ranges of values for the input parameters of a model such as, for example, the fault slip model of an earthquake. In that case the deterministic calculation of the NE might not be useful.

However, our stochastic approach to estimate the NE could still be applied here to obtain a measure of the expected error associated with it, and thereby, to partially validate its prediction for the GC motion. Likewise, this approach may also be useful when the spatio-temporal domain of applicability of a model is incomplete.

3.4 Analytical formula for the expected bias

As defined in Equation 3.20, the expected bias in a Helmert parameter of transformation is the standard deviation of its probability distribution. The generality of this definition allows it to be applicable to the different methods (summation and transformation) of determining the different kinds (instantaneous and time-dependent) of Helmert parameters of the geometric Centre of Network (CN) frame as well as of the Centre of Weighted Network (CWN) frame that we will introduce in Section 3.6.

The $1/\sqrt{N}$ scaling of the expected bias with the network size N is extremely robust in that it applies to all of these variations. In fact, even though in theory this scaling is only applicable for large N, in reality, due to the magnitude of the surface displacement field being finite, it holds fairly well even for small N. We exploit this observation in this section to derive a set of formulae to calculate the expected bias of the HPs using Equation 3.21 from the vector spherical harmonics expansion of the displacement field. Although, strictly speaking, these formulae apply to the summation method and to the geometric CN frame, the difference between the expected bias values of the instantaneous HPs obtained using various methods quickly diminishes with increasing network size.

We, therefore, need to calculate $\mathrm{std}(X)$ where the random variable X stands for any of the component of the fields $\mathbf{u}$, s, or $\mathbf{w}$. Equivalently, we may calculate its square, that is, the variance of the random variable X,

$$(\mathrm{std}(X))^2 = \mathrm{var}(X) \tag{3.22a}$$
$$= \langle (X - \langle X \rangle)^2 \rangle \tag{3.22b}$$
$$= \langle X^2 \rangle - \langle X \rangle^2 \tag{3.22c}$$

where $\langle X \rangle$ is the corresponding CF frame parameter that we calculated from the degree-0 and the degree-1 components of the corresponding field in Equation 2.14

of Section 2.4.

Therefore we have,

$$\mathrm{var}(\mathbf{u}) = \frac{1}{4\pi}\int_{\partial\oplus} \mathbf{u}^2\, d\Omega - \mathbf{T}_{\mathrm{CF}}^2 \tag{3.23a}$$

$$\mathrm{var}(s) = \frac{1}{4\pi}\int_{\partial\oplus} s^2\, d\Omega - D_{\mathrm{CF}}^2 \tag{3.23b}$$

$$\mathrm{var}(\mathbf{w}) = \frac{1}{4\pi}\int_{\partial\oplus} \mathbf{w}^2\, d\Omega - \mathbf{R}_{\mathrm{CF}}^2 \tag{3.23c}$$

where it can be shown that, in the notation of Chapter 2,

$$\frac{1}{4\pi}\int_{\partial\oplus} \mathbf{u}^2\, d\Omega = \frac{1}{4\pi}\sum_{n,m} |y^S_{1,nm}(r_\oplus)|^2 + n(n+1)\left(|y^S_{3,nm}(r_\oplus)|^2 + |y^T_{1,nm}(r_\oplus)|^2\right) \tag{3.24a}$$

$$\frac{1}{4\pi}\int_{\partial\oplus} s^2\, d\Omega = \frac{1}{4\pi\, r_\oplus^2}\sum_{n,m} |y^S_{1,nm}(r_\oplus)|^2 \tag{3.24b}$$

$$\frac{1}{4\pi}\int_{\partial\oplus} \mathbf{w}^2\, d\Omega = \frac{9}{16\pi\, r_\oplus^2}\sum_{n,m} n(n+1)\left(|y^S_{3,nm}(r_\oplus)|^2 + |y^T_{1,nm}(r_\oplus)|^2\right) \tag{3.24c}$$

by the orthogonality property of the spherical harmonics. Here, as before, the y_1^S and y_3^S functions are the coefficients of the spheroidal modes, and the y_1^T functions are the coefficients of the toroidal modes, evaluated at the Earth surface. See Appendix B.6 for the derivation of these formulae.

It is interesting to note that even though the CF frame parameters depend on the degree-0 and the degree-1 modes only, the sampling bias gets contributions from all the modes. In other words, the other modes alias into the measurement of the CN frame parameters through the finiteness of the observation network [*Wu et al.*, 2002]. Also, whereas the GC motion corresponds to transformations that preserve the shape of the surface of the Earth except for an overall scaling, the expected bias is a measure of the power of the deformation of the shape of the Earth surface.

However, these formulae are applicable only when the entire surface of the Earth contributes to the expected bias. In Section 4.5, we will exclude a spherical cap surrounding the earthquake epicentre from the calculation of the expected bias in order to remove the influence of the near field. It then becomes necessary to

construct the sampling distribution itself so as to evaluate the expected bias as its standard deviation.

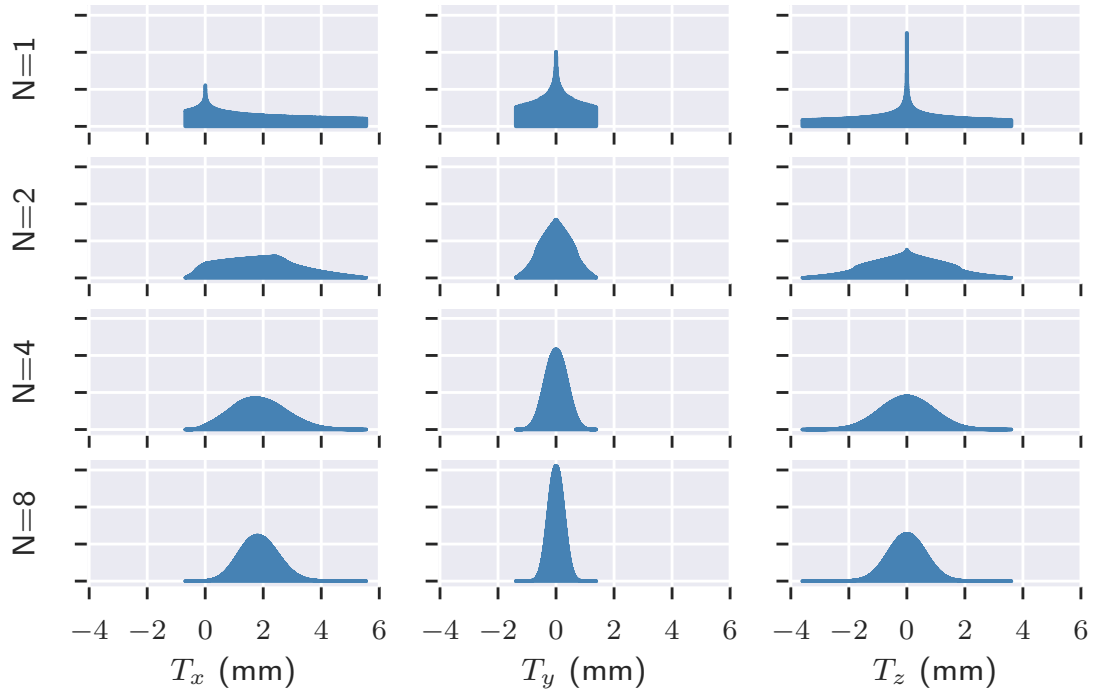

Figure 3.1: The distributions of the Cartesian components of the contributions from the degree-1 modes to $\mathbf{T}_{\mathrm{CN}}$ with varying network size N. The example coseismic field is due to the point source $M_{\text{dc-1}}$ at a depth of 10 km. Although only the x-component has a non-zero mean of 1.85 mm, all the components contribute significantly to the network effect, as can be seen by the comparable width of the distributions for all three components. Note that as the network size increases, the distributions approach normal distributions of increasingly narrower widths.

Therefore, we now present a construction that allows us to build up the sampling distribution of the sample means from the probability distribution of the fields. In practice, it is probably more convenient to apply the following construction to discretised and normalised frequency distributions instead of probability distribution functions (PDFs). We illustrate this construction for an example displacement field in Figure 3.1.

As before, we choose a random variable X, with the PDF p_X, that may stand for

any component of the $\mathbf{u}$, the s, or the $\mathbf{w}$ fields, for notational convenience. For a random sampling of X by a network of size N, the measurements $X_k = X(\mathbf{r}_k)$, where $1 \leq k \leq N$, all share the same PDF p_X. Since these measurements are independent, probability theory dictates that the PDF of their sum $S = \sum_k X_k$ is the convolution of their PDFs. That is,

$$p_S = \underbrace{p_X * \ldots * p_X}_{N \text{ times}} \tag{3.25}$$

where $*$ denotes convolution. The PDF of the sampling mean $\overline{X} = S/N$ is given by

$$p_{\overline{X}}(x) = N\ p_S(Nx) \tag{3.26}$$

by a simple re-scaling that preserve the total probability. From the sampling distribution $p_{\overline{X}}$, the expected bias ΔX may be calculated immediately as its standard deviation.

To summarise, to calculate the expected bias for network size N, we may want to proceed by partitioning the surface of the Earth into a large number of equal area pieces, evaluate the displacement field $\mathbf{u}$, and thereby s and $\mathbf{w}$, on one representative point per piece, using the crustal deformation model we are considering. We then aggregate the data to form a frequency distribution for each component of the fields. Then, after convolving the distribution with itself N times and a final re-scaling of the distribution by $1/N$, we obtain the frequency distributions of $\mathbf{T}_{\text{CN}}$, D_{CN}, and $\mathbf{R}_{\text{CN}}$ respectively. The expected biases ΔT, ΔD, and ΔR will then be the standard deviations of these distributions that follow the $1/\sqrt{N}$ scaling (Figure 3.2).

Note that although this construction is computationally more expensive than the analytical formulae in Equations 3.23 and 3.24, the vector spherical harmonics expansion form for the displacement field is not required for it to be applicable. Only the values of the displacement field evaluated on a sufficiently dense set of points are necessary.

3.5 Time-dependent case

Now we consider extensions of these methods to time-dependent deformation processes. The case study for the methods introduced here will be the elastic

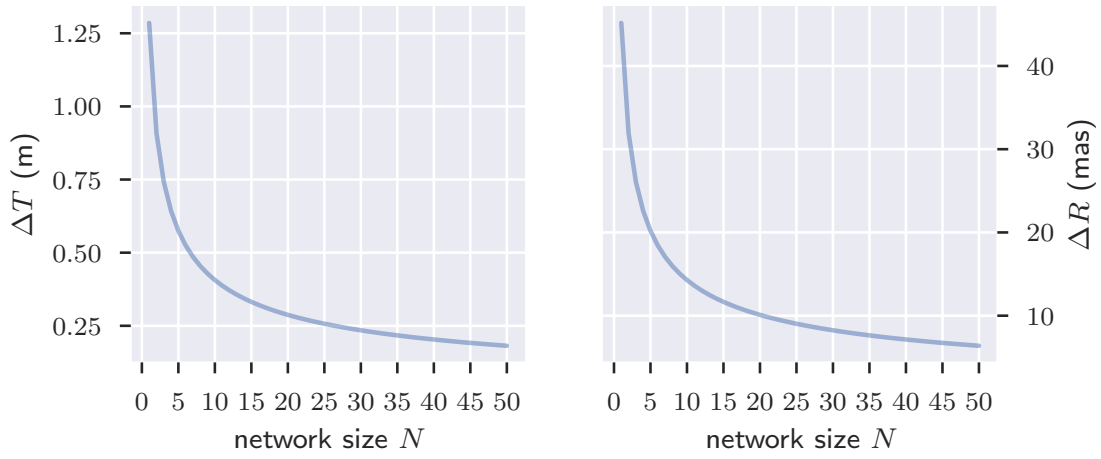

Figure 3.2: The dependence of the expected bias on the network size N. The standard deviations of $\mathbf{T}_{\mathrm{CN}}$ (left) and $\mathbf{R}_{\mathrm{CN}}$ (right) scales as $1/\sqrt{N}$. The seismic source of the example coseismic displacement field here is $M_{\text{dc-1}}$ at a depth of 10 km.

deformation due to surface water mass movements that we investigate in Chapter 5.

3.5.1 Transformation method

According to the transformation method, for a timeseries of station positions at a discrete set of epochs t_j, the Helmert parameters may be estimated by a least square fit to the set of over-determined equations

$$\mathbf{u}_{j,k} = \left[\begin{array}{c:c:c:c:c:c} I & \mathbf{r} & r_k^{\times} & \delta t_j I & \delta t_j \mathbf{r} & \delta t_j r_k^{\times} \end{array}\right] \left[\begin{array}{c} \mathbf{T} \\ \hdashline D \\ \hdashline \mathbf{R} \\ \hdashline \dot{\mathbf{T}} \\ \hdashline \dot{D} \\ \hdashline \dot{\mathbf{R}} \end{array}\right]_{\mathrm{CN}} \tag{3.27}$$

in the notation of Equation 3.6. Here, $\delta t_j = t_j - t_{\mathrm{ref}}$ for some reference epoch t_{ref}, $\mathbf{u}_{j,k}$ is the displacement of the station with index k at the epoch with index j,

$\dot{\mathbf{T}}_{\text{CN}}$ and $\dot{\mathbf{R}}_{\text{CN}}$ are the linear velocity and angular velocity parameters respectively, and $\dot{D}_{\text{CN}}$ is the rate of scale change. This is a specialised form of the more general set of equations given in *Altamimi et al.* [2002] that also incorporates velocity measurements at the stations.

Hence we adapt the procedure outlined in Section 3.1.2 to also tackle the time-dependent case here. That is, we stack the equations for the components of $\mathbf{u}_{j,k}$ together in some specified order to form the design matrix A, and our solution for the CN frame parameters are obtained by applying the matrix $(A^T W A)^{-1} A^T W$ to the column matrix formed by the components of $\mathbf{u}_{j,k}$ in the same order. Here, as before, W is an optional matrix that may assign weights to the observations $\mathbf{u}_{j,k}$. For the unweighted case, W may be taken to be the identity matrix.

3.5.2 Summation method

For the time-dependent case, an analogue of the summation method may also be constructed as follows. Suppose the endpoints of the relevant time intervals are $\tau_0, \tau_1, \ldots, \tau_p$, where p is the number of intervals, and the epochs at which the observations were carried out are the midpoints of these intervals $t_j = \frac{1}{2}\left(\tau_{j-1} + \tau_j\right)$. Then for any function f evaluated at these epochs, $f_j = f(t_j)$, we define the (weighted) time average:

$$[\![f]\!] = \frac{1}{\tau_p - \tau_0} \sum_{j=1}^{p} f_j \Delta t_j \tag{3.28}$$

where $\Delta t_j = \tau_j - \tau_{j-1}$ is the length of the jth interval.

Here, the secular translational geocentre motion is modelled by

$$\mathbf{T}_{\text{model}}(t) = \mathbf{T}_{\text{CN}} + (t - t_{\text{ref}})\dot{\mathbf{T}}_{\text{CN}} \tag{3.29}$$

The parameters $\mathbf{T}_{\text{CN}}$ and $\dot{\mathbf{T}}_{\text{CN}}$ are estimated by minimising the time-averaged deviation $[\![\left(\mathbf{T} - \mathbf{T}_{\text{model}}\right)^2]\!]$ where $\mathbf{T}_j$ is the instantaneous CN at the epoch with index j,

$$\mathbf{T}_j = \frac{1}{N} \sum_{k=1}^{N} \mathbf{u}_{j,k} \tag{3.30}$$

We employ simple linear regression theory to solve for the CN parameters. The results are,

$$\mathbf{T}_{\mathrm{CN}} = [\![\mathbf{T}]\!] \tag{3.31a}$$

$$\dot{\mathbf{T}}_{\mathrm{CN}} = \frac{[\![(\mathbf{T}-[\![\mathbf{T}]\!])(t-[\![t]\!])]\!]}{[\![(t-[\![t]\!])^2]\!]} = \frac{\underline{\mathrm{cov}}(\mathbf{T},t)}{\underline{\mathrm{var}}(t)} \tag{3.31b}$$

by choosing $t_{\mathrm{ref}} = [\![t]\!]$, where the underlined operators $\underline{\mathrm{cov}}$ and $\underline{\mathrm{var}}$ denote the (weighted) covariance and variance in time. To facilitate direct comparison of results with the transformation method, we make the same choice of t_{ref} for both of the methods in Chapters 4 and 5. Similarly,

$$\mathbf{R}_{\mathrm{CN}} = [\![\mathbf{R}]\!] \tag{3.32a}$$

$$\dot{\mathbf{R}}_{\mathrm{CN}} = \frac{[\![(\mathbf{R}-[\![\mathbf{R}]\!])(t-[\![t]\!])]\!]}{[\![(t-[\![t]\!])^2]\!]} = \frac{\underline{\mathrm{cov}}(\mathbf{R},t)}{\underline{\mathrm{var}}(t)} \tag{3.32b}$$

$$D_{\mathrm{CN}} = [\![D]\!] \tag{3.32c}$$

$$\dot{D}_{\mathrm{CN}} = \frac{[\![(D-[\![D]\!])(t-[\![t]\!])]\!]}{[\![(t-[\![t]\!])^2]\!]} = \frac{\underline{\mathrm{cov}}(D,t)}{\underline{\mathrm{var}}(t)} \tag{3.32d}$$

where

$$\mathbf{R}_j = \frac{1}{N}\sum_{k=1}^{N}\mathbf{w}_{j,k} \tag{3.33}$$

$$D_j = \frac{1}{N}\sum_{k=1}^{N}s_{j,k} \tag{3.34}$$

are the instantaneous shift in orientation and the instantaneous change in scale of the CN frame.

We note that Geoffrey Blewitt suggested (in personal communication) that yet another alternative method for calculating the time-dependent HPs would be to use Theil-Sen estimators that may be more robust due to their reduced sensitivity to outliers.

3.6 Voronoi decomposition of Earth surface

As discussed before, the average of a random variable X over the Earth surface

$$\langle X\rangle = \frac{1}{4\pi}\int_{\partial\oplus} X\, d\Omega \tag{3.35}$$

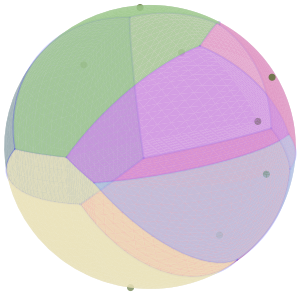

Figure 3.3: Voronoi decomposition of the surface of the sphere. The 8 illustrative stations are shown in green dots.

may be discretised as

$$\overline{X} = \frac{1}{N}\sum_{k=1}^{N} X(\mathbf{r}_k) \tag{3.36}$$

However, if the symbol $d\Omega$ in the former equation is interpreted to be the differential area on the unit sphere, then this form also suggests another natural discretisation,

$$\overline{X} = \frac{1}{A_\oplus}\sum_{k=1}^{N} X(\mathbf{r}_k) A_k \tag{3.37}$$

where $A_\oplus = 4\pi r_\oplus^2$ is the surface area of the Earth, and A_k is the surface area assigned to the station with index k. That is, we assign a weight proportional to the area of the surface of the Earth that a station represents to its measurements.

Here we investigate one such choice of the weight: the area of the Voronoi cell of the station. We will call the resulting frame the Centre of Weighted Network

(CWN) frame. Thus the CWN frame parameters are:

$$\mathbf{T}_{\text{CWN}} = \sum_{k=1}^{N} \mathbf{u}(\mathbf{r}_k) \frac{A_k}{A_\oplus} \tag{3.38a}$$

$$D_{\text{CWN}} = \sum_{k=1}^{N} s(\mathbf{r}_k) \frac{A_k}{A_\oplus} \tag{3.38b}$$

$$\mathbf{R}_{\text{CWN}} = \sum_{k=1}^{N} \mathbf{w}(\mathbf{r}_k) \frac{A_k}{A_\oplus} \tag{3.38c}$$

where A_k is the area of the Voronoi cell surrounding the station with index k.

For a fixed set of N stations, the Voronoi cell [*Voronoi*, 1908] corresponding to a particular station is the set of points on the surface closer to that station than any other station (Figure 3.3). Here, the distance between two points on the sphere is their great-circle distance. Thus the surface of the sphere is partitioned into N cells, one for each station, that are spherical polygons whose sides are arcs of great circles. The areas of these polygons are our required weights.

The geometric CWN frame also has a natural transformation method variant. As noted before, the form of Equation 3.12 makes it straightforward to associate weights to the displacement measurements by specifying a weight matrix. In this case the weight matrix takes the form

$$W = \begin{bmatrix} A_1 & & & & & & \\ & A_1 & & & & & \\ & & A_1 & & & & \\ & & & \ddots & & & \\ & & & & A_N & & \\ & & & & & A_N & \\ & & & & & & A_N \end{bmatrix} \tag{3.39}$$

where the blank entries are filled with zero. That is, it is a diagonal matrix consisting of the areas of the Voronoi cells surrounding the stations. Each area is repeated three times, once for each of the three components of the displacement vector recorded at the station.

Our motivation for this modification to the CN frame comes from the discrepancy in spatial coverage between the continents. For instance, the coverage of Europe

by geodetic stations in general is considerably better than that of Africa. As a result, the GC motion signal calculated using the CN frame for a hypothetical earthquake in Europe would be disproportionately more pronounced than a similar earthquake in Africa. However, since in the CWN frame the European stations would on an average be assigned smaller weights compared to the African stations, we expect this bias to be partly compensated by this modification.

In Chapters 4 and 5 we will compare the merits of using the CN frame and the CWN frame for GC motion determination by space geodetic techniques.

Chapter 4

Coseismic deformation by great earthquakes

In this chapter, we investigate the geocentre (GC) motion caused by the coseismic displacement field due to great earthquakes, as well as the associated network effect (NE). As discussed in Section 2.5, our model for the elastic Earth here is the Preliminary Reference Earth Model (PREM) [*Dziewonski and Anderson*, 1981], and our method for calculating the deformation field is the normal mode summation method [*Pollitz*, 1996; *Sun and Dong*, 2014].

In Section 4.1, we tabulate the values of the shifts in instantaneous Helmert parameters (HPs) of the Centre of Figure (CF) frame with respect to the inertial Centre of Mass (CM) frame for four basic kinds of seismic sources (one isotropic, two double couples, and one compensated linear vector dipole) of moment magnitude 9.0 at various source depths. As explained in Section 2.5.3, it is possible to calculate the displacement field due to any seismic point source from the displacement fields created by these four sources. We also tabulate and compare the values of the expected bias in these parameters obtained by employing different methods.

Next, in Section 4.2, we introduce the simplified fault slip models that we use for the two great earthquakes that we study in this chapter: the 2004 Sumatra–Andaman earthquake and the 2011 Tōhoku–Oki earthquake. In Sections 4.3 and 4.4 we evaluate the effectiveness of the expected bias introduced in Chapter 3 as a measure of the error introduced by the NE. To this end, we calculate the coseismic displacement field at the stations of three illustrative geodetic networks to obtain

the observed shifts in their Centre of Network (CN) parameters.

Then, in Section 4.5, we will address the issue of our method over-estimating the NE for networks located in the far field due to the localised nature of the coseismic field. We will show that the effect of constructing a network with only the sites that were relatively unaffected by the earthquake can be modelled by excluding an epicentral zone from consideration for the sites of the random network in the calculation of the expected bias.

Finally, in Section 4.6, we summarise our results for the application of the Centre of Weighted Network (CWN) frame in GC motion detection for the coseismic case.

4.1 Deformation due to simple point sources

The point sources we consider in this section have the linearly independent moment tensors from Equations 2.64, 2.65, and 2.66:

$$M_{\text{iso}} = \frac{M_0}{\sqrt{3}} \begin{bmatrix} 1 & 0 & 0 \\ 0 & 1 & 0 \\ 0 & 0 & 1 \end{bmatrix} \tag{4.1a}$$

$$M_{\text{dc-1}} = \frac{M_0}{\sqrt{2}} \begin{bmatrix} 0 & 1 & 0 \\ 1 & 0 & 0 \\ 0 & 0 & 0 \end{bmatrix} \tag{4.1b}$$

$$M_{\text{dc-2}} = \frac{M_0}{\sqrt{2}} \begin{bmatrix} 0 & 0 & 0 \\ 0 & 0 & 1 \\ 0 & 1 & 0 \end{bmatrix} \tag{4.1c}$$

$$M_{\text{clvd-1}} = \frac{M_0}{\sqrt{6}} \begin{bmatrix} 1 & 0 & 0 \\ 0 & -2 & 0 \\ 0 & 0 & 1 \end{bmatrix} \tag{4.1d}$$

with the same scalar moment M_0 [see, for example, *Stein and Wysession*, 2009, §4.4.5], chosen so that the moment magnitude M_W is 9.0. The tensors are expressed in the $\hat{\mathbf{r}}$-$\hat{\boldsymbol{\theta}}$-$\hat{\boldsymbol{\phi}}$ coordinates in the geographical spherical coordinate system or, equivalently, in the $\hat{\mathbf{z}}$-$\hat{\mathbf{x}}$-$\hat{\mathbf{y}}$ coordinates in the epicentral Cartesian coordinate system.

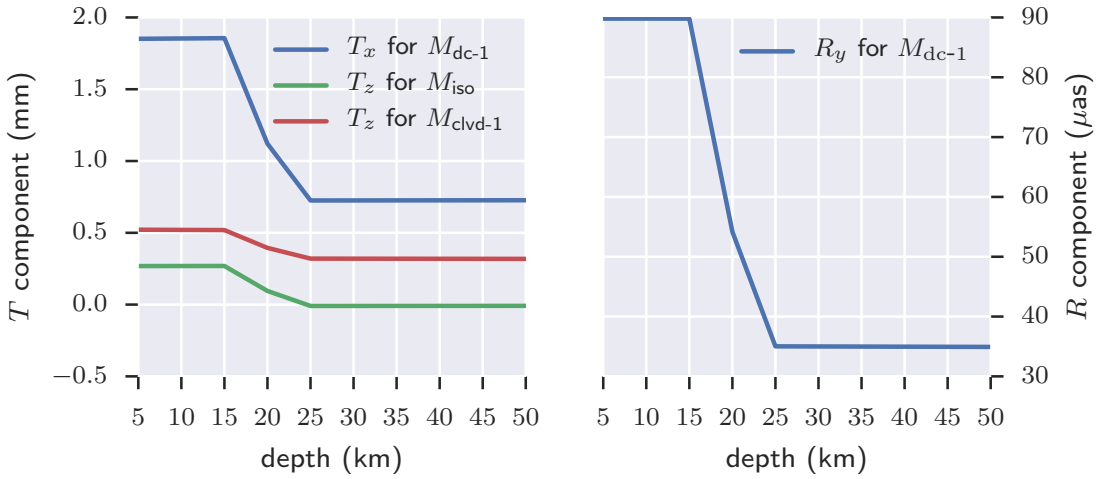

Figure 4.1: $\mathbf{T}_{\text{CF}}$ (left) and $\mathbf{R}_{\text{CF}}$ (right) as functions of the source depth for the reference set of point sources. Only the non-zero components are shown. The sharp transitions can be ascribed to the particular layer structure of the PREM.

In this section we will work in the epicentral coordinate system. We place the point source inside the Earth on the z-axis at r_s and compute the discontinuity in the $\mathbf{y}$ vector using Equations 2.75 and 2.76. As was explained in Section 2.5.2, we then propagate the regular solutions of the equations of motion (Equations 2.32 and 2.33) using Equation 2.55,

$$\mathbf{y}_{\text{reg}}(r_\oplus) = \Omega_N \, \Omega_{N-1} \, \ldots \, \Omega_3 \, \Omega_2 \, \mathbf{y}_{\text{reg}}(r_1) \tag{4.2}$$

as well as the discontinuity using Equation 2.56,

$$\mathbf{y}_{\text{disc}}(r_\oplus) = \Omega_N \, \Omega_{N-1} \, \ldots \, \Omega_{s+1} \, \Omega_s \, \Delta\mathbf{y} \tag{4.3}$$

to the Earth surface with the help of the matrizant matrices Ω_k. Then the unknown constants in the combined solution

$$\mathbf{y} = \mathbf{y}_{\text{reg}} + \mathbf{y}_{\text{disc}} \tag{4.4}$$

can be calculated from the free boundary conditions in Equation 2.58,

$$\text{spheroidal modes:} \quad y_2^S(r_\oplus) = y_4^S(r_\oplus) = 0 \tag{4.5a}$$

$$\text{toroidal modes:} \quad y_2^T(r_\oplus) = 0 \tag{4.5b}$$

For the degree-1 modes, however, as discussed in Section 2.4 and 2.5.5, these boundary conditions are degenerate, and have to be supplemented by Equation 2.18,

$$\int_0^{r_\oplus} \rho \left(y^S_{1,1,m} + 2y^S_{3,1,m} \right) r^2 \, dr = 0 \tag{4.6a}$$

$$\int_0^{r_\oplus} \rho \, y^T_{1,1,m} \, r^3 \, dr = 0 \tag{4.6b}$$

encoding the conservation of linear and angular momenta of the Earth system respectively, to obtain a complete solution.

4.1.1 Shifts in Helmert parameters

First, we consider the shifts in the CF frame parameters due to these sources. Because of the simple geometry of these sources, most of the Cartesian components of the CF parameters are identically zero in the epicentral coordinates. In Figure 4.1, we show the dependence on the source depth of the non-zero $\mathbf{T}_{\mathrm{CF}}$ and $\mathbf{R}_{\mathrm{CF}}$ parameters expressed in units of millimetres (mm) and micro-arc-seconds (μas) respectively. The scale parameters D_{CF} are not shown in the figure. Except the one for M_{iso}, they are also theoretically zero. It can be seen in the figure that within the crust (0–15 km depth) and within the mantle (> 25 km depth) the dependence of these parameters on the depth from the surface is relatively weak. However, their values rapidly decrease as the seismic source crosses the Mohorovičić (Moho) discontinuity at ∼15–25 km depth.

The shifts in the CF parameters for these seismic sources at selected depths are also tabulated in Tables 4.1, 4.2, 4.3, and 4.4 respectively. These values are calculated from the coefficients of the degree-0 and the degree-1 components of the displacement field by Equation 2.14,

$$\mathbf{T}_{\mathrm{CF}} = \frac{1}{4\pi} \sum_{m=-1}^{1} \left(y^S_{1,1,m}(r_\oplus) + 2y^S_{3,1,m}(r_\oplus) \right) \mathbf{\Delta}_m \tag{4.7a}$$

$$D_{\mathrm{CF}} = \frac{1}{\sqrt{4\pi} r_\oplus} y^S_{1,00}(r_\oplus) \tag{4.7b}$$

$$\mathbf{R}_{\mathrm{CF}} = \frac{3}{8\pi r_\oplus} \sum_{m=-1}^{1} 2y^T_{1,1,m}(r_\oplus) \mathbf{\Delta}_m \tag{4.7c}$$

source	depth	mean($\mathbf{u}$)	std($\mathbf{u}$)	mean(s)	std(s)	mean($\mathbf{w}$)	std($\mathbf{w}$)
		$\mathbf{T}_{\mathrm{CF}}$	$\Delta T\sqrt{N}$	D_{CF}	$\Delta D\sqrt{N}$	$\mathbf{R}_{\mathrm{CF}}$	$\Delta R\sqrt{N}$
	(km)	(mm)	(m)	(ppb)	(ppm)	(μas)	(mas)
M_{iso}	5	$0.268\,\hat{\mathbf{z}}$	0.837	0.080	0.093	$\mathbf{0}$	28.865
M_{iso}	10	$0.269\,\hat{\mathbf{z}}$	0.439	0.080	0.050	$\mathbf{0}$	14.557
M_{iso}	15	$0.269\,\hat{\mathbf{z}}$	0.344	0.080	0.042	$\mathbf{0}$	10.599
M_{iso}	20	$0.095\,\hat{\mathbf{z}}$	0.170	0.055	0.019	$\mathbf{0}$	5.820
M_{iso}	25	$-0.009\,\hat{\mathbf{z}}$	0.088	0.036	0.009	$\mathbf{0}$	3.262
M_{iso}	30	$-0.009\,\hat{\mathbf{z}}$	0.072	0.036	0.007	$\mathbf{0}$	2.660
M_{iso}	35	$-0.009\,\hat{\mathbf{z}}$	0.060	0.036	0.006	$\mathbf{0}$	2.237
M_{iso}	40	$-0.009\,\hat{\mathbf{z}}$	0.052	0.036	0.005	$\mathbf{0}$	1.923
M_{iso}	45	$-0.009\,\hat{\mathbf{z}}$	0.045	0.036	0.005	$\mathbf{0}$	1.683
M_{iso}	50	$-0.009\,\hat{\mathbf{z}}$	0.040	0.036	0.004	$\mathbf{0}$	1.492

Table 4.1: Statistics of the fields $\mathbf{u}$, s, and $\mathbf{w}$ of the point source M_{iso}. The means and the magnitude of the standard deviations are obtained using analytic formulae from the y function values at the surface.

source	depth	mean($\mathbf{u}$)	std($\mathbf{u}$)	mean(s)	std(s)	mean($\mathbf{w}$)	std($\mathbf{w}$)
		$\mathbf{T}_{\mathrm{CF}}$	$\Delta T\sqrt{N}$	D_{CF}	$\Delta D\sqrt{N}$	$\mathbf{R}_{\mathrm{CF}}$	$\Delta R\sqrt{N}$
	(km)	(mm)	(m)	(ppb)	(ppm)	(μas)	(mas)
$M_{\text{dc-1}}$	5	$1.851\,\hat{\mathbf{x}}$	2.072	0	0.158	$89.803\,\hat{\mathbf{y}}$	72.940
$M_{\text{dc-1}}$	10	$1.854\,\hat{\mathbf{x}}$	1.023	0	0.073	$89.813\,\hat{\mathbf{y}}$	37.929
$M_{\text{dc-1}}$	15	$1.856\,\hat{\mathbf{x}}$	0.756	0	0.054	$89.809\,\hat{\mathbf{y}}$	28.229
$M_{\text{dc-1}}$	20	$1.121\,\hat{\mathbf{x}}$	0.345	0	0.024	$54.169\,\hat{\mathbf{y}}$	13.017
$M_{\text{dc-1}}$	25	$0.725\,\hat{\mathbf{x}}$	0.190	0	0.013	$35.020\,\hat{\mathbf{y}}$	7.065
$M_{\text{dc-1}}$	30	$0.725\,\hat{\mathbf{x}}$	0.157	0	0.011	$35.000\,\hat{\mathbf{y}}$	5.815
$M_{\text{dc-1}}$	35	$0.726\,\hat{\mathbf{x}}$	0.134	0	0.010	$34.981\,\hat{\mathbf{y}}$	4.931
$M_{\text{dc-1}}$	40	$0.726\,\hat{\mathbf{x}}$	0.117	0	0.008	$34.962\,\hat{\mathbf{y}}$	4.275
$M_{\text{dc-1}}$	45	$0.726\,\hat{\mathbf{x}}$	0.103	0	0.008	$34.943\,\hat{\mathbf{y}}$	3.770
$M_{\text{dc-1}}$	50	$0.727\,\hat{\mathbf{x}}$	0.092	0	0.007	$34.924\,\hat{\mathbf{y}}$	3.369

Table 4.2: Statistics of the fields $\mathbf{u}$, s, and $\mathbf{w}$ of the point source $M_{\text{dc-1}}$. The means and the magnitude of the standard deviations are obtained using analytic formulae from the y function values at the surface.

source	depth	mean($\mathbf{u}$) $\mathbf{T}_{\mathrm{CF}}$	std($\mathbf{u}$) $\Delta T\sqrt{N}$	mean(s) D_{CF}	std(s) $\Delta D\sqrt{N}$	mean($\mathbf{w}$) $\mathbf{R}_{\mathrm{CF}}$	std($\mathbf{w}$) $\Delta R\sqrt{N}$
	(km)	(mm)	(m)	(ppb)	(ppm)	(μas)	(mas)
$M_{\text{dc-2}}$	5	$\mathbf{0}$	1.353	0	0.060	$\mathbf{0}$	60.251
$M_{\text{dc-2}}$	10	$\mathbf{0}$	0.606	0	0.030	$\mathbf{0}$	26.408
$M_{\text{dc-2}}$	15	$\mathbf{0}$	0.298	0	0.012	$\mathbf{0}$	13.434
$M_{\text{dc-2}}$	20	$\mathbf{0}$	0.203	0	0.008	$\mathbf{0}$	9.130
$M_{\text{dc-2}}$	25	$\mathbf{0}$	0.140	0	0.005	$\mathbf{0}$	6.450
$M_{\text{dc-2}}$	30	$\mathbf{0}$	0.114	0	0.004	$\mathbf{0}$	5.256
$M_{\text{dc-2}}$	35	$\mathbf{0}$	0.096	0	0.004	$\mathbf{0}$	4.422
$M_{\text{dc-2}}$	40	$\mathbf{0}$	0.083	0	0.003	$\mathbf{0}$	3.809
$M_{\text{dc-2}}$	45	$\mathbf{0}$	0.073	0	0.003	$\mathbf{0}$	3.341
$M_{\text{dc-2}}$	50	$\mathbf{0}$	0.065	0	0.002	$\mathbf{0}$	2.974

Table 4.3: Statistics of the fields $\mathbf{u}$, s, and $\mathbf{w}$ of the point source $M_{\text{dc-2}}$. The means and the magnitude of the standard deviations are obtained using analytic formulae from the y function values at the surface.

source	depth	mean($\mathbf{u}$) $\mathbf{T}_{\mathrm{CF}}$	std($\mathbf{u}$) $\Delta T\sqrt{N}$	mean(s) D_{CF}	std(s) $\Delta D\sqrt{N}$	mean($\mathbf{w}$) $\mathbf{R}_{\mathrm{CF}}$	std($\mathbf{w}$) $\Delta R\sqrt{N}$
	(km)	(mm)	(m)	(ppb)	(ppm)	(μas)	(mas)
$M_{\text{clvd-1}}$	5	$0.522\,\hat{\mathbf{z}}$	1.621	0.043	0.164	$\mathbf{0}$	57.853
$M_{\text{clvd-1}}$	10	$0.520\,\hat{\mathbf{z}}$	0.776	0.043	0.084	$\mathbf{0}$	26.199
$M_{\text{clvd-1}}$	15	$0.519\,\hat{\mathbf{z}}$	0.427	0.043	0.048	$\mathbf{0}$	13.980
$M_{\text{clvd-1}}$	20	$0.395\,\hat{\mathbf{z}}$	0.253	0.026	0.026	$\mathbf{0}$	9.005
$M_{\text{clvd-1}}$	25	$0.320\,\hat{\mathbf{z}}$	0.154	0.012	0.014	$\mathbf{0}$	6.077
$M_{\text{clvd-1}}$	30	$0.320\,\hat{\mathbf{z}}$	0.128	0.012	0.011	$\mathbf{0}$	4.986
$M_{\text{clvd-1}}$	35	$0.320\,\hat{\mathbf{z}}$	0.109	0.013	0.010	$\mathbf{0}$	4.218
$M_{\text{clvd-1}}$	40	$0.319\,\hat{\mathbf{z}}$	0.094	0.013	0.009	$\mathbf{0}$	3.649
$M_{\text{clvd-1}}$	45	$0.319\,\hat{\mathbf{z}}$	0.083	0.013	0.008	$\mathbf{0}$	3.212
$M_{\text{clvd-1}}$	50	$0.318\,\hat{\mathbf{z}}$	0.074	0.013	0.007	$\mathbf{0}$	2.867

Table 4.4: Statistics of the fields $\mathbf{u}$, s, and $\mathbf{w}$ of the point source $M_{\text{clvd-1}}$. The means and the magnitude of the standard deviations are obtained using analytic formulae from the y function values at the surface.

where the constant vectors $\boldsymbol{\Delta}_m$ are defined in Appendix B.1. Since the shifts in the HPs are linear in the displacement field, the GC motion for an arbitrary point source at these depths can be reconstructed from the information presented in the tables. Thus these tables summarise our computational results on the effects of fault geometry and fault depth on GC motion (translation $\mathbf{T}_{\mathrm{CF}}$, scale D_{CF}, rotation $\mathbf{R}_{\mathrm{CF}}$) for an Earth described by the PREM.

4.1.2 Source depth dependence of the expected bias

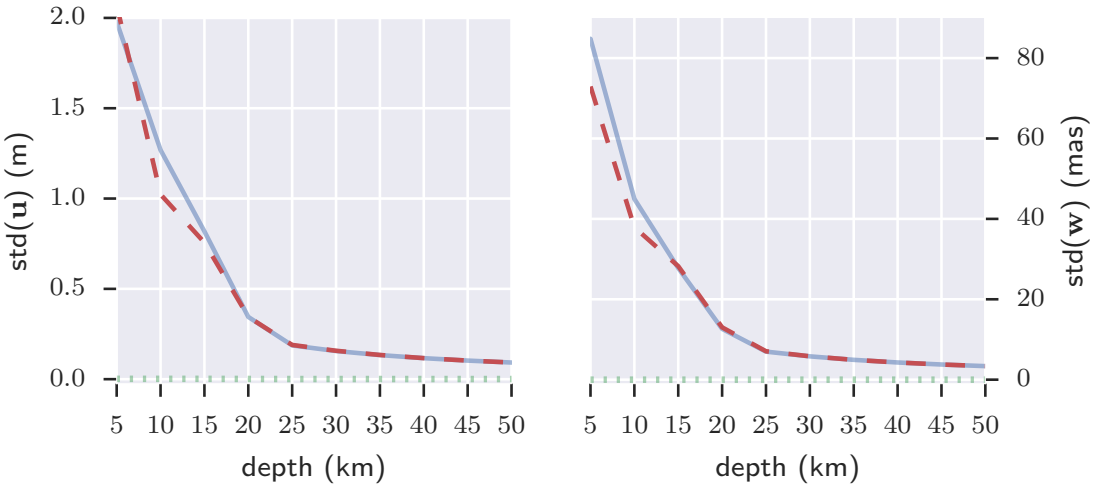

Figure 4.2: The standard deviations of $\mathbf{T}_{\mathrm{CN}}$ (left) and $\mathbf{R}_{\mathrm{CN}}$ (right), that is, the expected bias for network size $N = 1$, as functions of the source depth for the point source $M_{\text{dc-1}}$. Notice that the scales are 10^3 times that of Figure 4.1, and therefore, the mean values shown in green dotted lines are visually indiscernible from zero. The red dashed lines show the bias calculated using Equations 3.23 and 3.24, while the blue lines are obtained numerically.

These tables also contain the standard deviation of the $\mathbf{u}$, the s, and the $\mathbf{w}$ fields. Therefore, when the network size N is known, the expected bias in the HPs can

also be calculated from the tables using Equation 3.21:

$$\Delta T \approx \frac{\mathrm{std}(\mathbf{u})}{\sqrt{N}} \tag{4.8a}$$

$$\Delta D \approx \frac{\mathrm{std}(s)}{\sqrt{N}} \tag{4.8b}$$

$$\Delta R \approx \frac{\mathrm{std}(\mathbf{w})}{\sqrt{N}} \tag{4.8c}$$

The standard deviations here are calculated by Equations 3.23 and 3.24. The source depth dependence of the standard deviations is shown in Figure 4.2. Thus these tables also summarise our computations of the expected bias, and therefore, the network effect in GC motion (ΔT for translation, ΔD for scale, ΔR for rotation), for various fault geometry and fault depth for an Earth modelled by the PREM.

The infinite sum on the spherical harmonic degree n was truncated, following Fred Pollitz's `STATIC1D` notes, when the source was deeper than 2.5 wavelengths, where the wavelength associated with a spherical harmonic is given by Equation 2.13. We found that to achieve sub-mm level accuracy this is indeed the minimum required cutoff. For a source depth of 5 km, for instance, the cutoff n is as high as ∼20000.

Note that the units for the standard deviations in the tables are 10^3 times larger than that of the means. This is because although the shape of the Earth is distorted significantly by the earthquakes, the displacement fields corresponding to the mean translation, rotation, or expansion of the surface are small in comparison. On the practical side, this means that even for a network consisting of over 10000 sites ($\sqrt{N} \approx 100$), the network effect is roughly an order of magnitude larger than the signal to detect.

4.1.3 Numerically constructed sampling distribution

Next, we evaluated the fields on a 1200×2400 uniform grid covering the Earth surface. The PDFs of $\mathbf{u}$, s, and $\mathbf{w}$ were then constructed as normalised frequency distributions by sorting each of their Cartesian components into 10000 equal width bins. The sampling distributions of the sample means, $p_{\mathbf{T}_{\mathrm{CN}}}$, $p_{D_{\mathrm{CN}}}$, and $p_{\mathbf{R}_{\mathrm{CN}}}$, were then calculated for different network sizes, using repeated convolution of the PDFs, as described in Section 3.4. The means calculated from the PDFs of $\mathbf{u}$, s, and $\mathbf{w}$

agreed with their theoretical values to within ∼0.1 mm, ∼0.001 ppb, and ∼10 μas respectively. We interpret these values to be indicative of the accuracy of our numerical results.

Figure 4.2 also shows a comparison of the analytical and the numerical methods of calculating the standard deviations of the fields **u** and **w** as functions of the seismic source depth. In general, the agreement improves as the depth of the seismic source is increased. This is because the fixed grid fails to adequately sample the distortions of the shape of the surface near the epicentre when the source is close to the surface. For other point sources not shown in the figure, the agreement between the two methods are also qualitatively similar.

We note here that initially we experimented with computationally inexpensive grid sizes of about 250×500 and cutoffs at spherical harmonic degree $n \approx 2500$ that also coincidentally gave us satisfactory accuracy for the CF parameters. However, as we increased the n cutoff to achieve convergence and to produce the short-wavelength features of the displacement field, the numerical accuracy of the CF parameters as compared to the theoretical values rapidly deteriorated. We found that this was because the localisation of the deformation field in the near field increased with higher cutoffs for the infinite summation and, therefore, the sampling of the near field by the fixed grid was insufficient. The accuracy of the numerical method was therefore recovered by increasing the spatial resolution of the grid.

Although using a finer grid would further improve the agreement between the analytical and the numerical results, we expect the gain to be mild compared to the additional computational effort it would require.

4.1.4 Comparison with the transformation method

In order to quantify the network effect for a random network of size N, we performed a Monte Carlo integration over possible network configurations to construct the probability distributions of the CN parameters calculated by the transformation method. The station positions were chosen at random with uniform probability over the surface of the Earth, that is, with a probability measure proportional to the area measure, or the angle measure, $d\Omega = \sin\theta\, d\theta\, d\phi$.

In order to improve the performance of our algorithm, we utilised the previ-

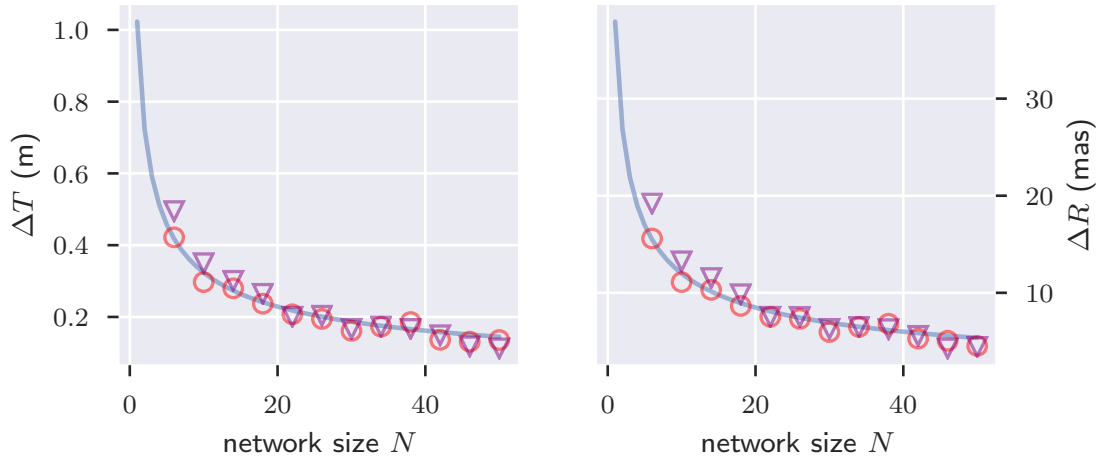

Figure 4.3: Comparison between the expected bias computed by the summation method (circles) and the transformation method (triangles) obtained by Monte Carlo simulation. The curves show the predictions of the probability density convolution method. The source is $M_{\text{dc-1}}$ at a depth of 10 km.

ously evaluated uniform grid samples to construct interpolation functions for the displacement field components in order to evaluate the fields at arbitrary locations. However, since the displacement field varies rapidly in the near field, we avoided interpolating inside a spherical cap of a radius of 1° around the epicentre. Our simulations ran until the calculated values of $\mathbf{T}_{\text{CF}}$, D_{CF}, and $\mathbf{R}_{\text{CF}}$ converged to within 0.005 mm, 0.0005 ppb, and 0.5 μas of their theoretical values, respectively.

The resulting network effect generally agrees (within ∼5%) with the summation method (Figure 4.3).

4.2 Sumatra–Andaman and Tōhoku–Oki earthquakes

We may imagine having two different, and perhaps opposite, objectives in mind when investigating the shifts in the CN parameters of a geodetic network due to some crustal deformation process. On one hand, we may be interested in measuring the resulting GC motion itself, and on the other hand, in the case of selecting the

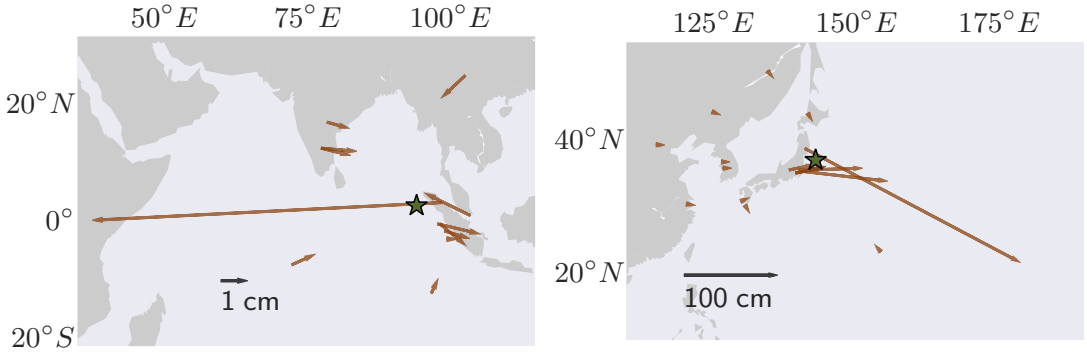

Figure 4.4: The horizontal coseismic offsets from GLOBK analysis of station position timeseries from *Bock and Webb* [2012, SOPAC archive]. The epicentres of the earthquakes (SA to the left and TO to the right) are marked by stars.

sites for the realisation of a reference frame, we may want to assess the perturbation induced by the deformation.

Here we investigate the coseismic deformation of the Earth surface by the Sumatra–Andaman (SA) earthquake of December 26, 2004, and the Tōhoku–Oki (TO) earthquake of March 11, 2011. To obtain simple theoretical descriptions of their deformation fields, we used centroid moment tensor products from the Global CMT Project (GCMT),[1] a searchable online catalog of earthquakes from the Lamont-Doherty Earth Observatory [*Dziewonski et al.*, 1981; *Ekström et al.*, 2012]. Thus, we essentially model them as resulting from point sources, of moment magnitude M_W 9.0 and M_W 9.1 at source depths 28.6 km and 20.0 km respectively.

To compare our predicted expected bias with the magnitude of the network effect, we use the space geodetic observation of station position timeseries from the Scripps Orbit and Permanent Array Center (SOPAC) archive[2]. The coseismic offsets in this timeseries for the two earthquakes (Figure 4.4) were calculated by the MEaSUREs program [*Bock and Webb*, 2012] using the GLOBK [*Herring et al.*, 2002] package. We will refer to the network of stations for which this timeseries data is available as the 'SOPAC network' for brevity. It is a large global network of ∼1000 sites (Figure 4.5) suitable for space geodetic detection of the GC motion.

[1] http://www.globalcmt.org
[2] available from ftp://sopac-ftp.ucsd.edu/pub/timeseries/measures/ats/Global/

As examples of relatively smaller networks, we also calculate the NE for the ITRF2008 and ITRF2014 core site networks[3], where we are interested in the perturbation caused by the earthquakes. The International Terrestrial Reference Frame (ITRF) core sites are carefully chosen to have mostly linear trajectories in order to accurately estimate Helmert parameters of transformation between successive ITRF versions. The core site networks (Figure 4.5) comprise of sites from different techniques as well as multi-technique sites: for ITRF2008 the network we used had 138 sites (of which 124 sites had GPS, 29 had VLBI, 13 had SLR, and 13 had DORIS sensors), whereas for ITRF2014 the core site network had 125 sites (of which 93 had GPS, 24 had VLBI, 8 had SLR, and 2 had DORIS sensors).

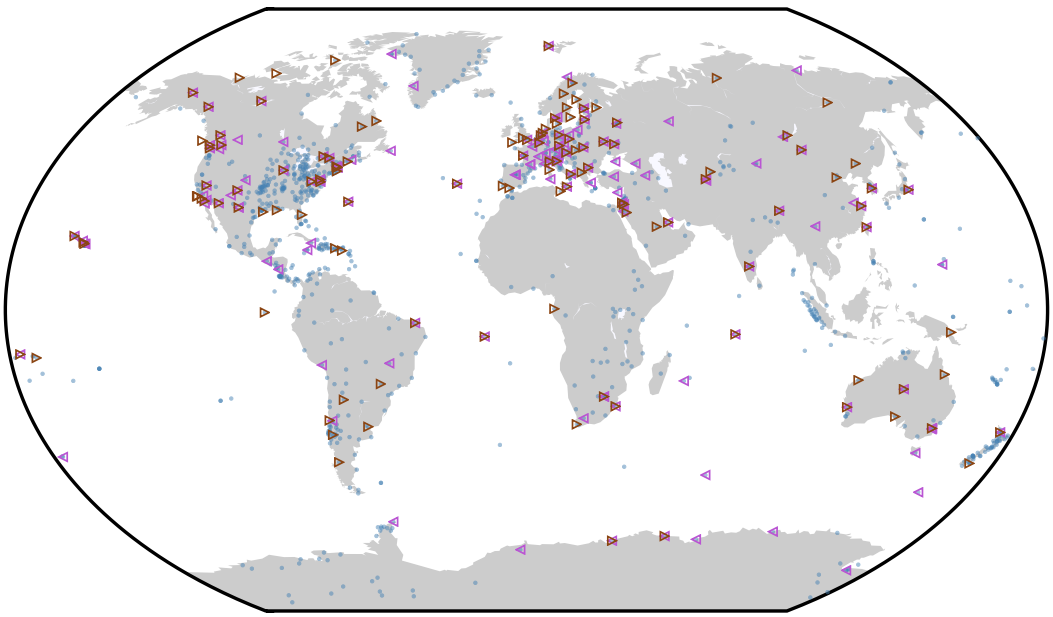

Figure 4.5: The stations consisting the three networks considered in this chapter and in Chapter 5. The ITRF2008 core site network is in purple, the ITRF2014 core site network in brown, and the 'SOPAC network' in blue.

The magnitudes of the theoretical shifts in the CF parameters due to the GCMT sources for the two earthquakes were 1.13 mm (SA) and 2.30 mm (TO) for transla-

[3] http://itrf.ign.fr

tion, and 53.4 μas (SA) and 108.4 μas (TO) for rotation. Instead of using a simple point source, *Sun and Dong* [2014] and *Zhou et al.* [2016] considered finite fault slip models and found the shifts to depend significantly on the slip model used, producing values 1.01–4.13 mm (SA) and 1.63–2.28 mm (TO) for translation (as reported in the correction article *Zhou et al.* [2015]), and 47.0–200.0 μas (SA) and 76.3–108.1 μas (TO) for rotation. On the other hand, we found that the expected bias, which is the main focus of our study here, is not sensitive to the fault model and therefore point sources suffice for our purposes.

4.3 Results for the SOPAC network

We report the results of our simulations in Table 4.5 for the Sumatra–Andaman (SA) event and Table 4.6 for the Tōhoku–Oki (TO) event. The CN shifts for the networks considered here are calculated using the transformation method so as to follow the ITRF realisation procedure, and the results obtained by the summation method are omitted for the sake of brevity. The differences between the two methods, incidentally, are less than 5% for the ITRF networks, but reach up to 40% for the SOPAC network for which sampling the near field introduces large displacements in a small number of sites.

In our simulations, the much larger SOPAC network detected signals comparable in magnitude to the theoretical shifts (compare the columns of the rows $|\mathbf{T}|$ and $|\mathbf{R}|$). However, the deviations from the theoretical predictions (rows $|\mathbf{T}-\mathbf{T}_{\mathrm{CF}}|$ and $|\mathbf{R}-\mathbf{R}_{\mathrm{CF}}|$) were also comparable in magnitude, validating our anticipation of the network effect being a primary hindrance to the measurement of GC motion. When comparing with satellite observations (Figure 4.4), it is found that for the SA event the signal was weaker than the simulated shift, whereas for the TO event they were stronger. In both cases, the deviations from the theoretical shifts were well within the expected bias predicted by our analysis for both the simulated and the observed coseismic offsets and, as such, may be interpreted to have had significant contributions from the unevenness in the coverage of the near field by the SOPAC network.

	GCMT theoretical	SOPAC simulation	SOPAC observations
(mm)	$\mathbf{T}_{CF}$	$\mathbf{T}_{CN}$	$\mathbf{T}_{CN}$
T_x	0.67	3.27	0.14
T_y	0.33	0.23	0.04
T_z	−0.85	−1.05	−0.03
$\lvert\mathbf{T}\rvert$	1.13	3.44	0.15
$\lvert\mathbf{T}-\mathbf{T}_{CF}\rvert$		2.59	1.02
ΔT		8.09	8.09
(ppb)	D_{CF}	D_{CN}	D_{CN}
D	0.01	−0.03	0.00
$\lvert D-D_{CF}\rvert$		0.04	0.01
ΔD		0.62	0.62
(μas)	$\mathbf{R}_{CF}$	$\mathbf{R}_{CN}$	$\mathbf{R}_{CN}$
R_x	−41.6	−56.2	−1.7
R_y	−1.3	−30.4	−1.0
R_z	−33.4	−147.9	−6.5
$\lvert\mathbf{R}\rvert$	53.4	161.1	6.8
$\lvert\mathbf{R}-\mathbf{R}_{CF}\rvert$		119.0	48.2
ΔR		295.6	295.6

Table 4.5: Shifts in instantaneous CN parameters for the 2004 Sumatra–Andaman (SA) event for the SOPAC network. The 'observations' column shows the coseismic offsets derived from the GPS timeseries data from *Bock and Webb* [2012].

4.4 Results for the ITRF core networks

The criteria for the ITRF core network sites are that these sites have been continuously monitored for at least 3 years, that they are located on the rigid parts of the tectonic plates and are far away from the deforming zones, and that the velocity formal errors and the velocity residuals are all less than 3 mm/yr, for at least three different solutions [*Altamimi et al.*, 2002]. However, if not properly accounted for, the coseismic displacement field of a great earthquake can introduce significant position and velocity errors in the realisation of a terrestrial reference frame (RF) [*Tregoning et al.*, 2013]. Because of their relatively small size, the ITRF core site networks are therefore especially vulnerable to perturbation by the coseismic field of great earthquakes that violate the assumption of linearity of their motion.

	GCMT theoretical	SOPAC simulation	SOPAC observations
(mm)	$\mathbf{T}_{CF}$	$\mathbf{T}_{CN}$	$\mathbf{T}_{CN}$
T_x	−1.98	−2.06	−3.68
T_y	−1.05	−1.53	−4.13
T_z	−0.47	−0.25	−1.26
$\lvert\mathbf{T}\rvert$	2.29	2.58	5.67
$\lvert\mathbf{T}-\mathbf{T}_{CF}\rvert$		0.53	3.60
ΔT		22.61	22.61
(ppb)	D_{CF}	D_{CN}	D_{CN}
D	0.03	0.03	−0.10
$\lvert D-D_{CF}\rvert$		0.00	0.12
ΔD		1.77	1.77
(μas)	$\mathbf{R}_{CF}$	$\mathbf{R}_{CN}$	$\mathbf{R}_{CN}$
R_x	20.3	29.7	47.3
R_y	−72.5	−53.0	−136.1
R_z	77.9	129.8	279.0
$\lvert\mathbf{R}\rvert$	108.4	143.3	314.0
$\lvert\mathbf{R}-\mathbf{R}_{CF}\rvert$		56.3	212.6
ΔR		831.6	831.6

Table 4.6: Shifts in instantaneous CN parameters for the 2011 Tōhoku–Oki (TO) event for the SOPAC network. The data presented here are the counterparts of Table 4.5 for the TO event.

For the SA event (Table 4.7), the shifts measured by the ITRF core sites in our simulations were an order of magnitude smaller than the theoretical shifts (compare the columns of the rows $|\mathbf{T}|$ and $|\mathbf{R}|$, values to the left of the slash). This is not surprising, given that the closest core site of the ITRF network, situated in Bangalore, India, is over 19.3° (∼2000 km) from the rupture zone, meaning that no sites sensed the near field deformation. However, for the TO event (Table 4.8), the theoretical and the simulated shifts were comparable. The shifts detected by the ITRF core network for the latter event can be ascribed mostly to the contributions of the Very-Long-Baseline Interferometry (VLBI) station situated in Kashima, Japan, being separated from the epicentre by only 2.5°.

In both cases, the expected biases from sampling the whole of the Earth's surface (reported quantities to the left of the slashes in Tables 4.7 and 4.8, rows

	GCMT theoretical	ITRF2008 simulation	ITRF2014 simulation
(mm)	$\mathbf{T}_{\mathrm{CF}}$	$\mathbf{T}_{\mathrm{CN}}$	$\mathbf{T}_{\mathrm{CN}}$
T_x	0.67/−0.01	0.03	0.02
T_y	0.33/ 0.15	0.10	0.10
T_z	−0.85/ 0.00	−0.01	0.01
$\lvert\mathbf{T}\rvert$	1.13/ 0.15	0.10	0.10
$\lvert\mathbf{T}-\mathbf{T}_{\mathrm{CF}}\rvert$		1.08/0.06	1.10/0.06
ΔT		22.13/0.09	23.26/0.10
(ppb)	D_{CF}	D_{CN}	D_{CN}
D	0.01/0.00	0.01	0.01
$\lvert D-D_{\mathrm{CF}}\rvert$		0.00/0.01	0.00/0.00
ΔD		1.69/0.00	1.78/0.00
(μas)	$\mathbf{R}_{\mathrm{CF}}$	$\mathbf{R}_{\mathrm{CN}}$	$\mathbf{R}_{\mathrm{CN}}$
R_x	−41.6/−0.2	−0.1	0.6
R_y	−1.3/ 0.0	−0.6	−0.5
R_z	−33.4/−0.2	−2.9	−2.2
$\lvert\mathbf{R}\rvert$	53.4/ 0.2	2.9	2.4
$\lvert\mathbf{R}-\mathbf{R}_{\mathrm{CF}}\rvert$		51.6/2.8	52.5/2.3
ΔR		809.2/4.4	850.2/4.6

Table 4.7: Shifts in instantaneous CN parameters for the 2004 Sumatra–Andaman (SA) event for the ITRF core networks. Where there are two values separated by a slash, the ones on the left are for the full field, while the ones on the right are for fields with a spherical cap excluded with the exclusion angle $\theta_{\mathrm{ex}} = 9.7^\circ$, that is, half the distance to the nearest site at Bangalore, India.

ΔT, ΔD, and ΔR) vastly overestimate the discrepancies between the simulated and the theoretical shifts for the ITRF core networks. This is because the ITRF core networks are far from random in that their stations have been selectively chosen to minimise non-linear signals and, since the coseismic displacement field is localised in nature, the sites therefore are, in effect, sampling only from the far field.

	GCMT theoretical	ITRF2008 simulation	ITRF2014 simulation
(mm)	$\mathbf{T}_{\mathrm{CF}}$	$\mathbf{T}_{\mathrm{CN}}$	$\mathbf{T}_{\mathrm{CN}}$
T_x	−1.98/−0.36	−1.00	−1.43
T_y	−1.05/−0.01	−1.90	−2.09
T_z	−0.47/ 0.09	0.46	0.57
$\lvert\mathbf{T}\rvert$	2.29/ 0.37	2.20	2.60
$\lvert\mathbf{T}-\mathbf{T}_{\mathrm{CF}}\rvert$		1.59/2.03	1.56/2.39
ΔT		61.89/2.03	65.03/2.14
(ppb)	D_{CF}	D_{CN}	D_{CN}
D	0.03/0.00	−0.02	−0.04
$\lvert D-D_{\mathrm{CF}}\rvert$		0.05/0.02	0.07/0.04
ΔD		4.83/0.03	5.08/0.03
(μas)	$\mathbf{R}_{\mathrm{CF}}$	$\mathbf{R}_{\mathrm{CN}}$	$\mathbf{R}_{\mathrm{CN}}$
R_x	20.3/ 2.2	42.9	41.5
R_y	−72.5/−7.7	−6.6	−2.5
R_z	77.9/ 8.3	130.2	143.1
$\lvert\mathbf{R}\rvert$	108.4/ 11.5	137.3	149.0
$\lvert\mathbf{R}-\mathbf{R}_{\mathrm{CF}}\rvert$		87.2/128.6	98.0/140.5
ΔR		2276.2/ 98.2	2391.6/103.2

Table 4.8: Shifts in instantaneous CN parameters for the 2011 Tōhoku–Oki (TO) event for the ITRF core networks. The data presented here are the counterparts of Table 4.7 for the TO event with $\theta_{\mathrm{ex}} = 1.3°$, that is, half the distance to the nearest site at Kashima, Japan.

4.5 Exclusion of epicentral cap

As discussed in the previous section, the expected biases for a network of ∼100 sites are unrealistically large compared to the network effect that the ITRF core sites experience. This apparent failure of our estimate can be explained by noting that a random network typically samples points very close to the epicentre that introduce large fluctuations, whereas, in practice, the core site network is carefully selected to avoid any non-linear motion that could damage the stability of the reference frame.

We therefore investigate the effect of choosing a minimum threshold distance from the earthquake epicentre for the stations of the random network when calculating the expected bias (Figure 4.6). That is, no stations are allowed with an

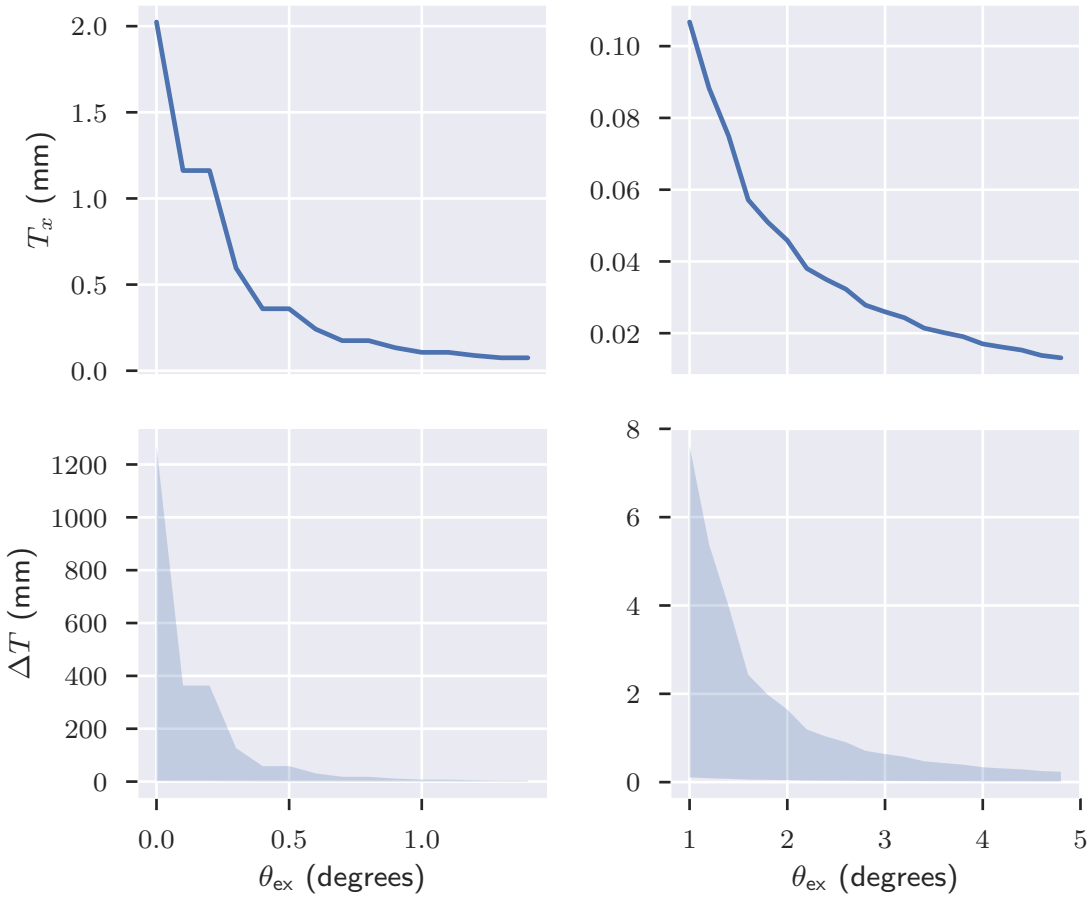

Figure 4.6: Effect of exclusion of an epicentral cap on the frequency distribution of the components of $\mathbf{T}_{CN}$ for $N = 1$. The seismic source is $M_{dc\text{-}1}$ at a depth of 10 km. Both the average shift (top, showing the only non-zero component T_x) and the associated expected bias (bottom) diminish rapidly with the exclusion angle.

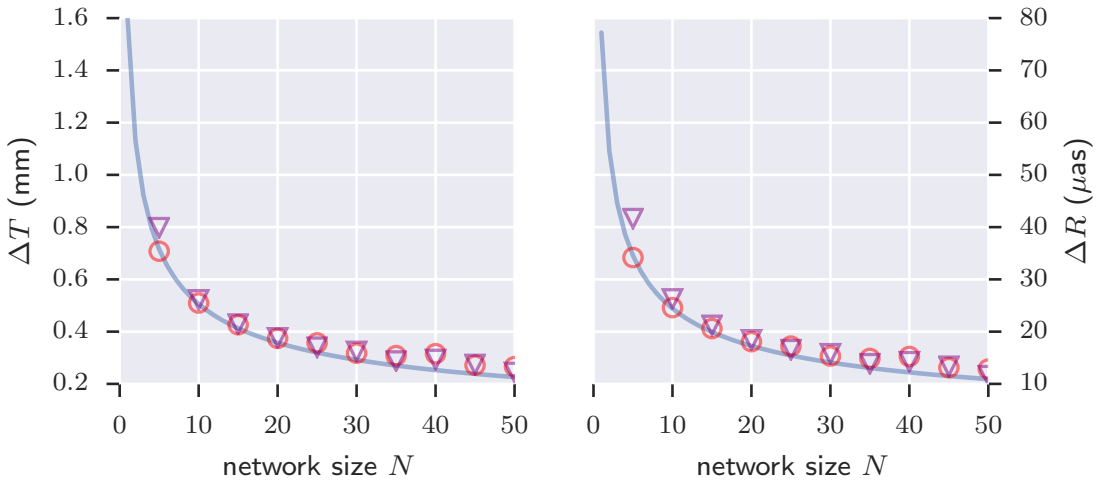

Figure 4.7: Comparison of the network effect computed by the summation method (circles) and the transformation method (triangles) obtained by Monte Carlo simulation when stations with distance less than 2° are excluded. The curves show the predictions of the probability density convolution method. The source is $M_{\text{dc-1}}$ at a depth of 10 km. Note that the units are 10^3 times smaller than those of Figure 4.3.

epicentral distance $\theta \leq \theta_{\text{ex}}$ where θ_{ex} is the specified threshold distance that we call the 'exclusion angle'. We find that most of the contributions to both the mean and the standard deviation of $\mathbf{u}$, as expected, comes from the near field. Thus, to achieve sub-mm level perturbations to the network, only a distance of ~2.5° around the epicentre needs to be excluded for M_W 9.0 earthquakes. However, excluding a spherical cap destroys the orthogonality property of the spherical harmonics and, therefore, analytic expressions for neither the shifts nor the network effect are readily available in this case. Therefore we obtained them numerically.

Incidentally, the difference between the summation method and the transformation method of obtaining the expected bias by Monte Carlo simulations diminishes (within ~1%) when an exclusion angle θ_{ex} of 2° around the epicentre is in effect (Figure 4.7), since the displacement field in the far field is generally smoother and much smaller in magnitude.

Coming back to the ITRF core sites, the expected bias becomes much more realistic when a spherical cap around the epicentre is excluded (reported quantities

to the right of the slashes in Tables 4.7 and 4.8). Our choice of the exclusion angle θ_{ex} was roughly half of the angular distance θ_{min} of the closest station from the epicentre for the two earthquakes. Also, the reported deviations of the CN parameters are not from the CF parameters for the full field, rather the deviations are from the CF parameters for fields with the epicentral cap excluded. This demonstrates that the network effect in the measurements by the ITRF core site networks is estimated well by modelling them to be measuring the movement of the CF of the far field only.

We note that in principle the choice of θ_{ex} is subjective. For the excluded cap not to discard the observations at any of the stations of the network, we must have

$$0 \leq \theta_{ex} \leq \theta_{min} \tag{4.9}$$

but otherwise we found that the computed expected bias is not sensitive to the exact choice θ_{ex} as long as the near field is effectively excluded. The simple choice of $\theta_{ex} = \frac{1}{2}\theta_{min}$ not only satisfies Equation 4.9 but also results in satisfactory estimates of the network effect in most cases.

On the other hand, since the SOPAC network is an example of a large network intended to have global coverage, we do not consider exclusion of epicentral caps in that case.

4.6 Results for the Centre of Network frame

Here we briefly report the effect (Table 4.9 for the SA event and Table 4.10 for the TO event) of modifying the CN parameter definitions to include Voronoi cell area weights for the stations as was proposed in Section 3.6. For these Centre of Weighted Network (CWN) frames, we find that the measurement of CF parameter shifts by the SOPAC network improves considerably (∼20–60%) for both of the events, and for both the summation and the transformation methods (compare rows $|\mathbf{T} - \mathbf{T}_{CF}|$, $|D - D_{CF}|$, and $|\mathbf{R} - \mathbf{R}_{CF}|$ of these two tables with the corresponding rows of the previous tables). Although the network effect largely remains the same in the small perturbations recorded by the ITRF core sites for the SA event resulting in ∼0–10% change in both directions, it in fact gets enhanced for the TO event (by ∼40–80%).

	GCMT theoretical	SOPAC simulation	SOPAC observations	ITRF2008 simulation	ITRF2014 simulation
(mm)	$\mathbf{T}_{\mathrm{CF}}$	$\mathbf{T}_{\mathrm{CWN}}$	$\mathbf{T}_{\mathrm{CWN}}$	$\mathbf{T}_{\mathrm{CWN}}$	$\mathbf{T}_{\mathrm{CWN}}$
T_x	0.67	1.79	0.02	−0.05	−0.08
T_y	0.33	0.29	0.12	0.15	0.13
T_z	−0.85	−0.67	0.07	−0.01	0.01
$\lvert\mathbf{T}\rvert$	1.13	1.93	0.14	0.16	0.15
$\lvert\mathbf{T}-\mathbf{T}_{\mathrm{CF}}\rvert$		1.13	1.14	1.12	1.16
ΔT		8.09	8.09	22.13	23.26
(ppb)	D_{CF}	D_{CWN}	D_{CWN}	D_{CWN}	D_{CWN}
D	0.01	−0.02	0.00	0.00	0.00
$\lvert D-D_{\mathrm{CF}}\rvert$		0.03	0.01	0.01	0.00
ΔD		0.62	0.62	1.69	1.78
(μas)	$\mathbf{R}_{\mathrm{CF}}$	$\mathbf{R}_{\mathrm{CWN}}$	$\mathbf{R}_{\mathrm{CWN}}$	$\mathbf{R}_{\mathrm{CWN}}$	$\mathbf{R}_{\mathrm{CWN}}$
R_x	−41.6	−33.3	2.6	−0.8	0.6
R_y	−1.3	2.1	0.8	−0.2	−0.2
R_z	−33.4	−88.1	−1.1	1.8	3.2
$\lvert\mathbf{R}\rvert$	53.4	94.2	2.9	1.9	3.2
$\lvert\mathbf{R}-\mathbf{R}_{\mathrm{CF}}\rvert$		55.4	54.8	53.9	55.9
ΔR		295.6	295.6	809.2	850.2

Table 4.9: Shifts in instantaneous CWN parameters for the 2004 Sumatra–Andaman (SA) event. The 'observations' column shows the coseismic offsets derived from the GPS timeseries data from *Bock and Webb* [2012].

Once again, this unexpected behaviour of the networks in this case may be ascribed to the inclusion of the site in Kashima, Japan. If we exclude this site from the network there are only mild changes in both directions, as in the SA event. It should be noted that the effects of the proximity of the Kashima station to the TO epicentre is here exacerbated by the absence of nearby core sites on its Pacific Ocean side, resulting in its Voronoi cell being exceptionally large.

	GCMT theoretical	SOPAC simulation	SOPAC observations	ITRF2008 simulation	ITRF2014 simulation
(mm)	$\mathbf{T}_{\mathrm{CF}}$	$\mathbf{T}_{\mathrm{CWN}}$	$\mathbf{T}_{\mathrm{CWN}}$	$\mathbf{T}_{\mathrm{CWN}}$	$\mathbf{T}_{\mathrm{CWN}}$
T_x	−1.98	−1.79	−3.70	−2.19	−2.71
T_y	−1.05	−0.82	−3.26	−4.53	−5.46
T_z	−0.47	−0.61	−1.95	0.75	0.88
$\lvert\mathbf{T}\rvert$	2.29	2.06	5.31	5.09	6.16
$\lvert\mathbf{T}-\mathbf{T}_{\mathrm{CF}}\rvert$		0.33	3.17	3.69	4.67
ΔT		22.61	22.61	61.89	65.03
(ppb)	D_{CF}	D_{CWN}	D_{CWN}	D_{CWN}	D_{CWN}
D	0.03	0.02	−0.08	−0.07	−0.09
$\lvert D-D_{\mathrm{CF}}\rvert$		0.01	0.11	0.10	0.12
ΔD		1.77	1.77	4.83	5.08
(μas)	$\mathbf{R}_{\mathrm{CF}}$	$\mathbf{R}_{\mathrm{CWN}}$	$\mathbf{R}_{\mathrm{CWN}}$	$\mathbf{R}_{\mathrm{CWN}}$	$\mathbf{R}_{\mathrm{CWN}}$
R_x	20.3	11.7	54.0	144.3	176.0
R_y	−72.5	−71.9	−171.3	−50.5	−60.4
R_z	77.9	67.3	187.5	206.5	240.3
$\lvert\mathbf{R}\rvert$	108.4	99.2	259.6	257.0	303.9
$\lvert\mathbf{R}-\mathbf{R}_{\mathrm{CF}}\rvert$		13.7	151.3	180.0	225.3
ΔR		831.6	831.6	2276.2	2391.6

Table 4.10: Shifts in instantaneous CWN parameters for the 2011 Tōhoku–Oki (TO) event. The data presented here are the counterparts of Table 4.9 for the TO event.

Chapter 5

Elastic deformation by hydrological loading

Here, we study the secular drift, due to the elastic deformation caused by the redistribution of surface water, in the derivative parameters, that is, the time-derivatives of the instantaneous Helmert parameters (HPs) of coordinate transformation: the velocity $\dot{\mathbf{T}}_{\mathrm{CF}}$, the rate of scale change $\dot{D}_{\mathrm{CF}}$, and the angular velocity $\dot{\mathbf{R}}_{\mathrm{CF}}$. Our 'theoretical' model of the time-dependent surface water density is derived from the observations of the gravity field by the Gravity Recovery and Climate Experiment (GRACE) [*Tapley et al.*, 2004] satellites. The timeseries that we consider, the Release-05 (RL05) GRACE Satellite-only Model (GSM) data products from the Center of Space Research (CSR) at the University of Texas at Austin, is given (except for some missing data points) at 30-day intervals for the period 2004–2014. The time interval was chosen to span a whole decade in order to minimise the error introduced by seasonal signals and short timeseries spans [*Santamaría-Gómez and Mémin*, 2015] in the secular velocity estimates. The spherical harmonics coefficient timeseries of the "space potential" field[1] is hosted online through the Physical Oceanography Distributed Active Archive Center (PODAAC) at the Jet Propulsion Laboratory (JPL). Various gravitational variations have already been taken into account in the processing of the data, such as Earth tides, ocean tides, atmospheric pressure fields and barotropic ocean response. Thus the time varying field that we have used only includes hydrology, snow cover, baroclinic ocean signals and glacial isostatic

[1] available from `ftp://podaac.jpl.nasa.gov/allData/grace/L2/CSR/RL05/`

adjustments (GIA), and possibly other unmodelled effects which we expect to be small.

These data products are for degrees $n \geq 2$ only, as the GRACE satellites alone are incapable of observing the geocentre (GC) motion. Therefore, we use the degree-1 coefficient timeseries[2] from *Swenson et al.* [2008], obtained by combining the RL05 data with the output of two numerical ocean models: one from the Estimating the Circulation and Climate of the Ocean (ECCO) consortium and the other being the Ocean Model for Circulation and Tides (OMCT) used by the GRACE project. For brevity, we will refer to this timeseries simply as the 'Ocean Model' (OM) degree-1 data. As discussed in Section 2.7.2, we need to transform the surface displacements due to the degree-1 potential field provided in the Centre of Figure (CF) frame to the inertial Centre of Mass (CM) frame that we choose to work in. Note that there is no degree-0 field in this case because of the conservation of total surface water mass.

Lastly, to facilitate the convergence of our Monte Carlo simulations, we subtract the static field according to the GRACE Gravity Model 03 (GGM03)[3] [*Tapley et al.*, 2007] from the RL05 potential field to obtain the time varying gravity anomaly field due to hydrological loading. Using the Love number theory presented in Section 2.7, we then calculated the elastic deformation due to surface loading by the water mass derived from this timeseries. We use here the Love numbers[4] obtained by Pascal Gégout for the Preliminary Reference Earth Model (PREM).

5.1 Geocentre motion from GRACE and ocean models

The time-dependent geocentre motion obtained by *Swenson et al.* [2008] is shown in Figure 5.1 for the period 2004–2014.

As in Section 4.1.4, we then evaluate the means and the standard deviations of the sampling distributions by Monte Carlo simulations over all possible network configurations of sample size N, and interpret them to represent the changes in

[2] available at `ftp://podaac.jpl.nasa.gov/allData/tellus/L2/degree_1/`
[3] available from `http://www.csr.utexas.edu/grace/gravity/`
[4] available from `https://gemini.gsfc.nasa.gov/aplo/Load_Love2_CM.dat`

Figure 5.1: Geocentre motion caused by hydrological loading deformations for the period 2004–2014. The green curve shows the quasi-periodic instantaneous position of the CF with respect to the CM frame. The blue line is our estimate of the secular motion of the geocentre.

the CF parameters and the associated expected biases respectively. The numerical values for the secular derivative parameters obtained this way were:

$$\dot{\mathbf{T}}_{\mathrm{CF}} = \langle \dot{\mathbf{T}}_{\mathrm{CN}} \rangle \approx (0.12\,\hat{\mathbf{x}} + 0.00\,\hat{\mathbf{y}} + 0.32\,\hat{\mathbf{z}})\,\mathrm{mm/yr} \tag{5.1a}$$

$$\dot{D}_{\mathrm{CF}} = \langle \dot{D}_{\mathrm{CN}} \rangle \approx 0.00\,\mathrm{ppb/yr} \tag{5.1b}$$

$$\dot{\mathbf{R}}_{\mathrm{CF}} = \langle \dot{\mathbf{R}}_{\mathrm{CN}} \rangle \approx (0.0\,\hat{\mathbf{x}} + 0.0\,\hat{\mathbf{y}} + 0.0\,\hat{\mathbf{z}})\,\mu\mathrm{as/yr} \tag{5.1c}$$

within the shown precision for both the summation and the transformation methods. Note that the angular velocity is expected to vanish because the toroidal modes are absent in the loading problem, and the rate of scale change also vanishes because the mass of the water layer is conserved. Within this precision, the same values are obtained if the linear regression procedure of Section 3.5.2 is applied to the theoretical GC motion derived from the OM data directly. Although the GRACE data we used contains contributions from the GIA, its effect on the GC motion that these parameters correspond to is small [*Swenson et al.*, 2008].

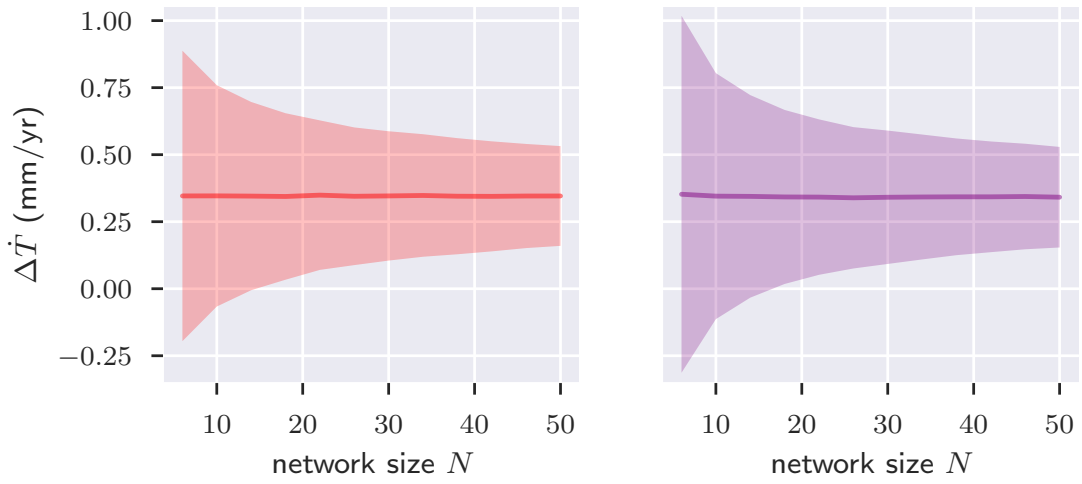

Figure 5.2: The network effect in secular velocity due to surface water mass movement also scales as $1/\sqrt{N}$ where N is the network size. For both the summation method (left, in pink) and the transformation method (right, in purple), the magnitude of the velocity parameter $|\dot{\mathbf{T}}_{\mathrm{CF}}| \approx 0.34\,\mathrm{mm/yr}$ from Equation 5.1 is marked by a thick horizontal line. The shaded region enveloping the line shows the uncertainty in the determination of the velocity parameter as predicted by the expected bias calculated for different network sizes.

It may be seen from Figure 5.2 that the expected biases, as in the case of instantaneous parameters for the coseismic deformation field in Chapter 4, show the expected $1/\sqrt{N}$ scaling for the derivative parameters too. According to the summation method they were:

$$\Delta\dot{T} = \mathrm{std}(\dot{\mathbf{T}}_{\mathrm{CN}}) \approx \frac{1.32\,\mathrm{mm/yr}}{\sqrt{N}} \tag{5.2a}$$

$$\Delta\dot{D} = \mathrm{std}(\dot{D}_{\mathrm{CN}}) \approx \frac{0.21\,\mathrm{ppb/yr}}{\sqrt{N}} \tag{5.2b}$$

$$\Delta\dot{R} = \mathrm{std}(\dot{\mathbf{R}}_{\mathrm{CN}}) \approx \frac{17.1\,\mu\mathrm{as/yr}}{\sqrt{N}} \tag{5.2c}$$

For the transformation method, the values were in general ∼10–15% higher for small network sizes but agreed better with the results of the summation method as the network size N increased.

Although the ratios of the expected biases to the parameters themselves are, in general, smaller in the hydrological loading deformation case compared to coseismic deformation, they are still not negligible. For example, for a realistic network size of $N \approx 400$, the expected network effect (NE) in the velocity parameters is ∼0.07 mm/yr, that is, ∼20% of the magnitude of the parameters itself. Surprisingly, although the theoretical rotation parameters should be zero, in practice the network effect in the rotation parameters is comparable in magnitude to that in the translation parameters when converted into corresponding motion of the pole. Thus the sub-sampling of the displacement field introduces a small spurious angular velocity that, fortunately, is well below the current detection capabilities of the geodetic techniques.

5.2 Results for the SOPAC network

Table 5.1 shows the summary of our results for the SOPAC network for the Centre of Network (CN) and the Centre of Weighted Network (CWN) frames. The theoretical column shows the values in Equation 5.1 derived from the Ocean Model (OM) degree-1 data, whereas the simulation columns show the drifts in the

	OM theoretical	SOPAC simulation	SOPAC simulation
(mm/yr)	$\dot{\mathbf{T}}_{CF}$	$\dot{\mathbf{T}}_{CN}$	$\dot{\mathbf{T}}_{CWN}$
$\dot{T}_x$	0.12	0.18	0.09
$\dot{T}_y$	0.00	−0.09	0.06
$\dot{T}_z$	0.32	0.45	0.36
$\lvert\dot{\mathbf{T}}-\dot{\mathbf{T}}_{CF}\rvert$		0.17	0.08
$\Delta\dot{T}$		0.04	0.04
(ppb/yr)	$\dot{D}_{CF}$	$\dot{D}_{CN}$	$\dot{D}_{CWN}$
$\dot{D}$	0	0.05	0.00
$\lvert\dot{D}-\dot{D}_{CF}\rvert$		0.05	0.00
$\Delta\dot{D}$		0.01	0.01
(μas/yr)	$\dot{\mathbf{R}}_{CF}$	$\dot{\mathbf{R}}_{CN}$	$\dot{\mathbf{R}}_{CWN}$
$\dot{R}_x$	0	−2.91	0.25
$\dot{R}_y$	0	0.18	−0.91
$\dot{R}_z$	0	0.62	−0.37
$\lvert\dot{\mathbf{R}}-\dot{\mathbf{R}}_{CF}\rvert$		3.00	1.01
$\Delta\dot{R}$		0.50	0.50

Table 5.1: Shifts in the derivative CN and CWN parameters for the SOPAC network.

parameters observed by the SOPAC network in our simulations. The deviations of the observed values by the networks from the theoretical values are also shown, along with the expected bias calculated by Equation 5.2.

Our estimates are within an order of magnitude of the observed deviations in all cases. It should be noted, however, that beyond an illustration of the applicability of our procedure, the rotation and the angular velocity results are of little interest because of their negligible magnitudes, as the current measurement precision for Earth's rotation and rotation rate are at 1 mas and 0.1 mas/yr level respectively [*Chao et al.*, 2014]. Our velocity results may be compared to *Wu et al.* [2012] where the secular trend was calculated using several different methods resulting in estimates that vary considerably. Among them, our procedure is closest to that of *Swenson et al.* [2008] who found a secular velocity estimate of $\dot{\mathbf{T}}_{CF} = (-0.06\,\hat{\mathbf{x}} - 0.04\,\hat{\mathbf{y}} + 0.06\,\hat{\mathbf{z}})$ mm/yr using the OM coefficients for the ECCO model. The significant difference in the estimate principally comes from the high sensitivity of the secular velocity parameters on the choice of time period. Our estimate agrees

with theirs for their choice of the time period (2003–2007).

For the CWN frame, it can be seen that there was an overall reduction (in most cases ∼50%) in the deviation from the CF parameters compared to the CN frame, that is, the estimation of the CF parameters from the observations of a geodetic network is significantly improved by using the CWN method.

However, our simulations have shown that there is no statistical advantage of choosing the CWN frame over the CN frame, that is, there is no significant reduction in the expected biases when integrating over all possible network configurations. This seemingly paradoxical result may be understood by noting that, although for smooth fields and some network configurations the field sampled at the station is representative of its corresponding region, there are also other networks where a disproportionately large area is represented by some point where the field has a significant deviation from its surroundings. Therefore, the results here as well as the results in the next section show that real geodetic networks such as the SOPAC network and the ITRF core networks are all well-behaved with respect to the hydrological loading deformations.

5.3 Results for the ITRF core networks

Table 5.2 summarises our results for the CN frame and the CWN frame for the ITRF core networks. It can be seen here that the expected bias estimates the NE for the networks well, despite their relatively small size. Unlike the coseismic displacement case, the elastic deformation field due to surface water movements is not localised and, therefore, the complications that we faced in Chapter 4 in that case do not arise here.

Again, the CWN frame in this case also performs better on an average than the CN frame in GC motion detection. From these observations, we expect the CWN frame to produce more realistic measurements of the shifts in CF frame parameters for real geodetic networks regardless of their size, as long as the displacement field of the geophysical process is not too irregular.

	OM theoretical	ITRF2008 simulation	ITRF2014 simulation	ITRF2008 simulation	ITRF2014 simulation
(mm/yr)	$\dot{\mathbf{T}}_{\mathrm{CF}}$	$\dot{\mathbf{T}}_{\mathrm{CN}}$	$\dot{\mathbf{T}}_{\mathrm{CN}}$	$\dot{\mathbf{T}}_{\mathrm{CWN}}$	$\dot{\mathbf{T}}_{\mathrm{CWN}}$
$\dot{T}_x$	0.12	0.24	0.24	0.20	0.15
$\dot{T}_y$	0.00	0.01	0.01	0.03	−0.01
$\dot{T}_z$	0.32	0.49	0.40	0.46	0.30
$\lvert\dot{\mathbf{T}}-\dot{\mathbf{T}}_{\mathrm{CF}}\rvert$		0.20	0.14	0.16	0.04
$\Delta\dot{T}$		0.11	0.12	0.11	0.12
(ppb/yr)	$\dot{D}_{\mathrm{CF}}$	$\dot{D}_{\mathrm{CN}}$	$\dot{D}_{\mathrm{CN}}$	$\dot{D}_{\mathrm{CWN}}$	$\dot{D}_{\mathrm{CWN}}$
$\dot{D}$	0	0.05	0.06	0.03	0.02
$\lvert\dot{D}-\dot{D}_{\mathrm{CF}}\rvert$		0.05	0.06	0.03	0.02
$\Delta\dot{D}$		0.02	0.02	0.02	0.02
(μas/yr)	$\dot{\mathbf{R}}_{\mathrm{CF}}$	$\dot{\mathbf{R}}_{\mathrm{CN}}$	$\dot{\mathbf{R}}_{\mathrm{CN}}$	$\dot{\mathbf{R}}_{\mathrm{CWN}}$	$\dot{\mathbf{R}}_{\mathrm{CWN}}$
$\dot{R}_x$	0	−1.1	−1.7	0.2	−1.7
$\dot{R}_y$	0	−0.5	−0.6	−0.3	−3.2
$\dot{R}_z$	0	0.0	0.3	−0.2	−0.1
$\lvert\dot{\mathbf{R}}-\dot{\mathbf{R}}_{\mathrm{CF}}\rvert$		1.2	1.8	2.1	3.6
$\Delta\dot{R}$		1.5	1.5	1.5	1.5

Table 5.2: Shifts in the derivative CN and CWN parameters for the ITRF core networks.

Chapter 6

Implementation

In this chapter, we document some highlights and some technical aspects of our implementation of the software needed to produce the results of this thesis. The source code for the programs developed for the project is available as a package called NERF[1] (for Non-linear Effects on Reference Frames).

For Chapter 4, our starting point was Fred Pollitz's `STATIC1D`[2] program to calculate coseismic displacements [see, for example *Pollitz*, 1996]. For Chapter 5, we adopted Paul Tregoning's routines to evaluate the elastic deformation due to the water mass movement inferred from GRACE measurements [see, for example, *Tregoning et al.*, 2009]. In both cases, our principle contribution was to enhance the programs to include exact calculations of the degree-1 fields. For the coseismic case we also added the degree-0 field, but in the hydrological loading case this field could be safely ignored because of the conservation of the total mass of the water envelope.

In addition, we developed the routines required for Monte Carlo integration over random geodetic network configurations. We also wrote algorithms to calculate Helmert parameters of transformation from the inertial frame to the reference frames realised by these networks by various methods discussed in Chapter 3. Among them, for the instantaneous case of the transformation method we took our initial inspirations from the `corcom` program in the GAMIT/GLOBK software suite [see, for example *Herring et al.*, 2008].

[1] hosted at `https://bitbucket.org/zannat/nerf`
[2] available from `https://earthquake.usgs.gov/research/software/`

We also implemented an algorithm to decompose the surface of a sphere into Voronoi cells around a set of specified points in order to experiment with our proposed alternate method of geocentre (GC) motion determination.

6.1 Overview of the project

Our choice of the implementation language was Python[3], despite the code we inherited being written in Fortran 77. Our motivation for this choice was the greater flexibility, readability, modularity, and re-usability of code that Python offers. We used Jupyter[4] notebooks for visualisation and interactive development. The execution of the algorithms, especially when running in batch, was orchestrated by Bash[5] shell scripts.

Besides the required mathematical and geometrical functions, we developed dedicated data types for the layered model of the Earth, vector spherical harmonic modes, and discrete displacement field at geodetic stations to be shared between both of the illustrative use cases. Moreover, this separation of concern facilitated testing and debugging of our code in isolation.

As expected for an interpreted language, the raw speed of our code was not on par with the original Fortran implementations. However, we utilised the popular NumPy[6] and SciPy[7] libraries to reduce the performance gap significantly. These well-tested packages also provided more confidence in the correctness of our programs.

Because of the so-called broadcasting rules for NumPy arrays, a majority of our developed functions were polymorphic in the shapes, or the ranks, of the arrays they were applied to. This feature offered syntactic clarity of the code by relieving the burden of manual book-keeping that otherwise obscures its mathematical content. For example, the same function

```
def angular_to_cartesian(theta, phi):
    """ Cartesian coordinates of a point on the unit sphere. """
    from numpy import array, sin, cos
    return array([sin(theta) * cos(phi), sin(theta) * sin(phi), cos(theta)])
```

[3] https://www.python.org
[4] https://www.jupyter.org/
[5] https://www.gnu.org/software/bash/
[6] https://www.numpy.org
[7] https://www.scipy.org

returns a 3-dimensional vector if its arguments `theta` and `phi` are numbers, whereas it returns a $3 \times N$ matrix if `theta` and `phi` are vectors of size N.

6.2 Numerical and performance considerations

Nevertheless, the main benefit of these choices turned out to be improvements in numerical accuracy. In order to be fast, `STATIC1D` relies heavily on interpolation of function values between pre-computed points. Consequently, it often fails to capture the highly oscillatory nature of the spherical harmonics, especially for higher degrees, resulting in apparent convergence to incorrect values for the displacement fields.

In his notes on `STATIC1D`, Fred Pollitz recommends, as a rule of thumb, summing up to the largest n that satisfies

$$d_s \leq 2.5\, \lambda_n \tag{6.1}$$

for satisfactory convergence of the sum, where d_s is the source depth, and the wavelength associated with the degree-n spherical harmonic is given by Equation 2.13,

$$\lambda_n = \frac{4\pi\, r_\oplus}{2n+1} \tag{6.2}$$

where $r_\oplus$ is the Earth radius. Our experiments also support this rule. With an average source depth of about 30 km, the 2004 Sumatra–Andaman coseismic field therefore requires summing up to $n \approx 3500$. Regrettably, previous studies often truncated the summation earlier, perhaps because of the considerable computational expense, which resulted in over-estimation of the far field and simultaneously under-estimation of the near field by substantial margins.

To further validate our calculations, we compared our predictions with the analytical half-space results of *Okada* [1985] for the near field where it is applicable (Figure 6.1). We found the agreement between the two to be substantially better than that with `STATIC1D`. As an additional check, we compared our results with analytical solutions for a non-stratified homogeneous Earth model [see, for example,

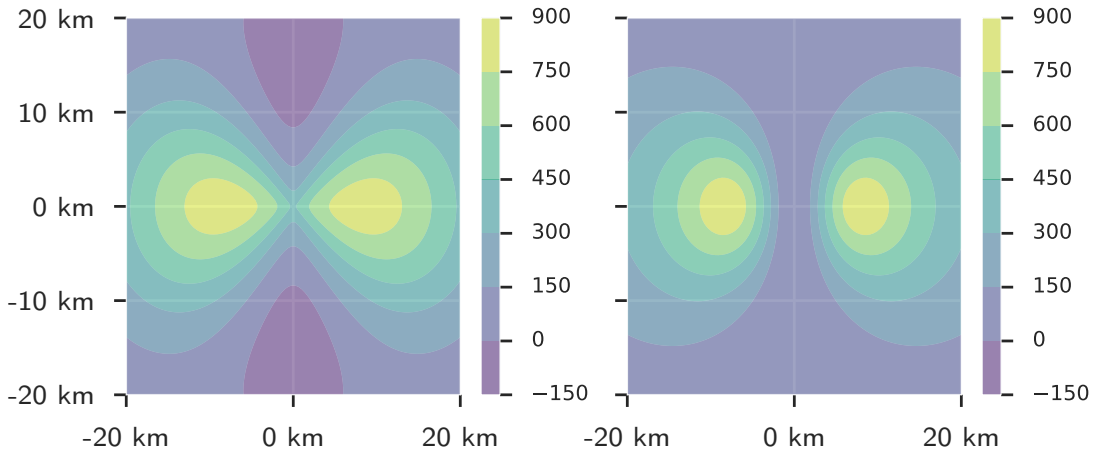

Figure 6.1: Comparison of our implementation of normal mode summation method (left) with the prediction of half-space theory (right) in the near field. The contour plots are showing the x-component of the displacement (in metres) in the epicentral Cartesian coordinate system. The seismic source is $M_{\text{dc-1}}$ of moment magnitude M_W 9.0 at 10 km depth from the surface. The infinite sum on the spherical harmonic degree was truncated at $n \approx 10000$. The difference between the predictions of the two methods is not significant for our purposes.

Takeuchi and Saito, 1972, §II.D] using Mathematica[8] and found it to be in satisfactory agreement even in the far field.

To our surprise, we found that, using Mathematica, we could invert the fundamental matrices discussed in Section 2.5.2 analytically, although we discovered later that they have appeared in the literature before [see, for example, *Sabadini and Vermeersen*, 2004]. Nevertheless, their use contributed to the numerical accuracy of the propagation of the solutions as well as to a moderate performance speed-up. Following `STATIC1D`, we also re-scaled the radial variables for the homogeneous solutions during the solution propagation so as to avoid numerical overflow or underflow for higher degrees, while taking care not to apply this re-scaling when propagating the solution associated with the discontinuity at the source.

[8] `https://www.wolfram.com/mathematica/`

6.3 Enhancements in functionality

In order to prevent the numerical overflow or underflow previously mentioned, `STATIC1D` requires breaking up a homogeneous layer into thinner layers with the same physical properties in the supplied Earth model file. However, this requires knowing in advance the maximum degree needed for the convergence of the summation which depends on the depth of the seismic source in consideration. We remedied this inconvenience by programming our algorithm to achieve the same effect by splitting the homogeneous layers dynamically as needed.

As discussed before, we implemented the calculation of degree-1 modes for both the coseismic displacement field and the elastic deformation due to hydrological loading field. We also added methods to calculate the changes to the Helmert parameters $\mathbf{T}_{\mathrm{CF}}$, D_{CF}, and $\mathbf{R}_{\mathrm{CF}}$ directly from the Earth model and the fault model. In doing so, we generalised the analytical formulae in *Sun and Dong* [2014] to stratified Earth models. We note that most standard programs to calculate coseismic displacement fields omit the degree-1 field [see, for example, *Xu and Chao*, 2015] since its effect on ground surveys is negligible.

Also, in our adaptation of the functionalities of the `corcom` program, we added the ability to calculate the Helmert parameters by several different methods: the summation method and the transformation method, for both the instantaneous and the time-varying case, with or without weights associated with the area represented by the stations. In addition, we included provisions for including any weight matrix coming from, for example, the covariance matrix of the displacement observations.

Finally, we note that our implementation could have benefited from the use of the recently developed `xarray`[9] library specifically designed for datasets with associated point position coordinates. We plan to incorporate this library in future developments of our code.

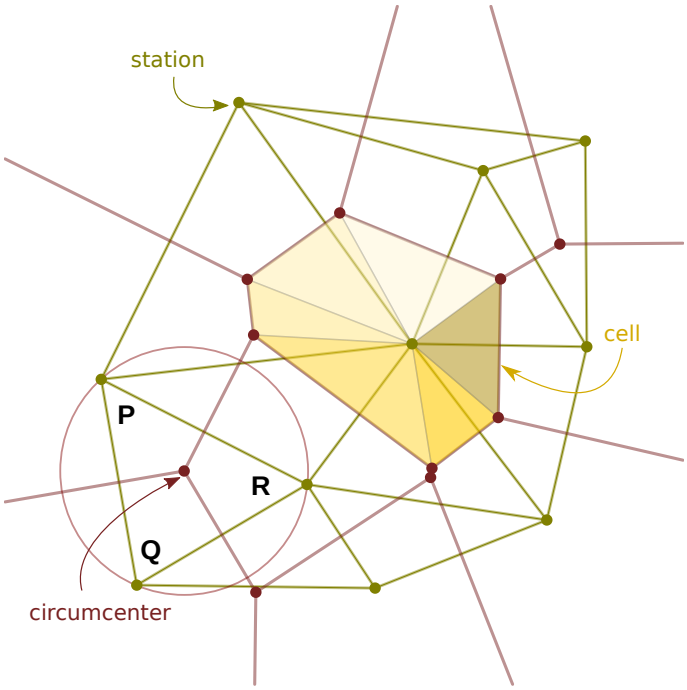

Figure 6.2: Duality between Delaunay triangulation and Voronoi decomposition, shown on the flat Euclidean plane for the ease of illustration. The Voronoi cell (red polygons) around a station (green dots) is constructed by sequentially joining the circumcentres (red dots) of the triangles (green triangles) that have the station as a common vertex, as depicted for the example (yellow fill) cell.

6.4 Voronoi decomposition of the surface of a sphere

In Section 3.6, we briefly introduced the decomposition of the surface of the Earth into Voronoi cells for the purposes of our proposed modification to the Centre of Network frame. Here we describe our conceptually simple algorithm for dividing the surface of a sphere, which in our case is the Earth, into Voronoi cells surrounding a specified set of points, which in our case are the ground stations. For simplicity, we here describe our algorithm for the unit sphere since the results for the spherical Earth may be obtained by scaling up the lengths by a factor of the Earth radius $r_\oplus$.

We use here a well-known relation, for the flat Euclidean plane, between Voronoi decomposition and Delaunay triangulation (Figure 6.2). The Delaunay

[9] https://xarray.pydata.org

triangulation [*Delaunay*, 1934] of the plane by a set of points is a triangulation such that no point in the set is contained inside the circumcircle of any of the triangles. The useful connection here is that the vertices of the Voronoi cells are the circumcentres of the Delaunay triangles. Therefore, we will be able to construct the Voronoi cells if we are given the Delaunay triangles.

Fortunately, the latter problem is simplified by the observation [*Brown*, 1979; *Renka*, 1997] that, for a sphere, finding the Delaunay triangulation is equivalent to the familiar problem of calculating the convex hull of the stations. Many efficient implementations of the convex hull problem are available, and we have used the SciPy bindings to the Qhull[10] library. The circumcentre of the spherical triangle with the stations **P**, **Q**, and **R** as its vertices may be found by calculating, for example, the vector $(\mathbf{P}-\mathbf{R})\times(\mathbf{Q}-\mathbf{R})$ perpendicular to the Euclidean triangle with the same vertices. If we now normalise this vector, then we find the point on the unit sphere that is the required circumcentre. The Voronoi cell of a station can then be constructed by sequentially joining the circumcentres of the triangles that touch the station by arcs of great circles on the sphere.

Once the spherical polygons are constructed, their areas are calculated by dividing them into spherical triangles whose areas are given by the classical L'Huilier's formula. For a spherical triangle with sides a, b, and c on the unit sphere, the classical L'Huilier's formula for the area A of the triangle states:

$$\tan\frac{1}{4}A=\sqrt{\tan\frac{1}{2}s\,\tan\frac{1}{2}(s-a)\,\tan\frac{1}{2}(s-b)\,\tan\frac{1}{2}(s-c)} \tag{6.3}$$

where $s=\frac{1}{2}(a+b+c)$, and the distances are measured in radians. The areas on the Earth surface are easily recovered by multiplying by $r_\oplus^2$.

Our algorithm unfortunately cannot resolve reliably stations with a few meters of each other due to numerical inaccuracies. This does not pose a serious problem to us since we did not distinguish between stations, often from different techniques, that are so close to each other. Incidentally, after we had finished collecting our data, a routine to calculate this decomposition had been introduced into the SciPy package making use of a more involved but numerically more stable algorithm due

[10] https://www.qhull.org

to *Caroli et al.* [2010]. We recommend using that library for this purpose in the future.

A related task here, for the investigations due to random network configurations, is choosing a point randomly on the surface of the sphere with a uniform probability density over the surface. The probability measure here is

$$\frac{d\Omega}{4\pi} = \frac{\sin\theta\, d\theta\, d\phi}{4\pi} = \frac{\sin\theta\, d\theta}{2}\,\frac{d\phi}{2\pi} \tag{6.4}$$

so that the coordinate ϕ is uniformly distributed over the interval $[0, 2\pi)$, but distribution of the coordinate θ is not uniform. The solution to this problem is to use the inverse sampling transform of the cumulative distribution function $z = \frac{1}{2}(1 - \cos\theta)$ to transform the uniform distribution of z over the unit interval into the required distribution for θ over the interval $[0, \pi)$.

Chapter 7

Conclusion

Accurate geocentre (GC) motion measurements are needed because interpretation of geophysical processes and realisation of terrestrial reference frames (TRFs) are strongly intertwined tasks. In this thesis, we found that measuring the GC motion by space geodetic techniques is severely constrained by the current number of geodetic ground stations and their uneven geographical distribution. Thus the error associated with the discrete sampling of the Earth surface, namely, the network effect (NE), presents a difficult obstacle towards achieving sub-millimetre level precision for TRFs.

We have proposed an intuitive and computationally inexpensive method to estimate the expected magnitude of the NE by stochastic analysis. Our estimate, which we call the expected bias, may be viewed as a formal error associated with discrete sampling in the GC motion predicted by a geophysical model of surface displacements.

Furthermore, we introduced a possible modification to the GC motion determination process by assigning weights proportional to the area of the Voronoi cell surrounding a station to the measurements of its displacement. We have shown that, for a reasonably smooth displacement field, the GC motion calculated by this process can be more accurate than the methods ordinarily employed. But we also notice that in rare instances this modification may in fact degrade GC motion detection.

Our findings here have been reported in the articles *Zannat and Tregoning* [2017a] and *Zannat and Tregoning* [2017b].

7.1 Summary of results

The most important result in this thesis is that the NE can be reasonably estimated for any crustal deformation model using our statistical approach, without detailed knowledge of the network configuration. We considered in this thesis several related methods of various degrees of rigour for computing this estimate, but it turned out that, given the $1/\sqrt{N}$ scaling of the NE with the network size N, the crudest method in Equation 3.21,

$$\Delta T \approx \frac{\mathrm{std}(\mathbf{u})}{\sqrt{N}}, \qquad \Delta D \approx \frac{\mathrm{std}(s)}{\sqrt{N}}, \qquad \Delta R \approx \frac{\mathrm{std}(\mathbf{w})}{\sqrt{N}} \tag{7.1}$$

is often sufficient to estimate the NE. Here, as usual, ΔT, ΔD, and ΔR are the expected biases in the translation, the scale, and the rotation Helmert parameters (HPs) respectively, $\mathbf{u}$ is the surface displacement field, and s and $\mathbf{w}$ are fields associated with respectively the scale and the rotation,

$$\mathbf{w}(\mathbf{r}) = \frac{3}{2}\,\frac{\mathbf{r}\times\mathbf{u}(\mathbf{r})}{r_\oplus^2}, \qquad s(\mathbf{r}) = \frac{\mathbf{r}\cdot\mathbf{u}(\mathbf{r})}{r_\oplus^2} \tag{7.2}$$

where $\mathbf{r}$ is the position vector and $r_\oplus$ is the radius of the spherical Earth.

We recall that in Section 3.4 we also derived a set of analytical formulae to calculate the standard deviations required in these equations from the coefficients of the surface displacement field in its vector spherical harmonics decomposition. Therefore the calculation of this expected bias is straightforward and can be seamlessly incorporated into any deformation model.

As we reported in Chapters 4 and 5, the expected bias in general performed well as an estimate of the NE for both the instantaneous and the time-dependent displacement fields in our simulations. In most cases, the computed NE was within an order of magnitude of the expected bias, and more often than not, the accuracy of the estimation was even better.

However, in the case of ITRF core site networks that have been carefully selected to avoid significant non-linear motion, our method over-estimated the error due to coseismic displacements. Nevertheless, we remedied this shortcoming of our method by carrying out our calculation of the expected bias after we excluded the near field to model the enforcement of this criteria. We found that, in practice, the

simple choice of half the distance from the epicentre to the nearest station as the radius of the excluded cap resulted in a satisfactory estimate of the NE.

Our analysis also showed that the NE becomes particularly serious when a single station in a small network records substantial displacement. In particular, in the case of the 2011 Tōhoku–Oki earthquake, the VLBI station at Kashima, Japan, recorded a coseismic offset of ∼900 mm, which resulted in a GC motion of more than 2 mm measured by the ITRF core site networks of ∼140 stations. In contrast, the GC motion recorded by the same networks for the Sumatra–Andaman earthquake, where there were no stations in the immediate vicinity of the epicentre, was only ∼0.1 mm.

Finally, our proposed Centre of Weighted Network (CWN) frame, which incorporates weights proportional to the area represented by a station into its measurements, performed generally better than the geometric Centre of Network (CN) frame. For the drifts in the derivative HPs caused by surface water movements, the NE was reduced by ∼50% on an average for the CWN frame compared to the CN frame.

Even though GC motion detection by the CWN frame for the coseismic case was also in general better than the CN frame, the inclusion of the station in Kashima, Japan for the Tōhoku–Oki earthquake was again problematic, and enhanced the NE by ∼40–80% in the shifts in the HPs. As it happens, on top of the station being in the near field of the earthquake, there were no other core sites on the Pacific Ocean side of the earthquake epicentre, resulting in an exceptionally large Voronoi cell being assigned to the site. This magnified the contribution of the site to the GC motion measurement.

7.2 Future plans

Initially for this project we also wanted to investigate the NE caused by the post-seismic relaxation (PSR) due a great earthquake. It is interesting as a time-varying phenomenon that ends in a permanent static shift in the GC, Earth orientation and the length of the day (LOD). Furthermore, while the relaxation takes place, the TRF constructed from station positions that are affected by it undergoes continuous frame deformation, which makes it theoretically challenging, and therefore

compelling, to investigate.

In fact, we carefully developed our code base with further research into PSR in mind. We developed much of the machinery needed to calculate the displacement field which can still be found in our code repository. We followed the approach of [*Pollitz*, 1992] of working in the Laplace transform of the motion where we need to find the roots of a set of characteristic equations in the variable conjugate to time. Although we implemented the root finding procedure for $n \geq 2$ for Maxwell rheology, we did not finish the program for $n = 0$ or $n = 1$, both of which require extra care. We plan to get back to that investigation in the future.

Another process of similar scope in the hydrological loading context is glacial isostatic adjustment (GIA). We note that, according to *Swenson et al.* [2008], the effect of GIA on GC motion is rather small, although that does not categorically rule out the possibility of a NE associated with it being significant.

We could also investigate the change in the LOD of Earth by coseismic deformation. This change arises through the change in the moment of inertia of the Earth that involves the degree-2 components of the displacement field [see, for example, *Chao and Gross*, 1987]. However, it is unclear whether NE plays an important role in this case.

In this thesis we investigated the effect of discrete sampling in space. But a similar sampling problem also appears in time in practice where data points are often missing, or the continual operation of a station is disrupted by, for example, instrumental changes or malfunction, or when new stations are introduced into a network, or stations are upgraded or retired. We suspect a stochastic approach similar to the one in this thesis might be also useful to characterise the error in GC measurements introduced by the intermittent observations of the positions of the stations of a geodetic network.

Appendix A

Mathematical notations and conventions

A.1 Spherical and Cartesian coordinates

With our geocentric applications in mind, the transformation laws between the spherical coordinates (r, θ, ϕ) and the Cartesian coordinates (x, y, z) are taken to be,

$$x = r \sin\theta \cos\phi \tag{A.1a}$$

$$y = r \sin\theta \sin\phi \tag{A.1b}$$

$$z = r \cos\theta \tag{A.1c}$$

and

$$r = \sqrt{x^2 + y^2 + z^2} \tag{A.2a}$$

$$\theta = \cos^{-1}\left(\frac{z}{r}\right) \tag{A.2b}$$

$$\phi = \tan^{-1}\left(\frac{y}{x}\right) \tag{A.2c}$$

where we interpret θ to be the co-latitude and ϕ to be the longitude. That is, the origin is situated at the centre of the spherical Earth, the z-axis goes through the north pole, and the x-axis goes through the intersection of the equator and the prime meridian. Here, the ordered set of unit vectors $\hat{\mathbf{r}}$, $\hat{\boldsymbol{\theta}}$, and $\hat{\boldsymbol{\phi}}$ in the spherical system, as well as $\hat{\mathbf{x}}$, $\hat{\mathbf{y}}$, and $\hat{\mathbf{z}}$ in the Cartesian system, has the right-handed orientation.

When a vector $\mathbf{v}$ is expressed in both coordinate systems as

$$\mathbf{v} = v_x\,\hat{\mathbf{x}} + v_y\,\hat{\mathbf{y}} + v_z\,\hat{\mathbf{z}} = v_r\,\hat{\mathbf{r}} + v_\theta\,\hat{\boldsymbol{\theta}} + v_\phi\,\hat{\boldsymbol{\phi}} \tag{A.3}$$

the components are related by

$$\begin{bmatrix} v_r \\ v_\theta \\ v_\phi \end{bmatrix} = \begin{bmatrix} \sin\theta\cos\phi & \sin\theta\sin\phi & \cos\theta \\ \cos\theta\cos\phi & \cos\theta\sin\phi & -\sin\theta \\ -\sin\phi & \cos\phi & 0 \end{bmatrix} \begin{bmatrix} v_x \\ v_y \\ v_z \end{bmatrix} \tag{A.4}$$

where the transformation matrix is orthogonal. Locally, $\hat{\mathbf{r}}$ points in the up direction, $\hat{\boldsymbol{\phi}}$ points east, and $\hat{\boldsymbol{\theta}}$ points south.

A.2 Spherical harmonics

For $m \geq 0$ we define the spherical harmonics,

$$Y_{nm}(\theta,\phi) = X_{nm}(\theta)\,e^{im\phi} \tag{A.5}$$

where the auxiliary function

$$X_{nm}(\theta) = (-1)^m \left(\frac{2n+1}{4\pi}\frac{(n-m)!}{(n+m)!}\right)^{\frac{1}{2}} P_{nm}(\cos\theta) \tag{A.6}$$

is convenient for our applications. Here, P_{nm} are the associated Legendre functions

$$P_{nm}(x) = \left(1-x^2\right)^{m/2} \frac{d^m}{dx^m} P_n(x) \tag{A.7}$$

and P_n are the Legendre polynomials

$$P_n(x) = \frac{1}{2^n\,n!}\frac{d^n}{dx^n}\left(x^2-1\right)^n \tag{A.8}$$

For $m > 0$, we define, following *Pollitz* [1996],

$$Y_{n,-m}(\theta,\phi) = (-1)^m Y^*_{nm}(\theta,\phi) \tag{A.9}$$

where $(\cdot)^*$ denotes complex conjugation. That is, for $m > 0$,

$$X_{n,-m}(\theta) = (-1)^m X_{nm}(\theta) \tag{A.10}$$

These spherical harmonics are normalised so that

$$\int_{\phi=0}^{2\pi}\int_{\theta=0}^{\pi} Y^*_{n',m'}Y_{nm}\,\sin\theta\,d\theta\,d\phi = \delta_{n,n'}\,\delta_{m,m'} \tag{A.11}$$

In order to highlight the geometric content of the above equation, we will write it as,

$$\int_{\mathbb{S}^2} Y^*_{n',m'}Y_{nm}\,d\Omega = \delta_{n,n'}\,\delta_{m,m'} \tag{A.12}$$

where $\mathbb{S}^2$ denotes the unit sphere, and $d\Omega = \sin\theta\,d\theta\,d\phi$ is the differential solid angle, or in other words, the differential area element on the unit sphere.

Besides the differential equations,

$$\frac{\partial}{\partial\phi}Y_{nm}(\theta,\phi) = imY_{nm}(\theta,\phi) \tag{A.13a}$$

$$\frac{\partial^2}{\partial\phi^2}Y_{nm}(\theta,\phi) = -m^2Y_{nm}(\theta,\phi) \tag{A.13b}$$

the spherical harmonics obey another useful relation, both of whose alternative forms

$$\frac{\partial^2}{\partial\theta^2}Y_{nm} + \cot\theta\frac{\partial}{\partial\theta}Y_{nm} + \left(n(n+1) - \frac{m^2}{\sin^2\theta}\right)Y_{nm} = 0 \tag{A.14a}$$

$$\frac{1}{\sin\theta}\,\frac{\partial}{\partial\theta}\left(\sin\theta\,\frac{\partial Y_{nm}}{\partial\theta}\right) + \left(n(n+1) - \frac{m^2}{\sin^2\theta}\right)Y_{nm} = 0 \tag{A.14b}$$

are useful in practice. Any square-integrable function on the unit sphere may be written as a linear combination of the spherical harmonics. This property, often referred to as the completeness property, is fundamental to the theory and the utility of the spherical harmonics.

For seismic applications, it is convenient to work in the epicentral coordinates of a point source where only the modes with $|m| \leq 2$ are excited [*Gilbert and Dziewonski*, 1975]. To express the strain components at the source, we will need to take the limit

$$\phi \to 0 \qquad \text{and} \qquad \theta \to 0 \tag{A.15}$$

of certain expressions involving the spherical harmonics. The first of these is relatively straightforward,

$$\lim_{\phi\to 0} Y_{nm}(\theta,\phi) = X_{nm}(\theta) \tag{A.16a}$$

$$\lim_{\phi\to 0} \frac{\partial Y_{nm}}{\partial \phi}(\theta,\phi) = imX_{nm}(\theta) \tag{A.16b}$$

$$\lim_{\phi\to 0} \frac{\partial^2 Y_{nm}}{\partial \phi^2}(\theta,\phi) = -m^2 X_{nm}(\theta) \tag{A.16c}$$

while for the second, the asymptotic form [see, for example, *Aki and Richards*, 2002, §8.1]

$$P_{nm}(\cos\theta) \;\to\; \frac{1}{2^m\, m!}\frac{(n+m)!}{(n-m)!}\theta^m \qquad \text{as} \;\; \theta\to 0 \;\; \text{ for } \;\; m\geq 0 \tag{A.17}$$

is extremely useful.

The degree-0 and degree-1 spherical harmonics have a particularly important role in this thesis. Therefore, we list them here explicitly,

$$Y_{00} = \frac{1}{\sqrt{4\pi}} \tag{A.18a}$$

$$Y_{10} = \sqrt{\frac{3}{4\pi}}\cos\theta \tag{A.18b}$$

$$Y_{11} = -\sqrt{\frac{3}{8\pi}}\sin\theta\, e^{i\phi} \tag{A.18c}$$

$$Y_{1,-1} = \sqrt{\frac{3}{8\pi}}\sin\theta\, e^{-i\phi} \tag{A.18d}$$

A.3 Vector spherical harmonics

The vector spherical harmonics are defined in terms of the spherical harmonics described in Appendix A.2 to be,

$$\mathbf{R}_{nm}(\theta,\phi) = Y_{nm}(\theta,\phi)\hat{\mathbf{r}} \tag{A.19a}$$

$$\mathbf{S}_{nm}(\theta,\phi) = \frac{\partial Y_{nm}}{\partial\theta}\hat{\boldsymbol{\theta}} + \frac{1}{\sin\theta}\frac{\partial Y_{nm}}{\partial\phi}\hat{\boldsymbol{\phi}} = \nabla_1 Y_{nm} \tag{A.19b}$$

$$\mathbf{T}_{nm}(\theta,\phi) = \frac{1}{\sin\theta}\frac{\partial Y_{nm}}{\partial\phi}\hat{\boldsymbol{\theta}} - \frac{\partial Y_{nm}}{\partial\theta}\hat{\boldsymbol{\phi}} = -\hat{\mathbf{r}}\times\nabla_1 Y_{nm} \tag{A.19c}$$

where

$$\nabla_1 = \hat{\boldsymbol{\theta}} \frac{\partial}{\partial \theta} + \hat{\boldsymbol{\phi}} \frac{1}{\sin\theta} \frac{\partial}{\partial \phi} \tag{A.20}$$

is the gradient operator on the surface of the unit sphere. The vector spherical harmonics are orthogonal in Euclidean space,

$$\mathbf{R}_{nm} \cdot \mathbf{S}_{nm} = 0 \tag{A.21a}$$
$$\mathbf{R}_{nm} \cdot \mathbf{T}_{nm} = 0 \tag{A.21b}$$
$$\mathbf{S}_{nm} \cdot \mathbf{T}_{nm} = 0 \tag{A.21c}$$

as well as in the space of square-integrable functions, known as the Hilbert space in mathematics [see, for example, *Arfken et al.*, 2011], defined on the surface of the unit sphere,

$$\int_{\mathbb{S}^2} \mathbf{R}^*_{n',m'} \cdot \mathbf{S}_{nm} \, d\Omega = 0 \tag{A.22a}$$
$$\int_{\mathbb{S}^2} \mathbf{R}^*_{n',m'} \cdot \mathbf{T}_{nm} \, d\Omega = 0 \tag{A.22b}$$
$$\int_{\mathbb{S}^2} \mathbf{S}^*_{n',m'} \cdot \mathbf{T}_{nm} \, d\Omega = 0 \tag{A.22c}$$

$$\int_{\mathbb{S}^2} \mathbf{R}^*_{n',m'} \cdot \mathbf{R}_{nm} \, d\Omega = \delta_{n,n'} \delta_{m,m'} \tag{A.22d}$$
$$\int_{\mathbb{S}^2} \mathbf{S}^*_{n',m'} \cdot \mathbf{S}_{nm} \, d\Omega = n(n+1) \, \delta_{n,n'} \delta_{m,m'} \tag{A.22e}$$
$$\int_{\mathbb{S}^2} \mathbf{T}^*_{n',m'} \cdot \mathbf{T}_{nm} \, d\Omega = n(n+1) \, \delta_{n,n'} \delta_{m,m'} \tag{A.22f}$$

The completeness property of the vector spherical harmonics states that any square-integrable vector field defined on the surface of a sphere can be expressed as a linear combination of these vector fields.

Appendix B

Derivation of selected formulae

Unless otherwise stated, we follow the same notations as in the main text.

B.1 Integrals of vector spherical harmonics

In our applications, we will need the values of the expressions,

$$\int_{\mathbb{S}^2} \mathbf{R}_{nm}\, d\Omega, \qquad \int_{\mathbb{S}^2} \mathbf{S}_{nm}\, d\Omega, \qquad \text{and} \int_{\mathbb{S}^2} \mathbf{T}_{nm}\, d\Omega$$

so we derive them in the following. For this purpose, it is helpful to note that the unit vectors in the spherical coordinate system from Section A.1

$$\hat{\mathbf{r}} = \sin\theta\cos\phi\,\hat{\mathbf{x}} + \sin\theta\sin\phi\,\hat{\mathbf{y}} + \cos\theta\,\hat{\mathbf{z}} \tag{B.1a}$$

$$\hat{\boldsymbol{\theta}} = \cos\theta\cos\phi\,\hat{\mathbf{x}} + \cos\theta\sin\phi\,\hat{\mathbf{y}} - \sin\theta\,\hat{\mathbf{z}} \tag{B.1b}$$

$$\hat{\boldsymbol{\phi}} = -\sin\phi\,\hat{\mathbf{x}} + \cos\phi\,\hat{\mathbf{y}} \tag{B.1c}$$

may be written in terms of the spherical harmonics listed in Equation A.18. We have,

$$\sin\theta\cos\phi = -\sqrt{\frac{2\pi}{3}}\left(Y_{11}^* - Y_{1,-1}^*\right) \tag{B.2a}$$

$$\sin\theta\sin\phi = -i\sqrt{\frac{2\pi}{3}}\left(Y_{11}^* + Y_{1,-1}^*\right) \tag{B.2b}$$

$$\cos\theta = \sqrt{\frac{4\pi}{3}}Y_{10}^* \tag{B.2c}$$

and therefore,

$$\begin{aligned}\hat{\mathbf{r}} &= Y^*_{1,-1}\cdot\sqrt{\frac{2\pi}{3}}\,(\hat{\mathbf{x}}-i\hat{\mathbf{y}}) + Y^*_{1,0}\cdot\sqrt{\frac{4\pi}{3}}\,\hat{\mathbf{z}} + Y^*_{1,1}\cdot\sqrt{\frac{2\pi}{3}}\,(-\hat{\mathbf{x}}-i\hat{\mathbf{y}}) \\ &= \sum_{m=-1}^{1} Y^*_{1,m}\,\boldsymbol{\Delta}_m \end{aligned} \tag{B.3}$$

where

$$\boldsymbol{\Delta}_0 = \sqrt{\frac{4\pi}{3}}\,\hat{\mathbf{z}} \tag{B.4a}$$

$$\boldsymbol{\Delta}_1 = -\sqrt{\frac{2\pi}{3}}\,(\hat{\mathbf{x}}+i\,\hat{\mathbf{y}}) \tag{B.4b}$$

$$\boldsymbol{\Delta}_{-1} = -\boldsymbol{\Delta}^*_1 = -\sqrt{\frac{2\pi}{3}}\,(-\hat{\mathbf{x}}+i\,\hat{\mathbf{y}}) \tag{B.4c}$$

This expansion, although not standard in the literature, proved to be extremely useful in our derivations. Note, however, that the quantities $\mathbf{E}_n^m$ defined in *Okubo and Endo* [1986] play essentially the same role as our $\boldsymbol{\Delta}_m$. Now it is evident that,

$$\int_{\mathbb{S}^2} \mathbf{R}_{nm}\,d\Omega = \int_{\mathbb{S}^2} Y_{nm}\,\hat{\mathbf{r}}\,d\Omega = \sum_{m'=-1}^{1} \boldsymbol{\Delta}_{m'}\int_{\mathbb{S}^2} Y_{nm}\,Y^*_{1,m'}\,d\Omega = \delta_{n,1}\boldsymbol{\Delta}_m \tag{B.5}$$

from the orthogonality relation in Equation A.12 of the spherical harmonics.

To evaluate $\int_{\mathbb{S}^2}\mathbf{T}_{nm}\,d\Omega$ and $\int_{\mathbb{S}^2}\mathbf{S}_{nm}\,d\Omega$, we note that

$$\hat{\boldsymbol{\theta}} = \frac{\partial\hat{\mathbf{r}}}{\partial\theta} \tag{B.6a}$$

$$\hat{\boldsymbol{\phi}} = \frac{1}{\sin\theta}\frac{\partial\hat{\mathbf{r}}}{\partial\phi} \tag{B.6b}$$

so that

$$\begin{aligned}\int_{\mathbb{S}^2} \mathbf{T}_{nm}\, d\Omega &= \int_{\mathbb{S}^2} \left(\frac{1}{\sin\theta} \frac{\partial Y_{nm}}{\partial \phi} \hat{\boldsymbol{\theta}} - \frac{\partial Y_{nm}}{\partial \theta} \hat{\boldsymbol{\phi}} \right) d\Omega \\ &= \sum_{m'=-1}^{1} \boldsymbol{\Delta}_{m'} \int_{\mathbb{S}^2} \left(\frac{1}{\sin\theta} \frac{\partial Y_{nm}}{\partial \phi} \cdot \frac{\partial Y^*_{1,m'}}{\partial \theta} - \frac{\partial Y_{nm}}{\partial \theta} \cdot \frac{1}{\sin\theta} \frac{\partial Y^*_{1,m'}}{\partial \phi} \right) d\Omega \\ &= \sum_{m'=-1}^{1} \boldsymbol{\Delta}_{m'} \int_{\mathbb{S}^2} \mathbf{T}_{nm} \cdot \mathbf{S}^*_{1,m'}\, d\Omega = \mathbf{0} \end{aligned} \tag{B.7}$$

$$\begin{aligned}\int_{\mathbb{S}^2} \mathbf{S}_{nm}\, d\Omega &= \int_{\mathbb{S}^2} \left(\frac{\partial Y_{nm}}{\partial \theta} \hat{\boldsymbol{\theta}} + \frac{1}{\sin\theta} \frac{\partial Y_{nm}}{\partial \phi} \hat{\boldsymbol{\phi}} \right) d\Omega \\ &= \sum_{m'=-1}^{1} \boldsymbol{\Delta}_{m'} \int_{\mathbb{S}^2} \left(\frac{\partial Y_{nm}}{\partial \theta} \cdot \frac{\partial Y^*_{1,m'}}{\partial \theta} + \frac{1}{\sin\theta} \frac{\partial Y_{nm}}{\partial \phi} \cdot \frac{1}{\sin\theta} \frac{\partial Y^*_{1,m'}}{\partial \phi} \right) d\Omega \\ &= \sum_{m'=-1}^{1} \boldsymbol{\Delta}_{m'} \int_{\mathbb{S}^2} \mathbf{S}_{nm} \cdot \mathbf{S}^*_{1,m'}\, d\Omega = n(n+1)\, \delta_{n,1}\, \boldsymbol{\Delta}_m = 2 \int_{\mathbb{S}^2} \mathbf{R}_{nm}\, d\Omega \end{aligned} \tag{B.8}$$

B.2 Shifts in Helmert parameters

Here we derive the expressions for $\mathbf{T}_{\mathrm{CF}}$ and $\mathbf{R}_{\mathrm{CF}}$ in Equation 2.6. For simplicity, let $\mathbf{T} = \mathbf{T}_{\mathrm{CF}}$ and $\mathbf{R} = \mathbf{R}_{\mathrm{CF}}$.

For the first, the approximating displacement field is given by a uniform translation $\mathbf{v} = \mathbf{T}$, and we minimise the error in the transformed coordinates with respect to $\mathbf{T}$,

$$\nabla_{\mathbf{T}} \int_{\partial\oplus} (\mathbf{u} - \mathbf{v})^2\, d\Omega = \mathbf{0} \Rightarrow \int_{\partial\oplus} (\mathbf{u} - \mathbf{T})\, d\Omega = \mathbf{0} \tag{B.9}$$

$$\Rightarrow \int_{\partial\oplus} \mathbf{u}\, d\Omega = \mathbf{T} \int_{\partial\oplus} d\Omega \tag{B.10}$$

$$\Rightarrow \mathbf{T} = \frac{1}{4\pi} \int_{\partial\oplus} \mathbf{u}\, d\Omega \tag{B.11}$$

where the gradient $\nabla_{\mathbf{T}}$ is taken with respect to the translation parameters.

For the second, the approximating field is the result of a uniform rotation around the $\mathbf{R}$ axis, that is, $\mathbf{v} = \mathbf{R} \times \mathbf{r}$. For notational simplicity, we minimise the error in the

transformed coordinates with respect to the R_x component first,

$$\frac{\partial}{\partial R_x}\int_{\partial\oplus}(\mathbf{u}-\mathbf{v})^2\,d\Omega=0\Rightarrow\int_{\partial\oplus}(\mathbf{u}-\mathbf{v})\cdot\frac{\partial\mathbf{v}}{\partial R_x}\,d\Omega=0 \tag{B.12}$$

But

$$\frac{\partial\mathbf{v}}{\partial R_x}=\frac{\partial}{\partial R_x}(\mathbf{R}\times\mathbf{r})=\frac{\partial\mathbf{R}}{\partial R_x}\times\mathbf{r}=\hat{\mathbf{x}}\times\mathbf{r} \tag{B.13}$$

So,

$$\int_{\partial\oplus}(\hat{\mathbf{x}}\times\mathbf{r})\cdot\mathbf{u}\,d\Omega=\int_{\partial\oplus}(\hat{\mathbf{x}}\times\mathbf{r})\cdot\mathbf{v}\,d\Omega \tag{B.14a}$$

and therefore

$$\hat{\mathbf{x}}\cdot\int_{\partial\oplus}\mathbf{r}\times\mathbf{u}\,d\Omega=\hat{\mathbf{x}}\cdot\int_{\partial\oplus}\mathbf{r}\times\mathbf{v}\,d\Omega \tag{B.14b}$$

by vector algebra. But this is just the x-component of the equation

$$\int_{\partial\oplus}\mathbf{r}\times\mathbf{u}\,d\Omega=\int_{\partial\oplus}\mathbf{r}\times\mathbf{v}\,d\Omega \tag{B.15}$$

and evidently the other two components of the last equation also hold by symmetry. Therefore,

$$\begin{aligned}\int_{\partial\oplus}\mathbf{r}\times\mathbf{u}\,d\Omega&=\int_{\partial\oplus}\mathbf{r}\times\mathbf{v}\,d\Omega=\int_{\partial\oplus}\mathbf{r}\times(\mathbf{R}\times\mathbf{r})\,d\Omega\\&=\int_{\partial\oplus}\big(\mathbf{R}\,r_\oplus^2-\mathbf{r}\,(\mathbf{R}\cdot\mathbf{r})\big)\,d\Omega=4\pi\,r_\oplus^2\,\mathbf{R}-r_\oplus^2\int_{\partial\oplus}(\mathbf{R}\cdot\hat{\mathbf{r}})\,\hat{\mathbf{r}}\,d\Omega\end{aligned} \tag{B.16}$$

To take advantage of the symmetry of the last integral, we temporarily set up a Cartesian coordinate system with the origin at the centre of the Earth and the z-axis parallel to $\mathbf{R}$ so that $\mathbf{R}=R\,\hat{\mathbf{z}}$. Since,

$$\hat{\mathbf{r}}=\sin\theta\cos\phi\,\hat{\mathbf{x}}+\sin\theta\sin\phi\,\hat{\mathbf{y}}+\cos\theta\,\hat{\mathbf{z}} \tag{B.17}$$

we have $\mathbf{R}\cdot\hat{\mathbf{r}}=R\cos\theta$, and therefore,

$$\begin{aligned}\int_{\partial\oplus}(\mathbf{R}\cdot\hat{\mathbf{r}})\,\hat{\mathbf{r}}\,d\Omega&=R\int_{\partial\oplus}\cos\theta\,\hat{\mathbf{r}}\,d\Omega=\sqrt{\frac{4\pi}{3}}R\int_{\partial\oplus}\hat{\mathbf{r}}\,Y_{10}\,d\Omega=\sqrt{\frac{4\pi}{3}}R\int_{\partial\oplus}\mathbf{R}_{10}\,d\Omega\\&=\sqrt{\frac{4\pi}{3}}R\,\boldsymbol{\Delta}_0=\frac{4\pi}{3}R\,\hat{\mathbf{z}}=\frac{4\pi}{3}\mathbf{R}\end{aligned} \tag{B.18a}$$

from Equations B.2, B.3, A.12, and B.4.

Thus,

$$\int_{\partial\oplus} \mathbf{r}\times\mathbf{u}\,d\Omega = \frac{8\pi\, r_\oplus^2}{3}\,\mathbf{R} \tag{B.19}$$

from which the expression for $\mathbf{R}_{\mathrm{CF}}$ follows. Interestingly, this last equation has an intuitive physical interpretation. If we imagine the Earth as a hollow sphere of uniform surface mass density so that the total mass $M = 4\pi$, then the left hand side of the equation is the total angular momentum $\mathbf{L}$ of the shell, provided we interpret $\mathbf{u}$ as a velocity field. Correspondingly, $\mathbf{R}$ would have to be identified as the angular velocity ω. Thus the equation can be recast to a more familiar form,

$$\mathbf{L} = I\,\omega \tag{B.20}$$

where

$$I = \frac{2\,M\,r_\oplus^2}{3} \tag{B.21}$$

which is, in fact, the standard expression for the moment of inertia of a hollow sphere of mass M and radius $r_\oplus$.

B.3 Helmert parameters from degree-0 and degree-1 modes

Here we derive Equation 2.14. In order to do so, we substitute the expansion

$$\mathbf{u} = \sum_{n=0}^{\infty}\sum_{m=-n}^{n} y^S_{1,nm}(r_\oplus)\,\mathbf{R}_{nm} + y^S_{3,nm}(r_\oplus)\,\mathbf{S}_{nm} + y^T_{1,nm}(r_\oplus)\,\mathbf{T}_{nm} \tag{B.22}$$

into the expressions

$$\mathbf{T}_{\mathrm{CF}} = \frac{1}{4\pi}\int_{\partial\oplus}\mathbf{u}\,d\Omega \tag{B.23a}$$

$$D_{\mathrm{CF}} = \frac{1}{4\pi r_\oplus^2}\int_{\partial\oplus}\mathbf{r}\cdot\mathbf{u}\,d\Omega \tag{B.23b}$$

$$\mathbf{R}_{\mathrm{CF}} = \frac{3}{8\pi r_\oplus^2}\int_{\partial\oplus}\mathbf{r}\times\mathbf{u}\,d\Omega \tag{B.23c}$$

For the translation parameters, we get

$$\begin{aligned}\mathbf{T}_{\mathrm{CF}} &= \frac{1}{4\pi}\sum_{n,m} y^S_{1,nm}(r_\oplus)\int_{\partial\oplus}\mathbf{R}_{nm}\,d\Omega + y^S_{3,nm}(r_\oplus)\int_{\partial\oplus}\mathbf{S}_{nm}\,d\Omega + y^T_{1,nm}(r_\oplus)\int_{\partial\oplus}\mathbf{T}_{nm}\,d\Omega \\ &= \frac{1}{4\pi}\sum_{n,m} y^S_{1,nm}(r_\oplus)\,\delta_{n,1}\,\boldsymbol{\Delta}_m + y^S_{3,nm}(r_\oplus)\,2\delta_{n,1}\,\boldsymbol{\Delta}_m \\ &= \frac{1}{4\pi}\sum_{m=-1}^{1}\left(y^S_{1,1,m}(r_\oplus) + 2\,y^S_{3,1,m}(r_\oplus)\right)\boldsymbol{\Delta}_m \end{aligned} \tag{B.24}$$

using results from Appendix B.1.

Since

$$\hat{\mathbf{r}}\cdot\mathbf{R}_{nm} = Y_{nm} \tag{B.25a}$$
$$\hat{\mathbf{r}}\cdot\mathbf{S}_{nm} = 0 \tag{B.25b}$$
$$\hat{\mathbf{r}}\cdot\mathbf{T}_{nm} = 0 \tag{B.25c}$$

we get for the scale parameter,

$$\begin{aligned} D_{\mathrm{CF}} &= \frac{1}{4\pi\,r_\oplus}\int_{\partial\oplus}\hat{\mathbf{r}}\cdot\mathbf{u}\,d\Omega \\ &= \frac{1}{4\pi\,r_\oplus}\sum_{n,m} y^S_{1,nm}(r_\oplus)\int_{\partial\oplus} Y_{nm}\,d\Omega \\ &= \frac{\sqrt{4\pi}}{4\pi\,r_\oplus}\sum_{n,m} y^S_{1,nm}(r_\oplus)\int_{\partial\oplus} Y_{nm}Y^*_{00}\,d\Omega \\ &= \frac{1}{\sqrt{4\pi}r_\oplus}\sum_{n,m} y^S_{1,nm}(r_\oplus)\,\delta_{n,0}\,\delta_{m,0} \\ &= \frac{1}{\sqrt{4\pi}r_\oplus}\,y^S_{1,00}(r_\oplus) \end{aligned} \tag{B.26}$$

Finally, since

$$\hat{\mathbf{r}}\times\mathbf{R}_{nm} = \mathbf{0} \tag{B.27a}$$
$$\hat{\mathbf{r}}\times\mathbf{S}_{nm} = -\mathbf{T}_{nm} \tag{B.27b}$$
$$\hat{\mathbf{r}}\times\mathbf{T}_{nm} = \mathbf{S}_{nm} \tag{B.27c}$$

we have

$$\begin{aligned}
\mathbf{R}_{\mathrm{CF}} &= \frac{3}{8\pi r_\oplus} \int_{\partial\oplus} \hat{\mathbf{r}} \times \mathbf{u}\, d\Omega \\
&= \frac{3}{8\pi r_\oplus} \sum_{n,m} -y^S_{3,nm}(r_\oplus) \int_{\partial\oplus} \mathbf{T}_{nm}\, d\Omega + y^T_{1,nm}(r_\oplus) \int_{\partial\oplus} \mathbf{S}_{nm}\, d\Omega \\
&= \frac{3}{8\pi r_\oplus} \sum_{n,m} y^T_{1,nm}(r_\oplus)\, 2\delta_{n,1}\, \boldsymbol{\Delta}_m \\
&= \frac{3}{8\pi r_\oplus} \sum_{m=-1}^{1} 2y^T_{1,1m}(r_\oplus)\, \boldsymbol{\Delta}_m
\end{aligned} \tag{B.28}$$

B.4 Conservation of linear and angular momenta

Here we derive Equation 2.18. Our expansion of the displacement field is,

$$\mathbf{u} = \sum_{n=0}^{\infty} \sum_{m=-n}^{n} y^S_{1,nm}\, \mathbf{R}_{nm} + y^S_{3,nm}\, \mathbf{S}_{nm} + y^T_{1,nm}\, \mathbf{T}_{nm} \tag{B.29}$$

When we substitute this expansion into the equation for the conservation of linear momentum we get,

$$\begin{aligned}
\mathbf{0} &= \sum_{n,m} \int_0^{r_\oplus} \rho\, r^2\, dr \left(y^S_{1,nm} \int_{\mathbb{S}^2} \mathbf{R}_{nm}\, d\Omega + y^S_{3,nm} \int_{\mathbb{S}^2} \mathbf{S}_{nm}\, d\Omega + y^T_{1,nm} \int_{\mathbb{S}^2} \mathbf{T}_{nm}\, d\Omega \right) \\
&= \sum_{n,m} \int_0^{r_\oplus} \rho\, r^2\, dr \left(y^S_{1,nm} + 2y^S_{3,nm} \right) \delta_{n,1}\, \boldsymbol{\Delta}_m \\
&= \sum_{m=-1}^{1} \int_0^{r_\oplus} \rho\, r^2\, dr \left(y^S_{1,1,m} + 2y^S_{3,1,m} \right) \boldsymbol{\Delta}_m
\end{aligned} \tag{B.30}$$

Since $\boldsymbol{\Delta}_m$ are linearly independent, it follows that

$$\int_0^{r_\oplus} \rho\, r^2\, dr \left(y^S_{1,1,m} + 2y^S_{3,1,m} \right) = 0 \tag{B.31}$$

for each $|m| \leq 1$. Similarly, for the conservation of angular momentum,

$$\begin{aligned}
\mathbf{0} &= \sum_{n,m} \int_0^{r_\oplus} \rho\, r^3\, dr\, \hat{\mathbf{r}} \times \left(y^S_{3,nm} \int_{\mathbb{S}^2} \mathbf{S}_{nm}\, d\Omega + y^T_{1,nm} \int_{\mathbb{S}^2} \mathbf{T}_{nm}\, d\Omega \right) \\
&= \sum_{n,m} \int_0^{r_\oplus} \rho\, r^3\, dr \left(-y^S_{3,nm} \int_{\mathbb{S}^2} \mathbf{T}_{nm}\, d\Omega + y^T_{1,nm} \int_{\mathbb{S}^2} \mathbf{S}_{nm}\, d\Omega \right) \\
&= \sum_{n,m} \int_0^{r_\oplus} \rho\, r^3\, dr\, 2y^T_{1,nm}\, \delta_{n,1}\, \boldsymbol{\Delta}_m \\
&= \sum_{m=-1}^{1} \int_0^{r_\oplus} \rho\, 2y^T_{1,1,m}\, r^3\, dr\, \boldsymbol{\Delta}_m
\end{aligned} \tag{B.32}$$

from which it follows that

$$\int_0^{r_\oplus} \rho\, y^T_{1,1,m}\, r^3\, dr = 0 \tag{B.33}$$

for each $|m| \leq 1$.

B.5 Transformation laws for the load Love numbers

The proof of Equation 2.98 is straightforward:

$$\begin{aligned}
\mathbf{m} &= \int_\oplus \mathbf{r}\, \rho\, dV \\
&= \int_{\partial\oplus} \left(\int_0^{r_\oplus} r\, \hat{\mathbf{r}}\, \sigma\, \delta(r - r_\oplus)\, r^2\, dr \right) d\Omega \\
&= r^3_\oplus \int_{\partial\oplus} \sigma\, \hat{\mathbf{r}}\, d\Omega \\
&= r^3_\oplus \sum_{n,m} \sigma_{nm} \int_{\partial\oplus} Y_{nm}\, \hat{\mathbf{r}}\, d\Omega \\
&= r^3_\oplus \sum_{n,m} \sigma_{nm} \int_{\partial\oplus} \mathbf{R}_{nm}\, d\Omega \\
&= r^3_\oplus \sum_{m=-1}^{1} \sigma_{1,m}\, \boldsymbol{\Delta}_m
\end{aligned} \tag{B.34}$$

Here, we have used the fact that the water layer is confined to the surface,

$$\rho = \sigma\, \delta(r - r_\oplus) \tag{B.35}$$

where it is described by the surface density σ, and we have also used the integral of the vector spherical harmonics $\mathbf{R}_{nm}$ from Appendix B.1.

Next, we derive Equation 2.104,

$$[h_1]_B = [h_1 - \alpha_B]_A \tag{B.36a}$$

$$[l_1]_B = [l_1 - \alpha_B]_A \tag{B.36b}$$

$$[k_1]_B = [k_1 - \alpha_B]_A \tag{B.36c}$$

We present the derivation here because not only is the algebra elided in *Blewitt* [2003], but also it is particularly transparent in our notation. Consider the displacement field

$$\mathbf{u} = \sum_{n',m'} y^S_{1,n',m'}\,\mathbf{R}_{n',m'} + y^S_{3,n',m'}\,\mathbf{S}_{n',m'} \tag{B.37}$$

as observed by the frames A and B, where frame B is the translation of frame A by the vector

$$[\mathbf{T}_B]_A = [\alpha_B]_A \frac{\mathbf{m}}{M_\oplus} \tag{B.38}$$

Evidently,

$$[\mathbf{u}]_B = [\mathbf{u}]_A - [\mathbf{T}_B]_A \tag{B.39}$$

To extract the degree-1 y^S_1 coefficients, we take the dot product of this equation with $\mathbf{R}^*_{1,m}$ and integrate over the Earth surface,

$$[y^S_{1,1,m}]_B = [y^S_{1,1,m}]_A - [\mathbf{T}_B]_A \cdot \int_{\partial\oplus} R^*_{1,m}\,d\Omega = [h_1]_A \frac{V_{1,m}}{g} - [\mathbf{T}_B]_A \cdot \mathbf{\Delta}^*_m \tag{B.40}$$

However,

$$\begin{aligned}
[\mathbf{T}_B]_A \cdot \mathbf{\Delta}^*_m &= [\alpha_B]_A \frac{\mathbf{m}\cdot\mathbf{\Delta}^*_m}{M_\oplus} \\
&= [\alpha_B]_A \frac{r^3_\oplus}{M_\oplus} \sum_{m'=-1}^{1} \sigma_{1,m'}\mathbf{\Delta}_{m'}\cdot\mathbf{\Delta}^*_m \\
&= [\alpha_B]_A \frac{\frac{4\pi}{3} r^3_\oplus}{M_\oplus}\sigma_{1,m} \\
&= [\alpha_B]_A \frac{V_{1,m}}{g}
\end{aligned} \tag{B.41}$$

since

$$\boldsymbol{\Delta}_{m'} \cdot \boldsymbol{\Delta}^*_m = \frac{4\pi}{3}\,\delta_{m,m'} \tag{B.42}$$

Thus,

$$[y^S_{1,1,m}]_B = [h_1 - \alpha_B]_A \frac{V_{1,m}}{g} = [h_1]_B \frac{V_{1,m}}{g} \tag{B.43}$$

that is,

$$[h_1]_B = [h_1 - \alpha_B]_A \tag{B.44}$$

If we take, in this proof, the dot product with $\mathbf{S}^*_{1,m}$ instead, we arrive at

$$[l_1]_B = [l_1 - \alpha_B]_A \tag{B.45}$$

To prove the last relation in Equation 2.104, we note that

$$[U]_B = [U]_A - g\,[\mathbf{T}_B]_A \cdot \hat{\mathbf{r}} \tag{B.46}$$

This is because in the translated frame the Earth surface appears to be lowered by the height $[\mathbf{T}_B]_A \cdot \hat{\mathbf{r}}$ and hence the gravitational potential is also lowered by the corresponding amount. Following the same steps as before but this time multiplying by $Y^*_{1,m}$ before integrating, we get

$$[k_1]_B = [k_1 - \alpha_B]_A \tag{B.47}$$

which ends the required derivation of the transformation laws. Notice that we have treated $V_{1,m}$ as a frame-independent quantity, since

$$\frac{\mathbf{m} \cdot \boldsymbol{\Delta}^*_m}{M_\oplus} = \frac{V_{1,m}}{g} \tag{B.48}$$

and $\mathbf{m}$ is not sensitive to the choice of the reference frame under our assumptions.

To derive Equation 2.108, we start with the results of *Blewitt* [2003],

$$[\alpha_{\mathrm{CE}}]_{\mathrm{CM}} = -1 \tag{B.49a}$$

$$[\alpha_{\mathrm{CF}}]_{\mathrm{CE}} = \frac{1}{3}[h_1 + 2l_1]_{\mathrm{CE}} \tag{B.49b}$$

and combine them to get,

$$[\alpha_{\mathrm{CF}}]_{\mathrm{CM}} = [\alpha_{\mathrm{CF}}]_{\mathrm{CE}} + [\alpha_{\mathrm{CE}}]_{\mathrm{CM}} = \frac{1}{3}[h_1 + 2l_1 - 3]_{\mathrm{CE}} \tag{B.50}$$

However, since

$$[h_1]_{\mathrm{CE}} = [h_1 - \alpha_{\mathrm{CE}}]_{\mathrm{CM}} = [h_1 + 1]_{\mathrm{CM}} \tag{B.51a}$$

$$[l_1]_{\mathrm{CE}} = [l_1 - \alpha_{\mathrm{CE}}]_{\mathrm{CM}} = [l_1 + 1]_{\mathrm{CM}} \tag{B.51b}$$

we have

$$[\alpha_{\mathrm{CF}}]_{\mathrm{CM}} = \frac{1}{3}[h_1 + 2l_1]_{\mathrm{CM}} \tag{B.52}$$

So, finally,

$$[1 + k_1]_{\mathrm{CF}} = [1 + k_1 - \alpha_{\mathrm{CF}}]_{\mathrm{CM}} = -[\alpha_{\mathrm{CF}}]_{\mathrm{CM}} = -\frac{1}{3}[h_1 + 2l_1]_{\mathrm{CM}} \tag{B.53}$$

Since $[k_1]_{\mathrm{CM}} = -1$.

B.6 Analytical formulae for expected bias

Here we derive Equation 3.24. We recall that the displacement field has the decomposition

$$\mathbf{u} = \sum_{n=0}^{\infty} \sum_{m=-n}^{n} \mathbf{u}_{nm} \tag{B.54a}$$

$$\mathbf{u}_{nm} = y^S_{1,nm}\, \mathbf{R}_{nm} + y^S_{3,nm}\, \mathbf{S}_{nm} + y^T_{1,nm}\, \mathbf{T}_{nm} \tag{B.54b}$$

Since we are here interested only in the surface displacement field, the y functions are evaluated at the Earth radius $r_\oplus$ and therefore we elide the radial argument for notational simplicity.

Therefore,

$$s_{nm} = \frac{1}{r_\oplus^2}\, \mathbf{r} \cdot \mathbf{u}_{nm} = \frac{1}{r_\oplus}\, y^S_{1,nm}\, Y_{nm} \tag{B.55a}$$

$$\mathbf{w}_{nm} = \frac{3}{2\, r_\oplus^2}\, \mathbf{r} \times \mathbf{u}_{nm} = \frac{3}{2\, r_\oplus} \left(-y^S_{3,nm}\, \mathbf{T}_{nm} + y^T_{1,nm}\, \mathbf{S}_{nm} \right) \tag{B.55b}$$

using Equations B.25 and B.27, where $s = \sum_{n,m} s_{nm}$, and $\mathbf{w} = \sum_{n,m} \mathbf{w}_{nm}$.

We need to evaluate

$$\int_{\partial\oplus} \mathbf{u}^2 \, d\Omega = \int_{\partial\oplus} \mathbf{u}^* \cdot \mathbf{u} \, d\Omega = \sum_{n',m'} \sum_{n,m} \int_{\partial\oplus} \mathbf{u}^*_{n',m'} \cdot \mathbf{u}_{nm} \, d\Omega \tag{B.56a}$$

$$\int_{\partial\oplus} s^2 \, d\Omega = \int_{\partial\oplus} s^* \cdot s \, d\Omega = \sum_{n',m'} \sum_{n,m} \int_{\partial\oplus} s^*_{n',m'} \cdot s_{nm} \, d\Omega \tag{B.56b}$$

$$\int_{\partial\oplus} \mathbf{w}^2 \, d\Omega = \int_{\partial\oplus} \mathbf{w}^* \cdot \mathbf{w} \, d\Omega = \sum_{n',m'} \sum_{n,m} \int_{\partial\oplus} \mathbf{w}^*_{n',m'} \cdot \mathbf{w}_{nm} \, d\Omega \tag{B.56c}$$

However, by Equations B.54, B.55, and A.22,

$$\int_{\partial\oplus} \mathbf{u}^*_{n',m'} \cdot \mathbf{u}_{nm} \, d\Omega = \delta_{n,n'} \delta_{m,m'} \times \left(y^{S*}_{1,n',m'} \, y^S_{1,nm} + n(n+1) \left(y^{S*}_{3,n',m'} \, y^S_{3,nm} + y^{T*}_{1,n',m'} \, y^T_{1,nm} \right) \right) \tag{B.57a}$$

$$\int_{\partial\oplus} s^*_{n',m'} \cdot s_{nm} \, d\Omega = \delta_{n,n'} \delta_{m,m'} \, \frac{1}{r_\oplus^2} \, y^{S*}_{1,n',m'} \, y^S_{1,nm} \tag{B.57b}$$

$$\int_{\partial\oplus} \mathbf{w}^*_{n',m'} \cdot \mathbf{w}_{nm} \, d\Omega = \delta_{n,n'} \delta_{m,m'} \, \frac{9}{4 r_\oplus^2} \, n(n+1) \left(y^{S*}_{3,n',m'} \, y^S_{3,nm} + y^{T*}_{1,n',m'} \, y^T_{1,nm} \right) \tag{B.57c}$$

Hence,

$$\int_{\partial\oplus} \mathbf{u}^2 \, d\Omega = \sum_{n,m} |y^S_{1,nm}|^2 + n(n+1) \left(|y^S_{3,nm}|^2 + |y^T_{1,nm}|^2 \right) \tag{B.58a}$$

$$\int_{\partial\oplus} s^2 \, d\Omega = \frac{1}{r_\oplus^2} \sum_{n,m} |y^S_{1,nm}|^2 \tag{B.58b}$$

$$\int_{\partial\oplus} \mathbf{w}^2 \, d\Omega = \frac{9}{4 r_\oplus^2} \sum_{n,m} n(n+1) \left(|y^S_{3,nm}|^2 + |y^T_{1,nm}|^2 \right) \tag{B.58c}$$

from which Equation 3.24 follows.

Appendix C

Equations of motion

Here we outline the derivation of the equations of motion introduced in Sections 2.5 and 2.7 for completeness. A relatively denser exposition of the material presented here can also be found in *Takeuchi and Saito* [1972].

C.1 Differential calculus in spherical coordinates

For convenience, we recall some elementary formulae for differentiation in spherical coordinates. The gradient of a scalar field f is given by

$$\nabla f = \hat{\mathbf{r}}\,\frac{\partial f}{\partial r} + \hat{\boldsymbol{\theta}}\,\frac{1}{r}\frac{\partial f}{\partial \theta} + \hat{\boldsymbol{\phi}}\,\frac{1}{r\sin\theta}\frac{\partial f}{\partial \phi} \tag{C.1}$$

The divergence of a vector field $\mathbf{u}$ has the form

$$\nabla\cdot\mathbf{u} = \frac{1}{r^2}\frac{\partial\left(r^2 u_r\right)}{\partial r} + \frac{1}{r\sin\theta}\frac{\partial(\sin\theta u_\theta)}{\partial\theta} + \frac{1}{r\sin\theta}\frac{\partial u_\phi}{\partial\phi} \tag{C.2}$$

and the Laplacian of a scalar field U can be written as

$$\nabla^2 U = \frac{1}{r^2}\frac{\partial}{\partial r}\left(r^2\frac{\partial U}{\partial r}\right) + \frac{1}{r^2\sin\theta}\frac{\partial}{\partial\theta}\left(\sin\theta\frac{\partial U}{\partial\theta}\right) + \frac{1}{r^2\sin^2\theta}\frac{\partial^2 U}{\partial\phi^2} \tag{C.3}$$

The gradient of a vector $\mathbf{u}$ is a tensor. Its components are:

$$(\nabla \mathbf{u})_{rr} = \frac{\partial u_r}{\partial r} \tag{C.4a}$$

$$(\nabla \mathbf{u})_{\theta\theta} = \frac{1}{r}\frac{\partial u_\theta}{\partial \theta} + \frac{u_r}{r} \tag{C.4b}$$

$$(\nabla \mathbf{u})_{\phi\phi} = \frac{1}{r\sin\theta}\frac{\partial u_\phi}{\partial \phi} + \frac{u_r}{r} + \frac{u_\theta \cot\theta}{r} \tag{C.4c}$$

$$(\nabla \mathbf{u})_{r\theta} = \frac{1}{r}\frac{\partial u_r}{\partial \theta} - \frac{u_\theta}{r} \tag{C.4d}$$

$$(\nabla \mathbf{u})_{\theta r} = \frac{\partial u_\theta}{\partial r} \tag{C.4e}$$

$$(\nabla \mathbf{u})_{r\phi} = \frac{1}{r\sin\theta}\frac{\partial u_r}{\partial \phi} - \frac{u_\phi}{r} \tag{C.4f}$$

$$(\nabla \mathbf{u})_{\phi r} = \frac{\partial u_\phi}{\partial r} \tag{C.4g}$$

$$(\nabla \mathbf{u})_{\theta\phi} = \frac{1}{r\sin\theta}\frac{\partial u_\theta}{\partial \phi} - \frac{u_\phi \cot\theta}{r} \tag{C.4h}$$

$$(\nabla \mathbf{u})_{\phi\theta} = \frac{1}{r}\frac{\partial u_\phi}{\partial \theta} \tag{C.4i}$$

If $\mathbf{u}$ is the displacement field, then the strain tensor E introduced in Equation 2.23 is

$$E = \frac{1}{2}\left((\nabla \mathbf{u}) + (\nabla \mathbf{u})^T\right) \tag{C.5}$$

where the superscript T denotes the transpose. Hence,

$$E_{rr} = \frac{\partial u_r}{\partial r} \tag{C.6a}$$

$$E_{\theta\theta} = \frac{1}{r}\frac{\partial u_\theta}{\partial \theta} + \frac{u_r}{r} \tag{C.6b}$$

$$E_{\phi\phi} = \frac{1}{r\sin\theta}\frac{\partial u_\phi}{\partial \phi} + \frac{u_r}{r} + \frac{u_\theta \cot\theta}{r} \tag{C.6c}$$

$$E_{r\theta} = E_{\theta r} = \frac{1}{2}\left(\frac{1}{r}\frac{\partial u_r}{\partial \theta} - \frac{u_\theta}{r} + \frac{\partial u_\theta}{\partial r}\right) \tag{C.6d}$$

$$E_{r\phi} = E_{\phi r} = \frac{1}{2}\left(\frac{1}{r\sin\theta}\frac{\partial u_r}{\partial \phi} - \frac{u_\phi}{r} + \frac{\partial u_\phi}{\partial r}\right) \tag{C.6e}$$

$$E_{\theta\phi} = E_{\phi\theta} = \frac{1}{2}\left(\frac{1}{r\sin\theta}\frac{\partial u_\theta}{\partial \phi} - \frac{u_\phi \cot\theta}{r} + \frac{1}{r}\frac{\partial u_\phi}{\partial \theta}\right) \tag{C.6f}$$

and the associated dilatation is

$$\operatorname{tr} E = \nabla \cdot \mathbf{u} = E_{rr} + E_{\theta\theta} + E_{\phi\phi} \tag{C.7}$$

where tr denotes the trace.

The divergence of a symmetric tensor σ is a vector whose components are

$$(\nabla \cdot \sigma)_r = \frac{1}{r^2}\frac{\partial\left(r^2\sigma_{rr}\right)}{\partial r} + \frac{1}{r\sin\theta}\left(\frac{\partial(\sin\theta\sigma_{r\theta})}{\partial\theta} + \frac{\partial\sigma_{r\phi}}{\partial\phi}\right) - \frac{1}{r}\left(\sigma_{\theta\theta} + \sigma_{\phi\phi}\right) \tag{C.8a}$$

$$(\nabla \cdot \sigma)_\theta = \frac{1}{r^2}\frac{\partial\left(r^2\sigma_{r\theta}\right)}{\partial r} + \frac{1}{r\sin\theta}\left(\frac{\partial(\sin\theta\sigma_{\theta\theta})}{\partial\theta} + \frac{\partial\sigma_{\theta\phi}}{\partial\phi}\right) + \frac{1}{r}\left(\sigma_{r\theta} - \sigma_{\phi\phi}\cot\theta\right) \tag{C.8b}$$

$$(\nabla \cdot \sigma)_\phi = \frac{1}{r^2}\frac{\partial\left(r^2\sigma_{r\phi}\right)}{\partial r} + \frac{1}{r\sin\theta}\left(\frac{\partial\left(\sin\theta\sigma_{\theta\phi}\right)}{\partial\theta} + \frac{\partial\sigma_{\phi\phi}}{\partial\phi}\right) + \frac{1}{r}\left(\sigma_{r\phi} + \sigma_{\theta\phi}\cot\theta\right) \tag{C.8c}$$

C.2 Hydrostatic equilibrium

We will use the same symbols and notations as in the main text unless otherwise stated. Unlike Section 2.5.1, we also consider gravity here, since it is necessary for Section 2.7. We can recover the case without gravity by setting the universal gravitational constant G to zero.

We start, following the original work of *Love* [1911], with a self-gravitating Earth in hydrostatic equilibrium. As usual, we consider here an SNREI Earth whose physical properties are spherically symmetric, that is, λ, μ, and ρ vary only with r. Consequently, other physical fields that we consider in this section also possess this property.

At equilibrium, Cauchy's equation in Equation 2.19 reads,

$$\nabla \cdot \sigma_0 + \mathbf{f}_0 = \mathbf{0} \tag{C.9}$$

Here, the body force $\mathbf{f}_0$ is gravitational,

$$\mathbf{f}_0 = \rho\, \mathbf{g}_0 \tag{C.10}$$

where the (vector) gravitational acceleration $\mathbf{g}_0$ points downwards:

$$\mathbf{g}_0 = -g\ \hat{\mathbf{r}} \tag{C.11}$$

The stress is given by a hydrostatic pressure,

$$\sigma_0 = -p_0 \tag{C.12}$$

and therefore behaves essentially as a scalar:

$$\nabla \cdot \sigma_0 = -\nabla p_0 \tag{C.13}$$

Combining all of these equations we arrive at

$$\nabla p_0 = \rho\ \mathbf{g}_0 = -\rho\ g\ \hat{\mathbf{r}} \tag{C.14}$$

subject to the boundary condition that $p_0(r_\oplus) = 0$.

Now, due to the conservative nature of the gravitational field, there is a gravitational potential field U_0 that satisfies

$$\mathbf{g}_0 = -\nabla U_0 \tag{C.15}$$

The potential also obeys Poisson's equation:

$$\nabla^2 U_0 = 4\pi\ G\ \rho \tag{C.16}$$

Of course, U_0 also only depends on r, and therefore the last two equations simplify to

$$g = \frac{dU_0}{dr} \tag{C.17}$$

and

$$\frac{1}{r^2}\frac{d}{dr}\left(r^2 \frac{dU_0}{dr}\right) = 4\pi\ G\ \rho \tag{C.18}$$

using Equations C.1 and C.3. Substituting C.17 in the last equation,

$$\frac{d}{dr}\left(r^2 g\right) = 4\pi\ G\ \rho\ r^2 \tag{C.19}$$

or,

$$g(r) = \frac{1}{r^2}\int_0^r 4\pi\ G\ \rho\ r^2\ dr \tag{C.20}$$

Thus, given an SNREI Earth model with a given ρ, the function g can be calculated immediately.

C.3 Consequences of deformation

Now consider this Earth under hydrostatic equilibrium undergoing an infinitesimal deformation $\mathbf{u}$ in response to some applied loading. We will, as usual, retain the induced changes in the quantities of interest that are first order, that is, linear, in $\mathbf{u}$, and disregard higher order terms when they occur.

To mitigate confusion, let us temporarily mark the equilibrium values of the fields with the subscript 0, the perturbations introduced by the deformation by the subscript 1, and the sum of these by the subscript 'total'. We will therefore attach the subscript 0 to symbols if needed when using the equations from the last section. The equations we want to solve for the deformed Earth are Poisson's equation,

$$\nabla^2 U_{\text{total}} = 4\pi\, G\, \rho_{\text{total}} \tag{C.21}$$

and, Cauchy's equation,

$$\nabla \cdot \sigma_{\text{total}} + \mathbf{f}_{\text{total}} = \mathbf{0} \tag{C.22}$$

which applies everywhere except the region where the loading is applied.

To calculate the change in density, consider the mass inside an arbitrary volume $\mathcal{V}$, where the change in mass inside is the mass that crossed its boundary $\partial\mathcal{V}$ [see, for example, *Aki and Richards*, 2002, §8.4],

$$\int_{\mathcal{V}} \rho_{\text{total}}\, dV = \int_{\mathcal{V}} \rho_0\, dV - \int_{\partial\mathcal{V}} (\rho_0\, \mathbf{u}) \cdot d\mathbf{A} \tag{C.23}$$

where dV and $d\mathbf{A}$ are the differential volume and area elements respectively. Applying Gauss' divergence theorem for any vector field $\mathbf{v}$,

$$\int_{\partial\mathcal{V}} \mathbf{v} \cdot d\mathbf{A} = \int_{\mathcal{V}} \nabla \cdot \mathbf{v}\, dV \tag{C.24}$$

we get

$$\int_{\mathcal{V}} \rho_{\text{total}}\, dV = \int_{\mathcal{V}} \rho_0\, dV - \int_{\mathcal{V}} \nabla \cdot (\rho_0 \mathbf{u})\, dV \tag{C.25}$$

and since the volume $\mathcal{V}$ is arbitrary, we conclude that

$$\rho_{\text{total}} = \rho_0 - \nabla \cdot (\rho_0 \mathbf{u}) \tag{C.26}$$

or, in other words,

$$\rho_1 = -\nabla \cdot (\rho_0 \mathbf{u}) \tag{C.27}$$

Subtracting Equation C.16,

$$\nabla^2 U_0 = 4\pi\, G\, \rho_0 \tag{C.28}$$

from Equation C.21 we get

$$\nabla^2 U_1 = 4\pi\, G\, \rho_1 = -4\pi\, G\, \nabla \cdot (\rho_0 \mathbf{u}) \tag{C.29}$$

Also, subtracting Equation C.15,

$$\mathbf{g}_0 = -\nabla U_0 \tag{C.30}$$

from

$$\mathbf{g}_{\text{total}} = -\nabla U_{\text{total}} \tag{C.31}$$

we get

$$\mathbf{g}_1 = -\nabla U_1 \tag{C.32}$$

We recall from the last section that,

$$\sigma_0 = -p_0 \tag{C.33a}$$
$$\nabla p_0 = \rho_0\, \mathbf{g}_0 \tag{C.33b}$$
$$\mathbf{g}_0 = -g\, \hat{\mathbf{r}} \tag{C.33c}$$

To find an expression for σ_{total}, we assume that when the material moves, it carries the equilibrium stress with it [see, for example, *Ben-Menahem and Singh*, 2012, §6.3.1]. Thus the total stress at a point after deformation is the sum of the equilibrium stress at the point it came from, and the additional stress caused by the strain induced by the deformation:

$$\begin{aligned}\sigma_{\text{total}}(\mathbf{r}) &= \sigma_0(\mathbf{r}-\mathbf{u}) + \sigma_1(\mathbf{r}) \\ &= -p_0(\mathbf{r}-\mathbf{u}) + \sigma_1(\mathbf{r}) = -p_0(\mathbf{r}) + \mathbf{u}\cdot\nabla p_0(\mathbf{r}) + \sigma_1(\mathbf{r})\end{aligned} \tag{C.34}$$

ignoring the higher order terms in $\mathbf{u}$. That is,

$$\sigma_{\text{total}} = -p_0 + \rho_0\,\mathbf{u}\cdot\mathbf{g}_0 + \sigma_1 \tag{C.35}$$

Consequently,

$$\begin{aligned}\nabla\cdot\sigma_{\text{total}} &= -\nabla p_0 + \nabla\big(\rho_0\,\mathbf{u}\cdot\mathbf{g}_0\big) + \nabla\cdot\sigma_1 \\ &= -\rho_0\,\mathbf{g}_0 + \nabla\big(\rho_0\,\mathbf{u}\cdot\mathbf{g}_0\big) + \nabla\cdot\sigma_1\end{aligned} \tag{C.36}$$

On the other hand,

$$\begin{aligned}\mathbf{f}_{\text{total}} &= \rho_{\text{total}}\,\mathbf{g}_{\text{total}} \\ &= (\rho_0+\rho_1)\big(\mathbf{g}_0+\mathbf{g}_1\big) \approx \rho_0\,\mathbf{g}_0 + \rho_0\,\mathbf{g}_1 + \rho_1\,\mathbf{g}_0\end{aligned} \tag{C.37}$$

neglecting the higher order term $\rho_1\,\mathbf{g}_1$. Substituting these values into Equation C.22,

$$\begin{aligned}\mathbf{0} &= \nabla\cdot\sigma_{\text{total}} + \mathbf{f}_{\text{total}} \\ &= \nabla\cdot\sigma_1 + \nabla\big(\rho_0\,\mathbf{u}\cdot\mathbf{g}_0\big) + \rho_0\,\mathbf{g}_1 + \rho_1\,\mathbf{g}_0 \\ &= \nabla\cdot\sigma_1 + \nabla\big(\rho_0\,\mathbf{u}\cdot\mathbf{g}_0\big) - \rho_0\,\nabla U_1 - \nabla\cdot(\rho_0\mathbf{u})\;\mathbf{g}_0 \\ &= \nabla\cdot\sigma_1 - \nabla\left(\rho_0\,g\,\mathbf{u}\cdot\hat{\mathbf{r}}\right) - \rho_0\,\nabla U_1 + \nabla\cdot(\rho_0\mathbf{u})\;g\,\hat{\mathbf{r}}\end{aligned} \tag{C.38}$$

Summarising, the equations to solve are,

$$\nabla\cdot\sigma_1 = \nabla\left(\rho_0\,g\,\mathbf{u}\cdot\hat{\mathbf{r}}\right) + \rho_0\,\nabla U_1 - \nabla\cdot(\rho_0\mathbf{u})\;g\,\hat{\mathbf{r}} \tag{C.39a}$$

$$\nabla^2 U_1 = -4\pi\,G\,\nabla\cdot(\rho_0\mathbf{u}) \tag{C.39b}$$

We can now safely drop the subscripts:

$$\nabla\cdot\sigma = \nabla\left(\rho\,g\,\mathbf{u}\cdot\hat{\mathbf{r}}\right) + \rho\,\nabla U - \nabla\cdot(\rho\mathbf{u})\;g\,\hat{\mathbf{r}} \tag{C.40a}$$

$$\nabla^2 U = -4\pi\,G\,\nabla\cdot(\rho\mathbf{u}) \tag{C.40b}$$

Note that U here is the perturbation in the potential field, and σ is the stress in response to material strain. This is consistent with the main text where the stress is caused entirely by strain in the absence of gravity.

C.4 Toroidal modes

For any toroidal mode of the displacement field,

$$\mathbf{u}^T_{nm}(r,\theta,\phi) = y^T_{1,nm}(r)\,\mathbf{T}_{nm}(\theta,\phi) \tag{C.41}$$

the components are:

$$u_r = 0 \tag{C.42a}$$

$$u_\theta = \frac{y_1}{\sin\theta}\frac{\partial Y}{\partial \phi} \tag{C.42b}$$

$$u_\phi = -y_1\frac{\partial Y}{\partial \theta} \tag{C.42c}$$

where we have suppressed the arguments, the spherical harmonics indices, and the superscript T indicating the toroidal mode for clarity and brevity.

From Equation C.2,

$$\nabla\cdot\mathbf{u} = \frac{1}{r\sin\theta}\left(\frac{\partial(\sin\theta u_\theta)}{\partial\theta} + \frac{\partial u_\phi}{\partial\phi}\right) \tag{C.43}$$

$$= \frac{y_1}{r\sin\theta}\left(\frac{\partial^2 Y}{\partial\theta\,\partial\phi} - \frac{\partial^2 Y}{\partial\phi\,\partial\theta}\right) = 0 \tag{C.44}$$

Therefore, the change in density due to deformation is,

$$-\nabla\cdot(\rho\,\mathbf{u}) = -\mathbf{u}\cdot\nabla\rho - \rho\,\nabla\cdot\mathbf{u} = -\mathbf{u}\cdot\hat{\mathbf{r}}\,\frac{d\rho}{dr} = -u_r\,\frac{d\rho}{dr} = 0 \tag{C.45}$$

using Equation C.1, and we see that the toroidal modes do not induce density changes, and consequently, changes in the gravitational field. Hence, the perturbation in the potential field,

$$U = 0 \tag{C.46}$$

In addition, since

$$u_r = \mathbf{r}\cdot\mathbf{u} = 0 \tag{C.47}$$

as well, Equation C.40a simplifies to,

$$\nabla\cdot\sigma = \mathbf{0} \tag{C.48}$$

So gravity is irrelevant to the toroidal modes. Furthermore, the constitutive relation in Equation 2.25,

$$\sigma = \lambda (\operatorname{tr} E) I + 2\mu E \tag{C.49}$$

also simplifies to

$$\sigma = 2\mu E \tag{C.50}$$

using Equation C.7.

From Equation C.6 we calculate,

$$E_{r\theta} = \frac{1}{2}\left(\frac{\partial u_\theta}{\partial r} - \frac{u_\theta}{r}\right) = \frac{1}{2}\left(\frac{dy_1}{dr} - \frac{y_1}{r}\right)\frac{1}{\sin\theta}\frac{\partial Y}{\partial \phi} \tag{C.51}$$

$$E_{r\phi} = \frac{1}{2}\left(\frac{\partial u_\phi}{\partial r} - \frac{u_\phi}{r}\right) = -\frac{1}{2}\left(\frac{dy_1}{dr} - \frac{y_1}{r}\right)\frac{\partial Y}{\partial \theta} \tag{C.52}$$

So,

$$\begin{aligned}\hat{\mathbf{r}} \cdot \sigma &= \hat{\mathbf{r}}\,\sigma_{rr} + \hat{\boldsymbol{\theta}}\,\sigma_{r\theta} + \hat{\boldsymbol{\phi}}\,\sigma_{r\phi} = 2\mu\left(\hat{\boldsymbol{\theta}}\,E_{r\theta} + \hat{\boldsymbol{\phi}}\,E_{r\phi}\right) \\ &= \mu\left(\frac{dy_1}{dr} - \frac{y_1}{r}\right)\left(\frac{1}{\sin\theta}\frac{\partial Y}{\partial \phi}\,\hat{\boldsymbol{\theta}} - \frac{\partial Y}{\partial \theta}\,\hat{\boldsymbol{\phi}}\right) = \mu\left(\frac{dy_1}{dr} - \frac{y_1}{r}\right)\mathbf{T}\end{aligned} \tag{C.53}$$

However, comparing with Equation 2.30b,

$$\hat{\mathbf{r}} \cdot \sigma = y_2\,\mathbf{T} \tag{C.54}$$

we see that

$$y_2 = \mu\left(\frac{dy_1}{dr} - \frac{y_1}{r}\right) \tag{C.55}$$

or,

$$\frac{dy_1}{dr} = \frac{y_1}{r} + \frac{y_2}{\mu} \tag{C.56}$$

which is one of the two equations we want to prove.

To find the other equation, we only need to consider the θ-component of Equation C.48. From Equation C.8,

$$\begin{aligned}(\nabla \cdot \sigma)_\theta &= \frac{1}{r^2}\frac{\partial\left(r^2\sigma_{r\theta}\right)}{\partial r} + \frac{1}{r\sin\theta}\left(\frac{\partial(\sin\theta\,\sigma_{\theta\theta})}{\partial\theta} + \frac{\partial\sigma_{\theta\phi}}{\partial\phi}\right) + \frac{1}{r}\left(\sigma_{r\theta} - \sigma_{\phi\phi}\cot\theta\right) \\ &= 0\end{aligned} \tag{C.57}$$

or, multiplying by $r^2 \sin\theta$,

$$\sin\theta \frac{\partial\left(r^2\sigma_{r\theta}\right)}{\partial r} + r\frac{\partial(\sin\theta\,\sigma_{\theta\theta})}{\partial\theta} + r\frac{\partial\sigma_{\theta\phi}}{\partial\phi} + r\sin\theta\,\sigma_{r\theta} - r\cos\theta\,\sigma_{\phi\phi} = 0 \tag{C.58}$$

Here,

$$\sigma_{r\theta} = \frac{y_2}{\sin\theta}\frac{\partial Y}{\partial\phi} \tag{C.59a}$$

$$\sigma_{\theta\theta} = 2\mu E_{\theta\theta} = \frac{2\mu}{r}\frac{\partial u_\theta}{\partial\theta} \tag{C.59b}$$

$$\sigma_{\theta\phi} = 2\mu E_{\theta\phi} = \mu\left(\frac{1}{r\sin\theta}\frac{\partial u_\theta}{\partial\phi} - \frac{u_\phi\cot\theta}{r} + \frac{1}{r}\frac{\partial u_\phi}{\partial\theta}\right) \tag{C.59c}$$

$$\sigma_{\phi\phi} = 2\mu E_{\phi\phi} = -2\mu E_{\theta\theta} = -\sigma_{\theta\theta} \tag{C.59d}$$

using Equation C.6, and the result that

$$\nabla\cdot\mathbf{u} = \operatorname{tr} E = E_{rr} + E_{\theta\theta} + E_{\phi\phi} = E_{\theta\theta} + E_{\phi\phi} = 0 \tag{C.60a}$$

so that

$$\sin\theta\,\sigma_{r\theta} = y_2\frac{\partial Y}{\partial\phi} \tag{C.61a}$$

$$r\,\sigma_{\theta\theta} = -r\,\sigma_{\phi\phi} = 2\mu E_{\theta\theta} = 2\mu\frac{\partial u_\theta}{\partial\theta} \tag{C.61b}$$

$$r\,\sigma_{\theta\phi} = 2\mu E_{\theta\phi} = \mu\left(\frac{1}{\sin\theta}\frac{\partial u_\theta}{\partial\phi} - u_\phi\cot\theta + \frac{\partial u_\phi}{\partial\theta}\right) \tag{C.61c}$$

In what follows, we will make liberal use of Equations A.13 and A.14 for simplifying expressions involving spherical harmonics. Then we have,

$$\sin\theta\,\sigma_{r\theta} = i\,m\,y_2\,Y \tag{C.62a}$$

$$r\,\sigma_{\theta\theta} = -r\,\sigma_{\phi\phi} = 2\mu\frac{i\,m\,y_1}{\sin\theta}\left(\frac{\partial Y}{\partial\theta} - \cot\theta\,Y\right) \tag{C.62b}$$

$$r\frac{\partial\sigma_{\theta\phi}}{\partial\phi} = i\,m\,\mu\,y_1\left(\cot\theta\frac{\partial Y}{\partial\theta} - \frac{\partial^2 Y}{\partial\theta^2} - \frac{m^2}{\sin^2\theta}Y\right) \tag{C.62c}$$

Substituting these into Equation C.58 and dividing by $i\,m\,Y$,

$$\begin{aligned}
0 &= \frac{\partial\left(r^2\,y_2\right)}{\partial r} + 2\mu\,\frac{y_1}{Y}\,\frac{\partial}{\partial\theta}\left(\frac{\partial Y}{\partial\theta} - \cot\theta\,Y\right) + \mu\,\frac{y_1}{Y}\left(\cot\theta\,\frac{\partial Y}{\partial\theta} - \frac{\partial^2 Y}{\partial\theta^2} - \frac{m^2}{\sin^2\theta}\,Y\right) \\
&\qquad + r\,y_2 + 2\mu\,\frac{y_1}{Y}\,\cot\theta\left(\frac{\partial Y}{\partial\theta} - \cot\theta\,Y\right) \\
&= r^2\,\frac{dy_2}{dr} + 3r\,y_2 + \mu\,\frac{y_1}{Y}\left(\cot\theta\,\frac{\partial Y}{\partial\theta} - \frac{\partial^2 Y}{\partial\theta^2} - \frac{m^2}{\sin^2\theta}\,Y\right) \\
&\qquad + 2\mu\,\frac{y_1}{Y}\left(\frac{\partial^2 Y}{\partial\theta^2} + \left(\csc^2\theta - \cot^2\theta\right)Y\right) \\
&= r^2\,\frac{dy_2}{dr} + 3r\,y_2 + \mu\,\frac{y_1}{Y}\left(\frac{\partial^2 Y}{\partial\theta^2} + \cot\theta\,\frac{\partial Y}{\partial\theta} - \frac{m^2}{\sin^2\theta}\,Y + 2Y\right) \\
&= r^2\,\frac{dy_2}{dr} + 3r\,y_2 + \mu\,\frac{y_1}{Y}\left(-n(n+1)\,Y + 2Y\right) \\
&= r^2\,\frac{dy_2}{dr} + 3r\,y_2 - \mu\,y_1\left(n^2 + n - 2\right)
\end{aligned} \tag{C.63}$$

Dividing by r^2,

$$\frac{dy_2}{dr} = \frac{\mu}{r^2}\,(n-1)(n+2)\,y_1 - \frac{3}{r}y_2 \tag{C.64}$$

Writing Equations C.56 and C.64 in matrix form we arrive at Equation 2.33.

C.5 Spheroidal modes

The components of a spheroidal mode of the displacement field

$$\mathbf{u}^S_{nm}(r,\theta,\phi) = y^S_{1,nm}(r)\,\mathbf{R}_{nm}(\theta,\phi) + y^S_{3,nm}(r)\,\mathbf{S}_{nm}(\theta,\phi) \tag{C.65}$$

are, in the simplified notation of the last section,

$$u_r = y_1\,Y \tag{C.66a}$$

$$u_\theta = y_3\,\frac{\partial Y}{\partial\theta} \tag{C.66b}$$

$$u_\phi = \frac{y_3}{\sin\theta}\,\frac{\partial Y}{\partial\phi} \tag{C.66c}$$

We also similarly decompose the perturbation in the scalar gravitational potential field,

$$U = -y_5\,Y \tag{C.67}$$

Now, Poisson's equation

$$\nabla^2 U = -4\pi\, G\, \nabla \cdot (\rho \mathbf{u}) \tag{C.68}$$

can be written as

$$\nabla \cdot \mathbf{C} = 0 \tag{C.69}$$

where we have defined

$$\mathbf{C} = \nabla U + \Gamma\, \mathbf{u} \tag{C.70a}$$

$$\Gamma = 4\pi\, G\, \rho \tag{C.70b}$$

At the interface between two homogeneous layers, imagine a small flat cylinder with one base just above the surface and the other just below. Applying Gauss' divergence theorem to this cylinder it can be shown [see, for example, *Aki and Richards*, 2002, §8.4] that the r-component of $\mathbf{C}$,

$$C_r = \mathbf{C} \cdot \hat{\mathbf{r}} = \frac{\partial U}{\partial r} + \Gamma\, u_r = \left(-\frac{dy_5}{dr} + \Gamma\, y_1 \right) Y \tag{C.71}$$

is continuous, and therefore, $dy_5/dr - \Gamma\, y_1$ can be adopted as a continuous function to solve for, even if ρ is discontinuous at layer boundaries. Following *Takeuchi and Saito* [1972], we will, however, define

$$y_6 = \frac{dy_5}{dr} - \Gamma\, y_1 + \frac{n+1}{r}\, y_5 \tag{C.72}$$

This can be rearranged to get one of the six equations we are to prove:

$$\frac{dy_5}{dr} = \Gamma\, y_1 - \frac{n+1}{r}\, y_5 + y_6 \tag{C.73}$$

This choice simplifies the boundary condition for y_6 at the Earth surface. To see this, notice that above the surface, that is, for $r > r_\oplus$, $\rho = 0$ and thus $\Gamma = 0$, and therefore Poisson's equation simplifies to Laplace's equation,

$$\begin{aligned} 0 = \nabla^2 U &= -\left(\frac{1}{r^2} \frac{\partial}{\partial r} \left(r^2 \frac{dy_5}{dr} \right) Y + \frac{y_5}{r^2} \left(\frac{1}{\sin\theta} \frac{\partial}{\partial \theta} \left(\sin\theta \frac{\partial Y}{\partial \theta} \right) - \frac{m^2}{\sin^2\theta}\, Y \right) \right) \\ &= -\left(\frac{1}{r^2} \frac{\partial}{\partial r} \left(r^2 \frac{dy_5}{dr} \right) Y - \frac{y_5}{r^2}\, n(n+1)\, Y \right) \end{aligned} \tag{C.74}$$

using Equation C.3. Therefore,

$$\frac{d}{dr}\left(r^2\,\frac{dy_5}{dr}\right) = n(n+1)\,y_5 \tag{C.75}$$

Being a second-order linear ordinary differential equation, it has two linearly independent solutions, and it can be verified by direct substitution that its most general solution is,

$$y_5 = A\,r^n + B\,r^{-(n+1)} \tag{C.76}$$

But since we want $U(\infty)$ to be regular, we must have $A = 0$, and so,

$$y_5 = B\,r^{-(n+1)} \tag{C.77}$$

Thus,

$$y_6 = \frac{dy_5}{dr} + \frac{n+1}{r}\,y_5 = B\left(-(n+1)\,r^{-(n+2)} + \frac{n+1}{r}\,r^{-(n+1)}\right) = 0 \tag{C.78}$$

and the continuity of y_6 at the Earth surface requires

$$y_6(r_\oplus) = 0 \tag{C.79}$$

Coming back to the region $r < r_\oplus$, we can now write

$$\begin{aligned}\mathbf{C} &= \hat{\mathbf{r}}\left(\Gamma\,y_1 - \frac{dy_5}{dr}\right) + \left(\Gamma\,y_3 - \frac{y_5}{r}\right)\left(\hat{\boldsymbol{\theta}}\,\frac{\partial Y}{\partial\theta} + \hat{\boldsymbol{\phi}}\,\frac{1}{\sin\theta}\frac{\partial Y}{\partial\phi}\right)\\ &= \hat{\mathbf{r}}\left(\frac{n+1}{r}\,y_5 - y_6\right)Y + \left(\Gamma\,y_3 - \frac{y_5}{r}\right)\left(\hat{\boldsymbol{\theta}}\,\frac{\partial Y}{\partial\theta} + \hat{\boldsymbol{\phi}}\,\frac{1}{\sin\theta}\frac{\partial Y}{\partial\phi}\right)\end{aligned} \tag{C.80}$$

so that

$$\begin{aligned}0 &= \nabla\cdot\mathbf{C}\\ &= \frac{1}{r^2}\frac{\partial}{\partial r}\left(r^2\left(\frac{n+1}{r}\,y_5 - y_6\right)\right)Y\\ &\qquad + \left(\Gamma\,y_3 - \frac{y_5}{r}\right)\frac{1}{r}\left(\frac{1}{\sin\theta}\frac{\partial}{\partial\theta}\left(\sin\theta\,\frac{\partial Y}{\partial\theta}\right) + \frac{1}{\sin^2\theta}\frac{\partial^2 Y}{\partial\phi^2}\right)\\ &= \frac{1}{r^2}\frac{\partial}{\partial r}\left(r\,(n+1)\,y_5 - r^2\,y_6\right)Y\\ &\qquad - \left(\Gamma\,y_3 - \frac{y_5}{r}\right)\frac{1}{r}\,n(n+1)\,Y\end{aligned} \tag{C.81}$$

Therefore,

$$\frac{n(n+1)}{r}\left(\Gamma y_3 - \frac{y_5}{r}\right) = \frac{n+1}{r^2}\left(r\frac{dy_5}{dr} + y_5\right) - \left(\frac{dy_6}{dr} + \frac{2}{r}y_6\right) \tag{C.82}$$

and

$$\begin{aligned}
\frac{dy_6}{dr} &= \frac{n+1}{r}\left(\frac{dy_5}{dr} + \frac{y_5}{r}\right) - \frac{2}{r}y_6 - \frac{n(n+1)}{r}\left(\Gamma y_3 - \frac{y_5}{r}\right) \\
&= \frac{n+1}{r}\left(y_6 + \Gamma y_1 - \frac{n+1}{r}y_5 + \frac{y_5}{r}\right) - \frac{2}{r}y_6 - \frac{n(n+1)}{r}\left(\Gamma y_3 - \frac{y_5}{r}\right) \\
&= \frac{n+1}{r}\left(y_6 + \Gamma y_1 - \frac{n}{r}y_5 - n\Gamma y_3 + \frac{n}{r}y_5\right) - \frac{2}{r}y_6 \\
&= \frac{n+1-2}{r}y_6 + \frac{n+1}{r}\Gamma y_1 - \frac{n(n+1)}{r}\Gamma y_3
\end{aligned} \tag{C.83}$$

using Equation C.73, or,

$$\frac{dy_6}{dr} = \frac{n+1}{r}\Gamma y_1 - \frac{n(n+1)}{r}\Gamma y_3 + \frac{n-1}{r}y_6 \tag{C.84}$$

which is another of the equations we are after.

We now turn to Equation C.40a

$$\begin{aligned}
\nabla\cdot\sigma &= \nabla(\rho\, g\, u_r) + \rho\,\nabla U - \nabla\cdot(\rho\mathbf{u})\; g\,\hat{\mathbf{r}} \\
&= (\nabla\rho)\, g\, u_r + \rho\,\nabla(g\,u_r) + \rho\,\nabla U - (\nabla\rho)\cdot\mathbf{u}\, g\,\hat{\mathbf{r}} - \rho\,\nabla\cdot\mathbf{u}\, g\,\hat{\mathbf{r}} \\
&= \frac{d\rho}{dr}\, g\, u_r\,\hat{\mathbf{r}} + \rho\,\nabla(g\,u_r) + \rho\,\nabla U - \frac{d\rho}{dr}\hat{\mathbf{r}}\cdot\mathbf{u}\, g\,\hat{\mathbf{r}} - \rho\,\nabla\cdot\mathbf{u}\, g\,\hat{\mathbf{r}} \\
&= \rho\,(\nabla U + \nabla(g\,u_r) - \nabla\cdot\mathbf{u}\, g\,\hat{\mathbf{r}}) \\
&= \rho\left(\nabla U + g\,\nabla u_r + \frac{dg}{dr}u_r\,\hat{\mathbf{r}} - \nabla\cdot\mathbf{u}\, g\,\hat{\mathbf{r}}\right)
\end{aligned} \tag{C.85}$$

using Equation C.1. From Equation C.20 we also have,

$$\frac{dg}{dr} = -\frac{2}{r^3}\int_0^r 4\pi\, G\,\rho\, r^2\, dr + \frac{1}{r^2}4\pi\, G\,\rho\, r^2 = -\frac{2}{r}g + \Gamma \tag{C.86}$$

Next, using Equation C.2 we evaluate,

$$\begin{aligned}
\nabla\cdot\mathbf{u} &= \frac{1}{r^2}\frac{\partial\left(r^2 y_1\right)}{\partial r}Y + \frac{y_3}{r}\left(\frac{1}{\sin\theta}\frac{\partial}{\partial\theta}\left(\sin\theta\frac{\partial Y}{\partial\theta}\right) + \frac{1}{\sin^2\theta}\frac{\partial^2 Y}{\partial\phi^2}\right) \\
&= \left(\frac{dy_1}{dr} + \frac{2}{r}y_1\right)Y + \frac{y_3}{r}\left(\frac{1}{\sin\theta}\frac{\partial}{\partial\theta}\left(\sin\theta\frac{\partial Y}{\partial\theta}\right) - \frac{m^2}{\sin^2\theta}\frac{\partial^2 Y}{\partial\phi^2}\right) \\
&= \left(\frac{dy_1}{dr} + \frac{2}{r}y_1 - \frac{n(n+1)}{r}y_3\right)Y
\end{aligned} \tag{C.87}$$

and therefore from the constitutive relation in Equation 2.25

$$\sigma = \lambda \nabla \cdot \mathbf{u}\, I + 2\mu\, E \tag{C.88}$$

we get, using Equation C.6,

$$\sigma_{rr} = \lambda \left(\frac{dy_1}{dr} + \frac{2}{r} y_1 - \frac{n(n+1)}{r} y_3 \right) Y + 2\mu \frac{dy_1}{dr} Y \tag{C.89a}$$

$$\sigma_{r\theta} = 2\mu \frac{1}{2} \left(\frac{y_1}{r} \frac{\partial Y}{\partial \theta} - \frac{y_3}{r} \frac{\partial Y}{\partial \theta} + \frac{dy_3}{dr} \frac{\partial Y}{\partial \theta} \right) \tag{C.89b}$$

$$\sigma_{r\phi} = 2\mu \frac{1}{2} \left(\frac{y_1}{r} \frac{1}{\sin\theta} \frac{\partial Y}{\partial \phi} - \frac{y_3}{r} \frac{1}{\sin\theta} \frac{\partial Y}{\partial \phi} + \frac{dy_3}{dr} \frac{1}{\sin\theta} \frac{\partial Y}{\partial \phi} \right) \tag{C.89c}$$

so that

$$\begin{aligned} \hat{\mathbf{r}} \cdot \sigma &= \hat{\mathbf{r}}\, \sigma_{rr} + \hat{\boldsymbol{\theta}}\, \sigma_{r\theta} + \hat{\boldsymbol{\phi}}\, \sigma_{r\phi} \\ &= \left((\lambda + 2\mu) \frac{dy_1}{dr} + \lambda \frac{2}{r} y_1 - \lambda \frac{n(n+1)}{r} y_3 \right) Y\, \hat{\mathbf{r}} \\ &\qquad + \mu \left(\frac{dy_3}{dr} + \frac{y_1}{r} - \frac{y_3}{r} \right) \left(\frac{\partial Y}{\partial \theta} \hat{\boldsymbol{\theta}} + \frac{1}{\sin\theta} \frac{\partial Y}{\partial \phi} \hat{\boldsymbol{\phi}} \right) \\ &= \left((\lambda + 2\mu) \frac{dy_1}{dr} + \lambda \frac{2}{r} y_1 - \lambda \frac{n(n+1)}{r} y_3 \right) \mathbf{R} + \mu \left(\frac{dy_3}{dr} + \frac{y_1}{r} - \frac{y_3}{r} \right) \mathbf{S} \end{aligned} \tag{C.90}$$

Comparing with Equation 2.30a,

$$\hat{\mathbf{r}} \cdot \sigma = y_2\, \mathbf{R} + y_4\, \mathbf{S} \tag{C.91}$$

we find,

$$y_2 = \bar{\sigma} \frac{dy_1}{dr} + \lambda \frac{2}{r} y_1 - \lambda \frac{n(n+1)}{r} y_3 \tag{C.92a}$$

$$y_4 = \mu \left(\frac{dy_3}{dr} + \frac{y_1}{r} - \frac{y_3}{r} \right) \tag{C.92b}$$

where the modulus

$$\bar{\sigma} = \lambda + 2\mu \tag{C.93}$$

is denoted in the main text simply by σ following *Pollitz* [1992], but we refrain from doing so here in order to avoid confusion with the stress tensor. Rearranging,

$$\frac{dy_1}{dr} = -\frac{2\lambda}{\bar{\sigma}\, r} y_1 + \frac{y_2}{\bar{\sigma}} + \frac{\lambda\, n(n+1)}{\bar{\sigma}\, r} y_3 \tag{C.94}$$

$$\frac{dy_3}{dr} = -\frac{y_1}{r} + \frac{y_3}{r} + \frac{y_4}{\mu} \tag{C.95}$$

which are two more of the equations we want to prove.

We can now eliminate dy_1/dr from Equation C.87 using C.94,

$$\begin{aligned}\nabla\cdot\mathbf{u} &= \left(\frac{y_2}{\bar{\sigma}} - \frac{\lambda}{\bar{\sigma}\,r}\left(2\,y_1 - n(n+1)\,y_3\right) + \frac{1}{r}\left(2\,y_1 - n(n+1)\,y_3\right)\right) Y \\ &= \frac{y_2}{\bar{\sigma}}\,Y + \frac{1}{r}\left(1 - \frac{\lambda}{\bar{\sigma}}\right)\left(2\,y_1 - n(n+1)\,y_3\right) Y \end{aligned} \tag{C.96}$$

To derive the last two equations, we need to consider two different components of Equation C.85. The r-component reads, using Equations C.1 and C.86:

$$(\nabla\cdot\sigma)_r = \rho\left(\frac{\partial U}{\partial r} + g\,\frac{\partial u_r}{\partial r} + \left(\Gamma - \frac{2}{r}\,g\right)u_r - \nabla\cdot\mathbf{u}\,g\right) \tag{C.97}$$

where

$$(\nabla\cdot\sigma)_r = \frac{1}{r^2}\frac{\partial\left(r^2\sigma_{rr}\right)}{\partial r} + \frac{1}{r\sin\theta}\left(\frac{\partial(\sin\theta\,\sigma_{r\theta})}{\partial\theta} + \frac{\partial\sigma_{r\phi}}{\partial\phi}\right) - \frac{1}{r}\left(\sigma_{\theta\theta} + \sigma_{\phi\phi}\right) \tag{C.98}$$

from Equation C.8. We know from Equations C.90 and C.92 that

$$\sigma_{rr} = y_2\,Y \tag{C.99}$$

$$\sigma_{r\theta} = y_4\,\frac{\partial Y}{\partial\theta} \tag{C.100}$$

$$\sigma_{r\phi} = \frac{y_4}{\sin\theta}\,\frac{\partial Y}{\partial\phi} \tag{C.101}$$

To evaluate $\left(\sigma_{\theta\theta} + \sigma_{\phi\phi}\right)$, we take the trace of Equation C.88 to get

$$\operatorname{tr}\sigma = \sigma_{rr} + \sigma_{\theta\theta} + \sigma_{\phi\phi} = 3\lambda\,\nabla\cdot\mathbf{u} + 2\mu\,\nabla\cdot\mathbf{u} \tag{C.102}$$

that is,

$$\sigma_{\theta\theta} + \sigma_{\phi\phi} = (3\lambda + 2\mu)\,\nabla\cdot\mathbf{u} - \sigma_{rr} \tag{C.103}$$

Therefore, on one hand,

$$\begin{aligned}(\nabla\cdot\sigma)_r &= \rho\left(-\frac{dy_5}{dr}\,Y + g\left(\frac{dy_1}{dr}\,Y - \nabla\cdot\mathbf{u}\right) + \left(\Gamma - \frac{2}{r}\,g\right)y_1\,Y\right) \\ &= \rho\left(-\frac{dy_5}{dr} + g\left(\frac{n(n+1)}{r}\,y_3 - \frac{2}{r}\,y_1\right) + \left(\Gamma - \frac{2}{r}\,g\right)y_1\right) Y \\ &= \rho\left(-\left(\Gamma\,y_1 - \frac{n+1}{r}\,y_5 + y_6\right) + g\left(\frac{n(n+1)}{r}\,y_3 - \frac{4}{r}\,y_1\right) + \Gamma\,y_1\right) Y \\ &= \rho\left(\frac{n+1}{r}\,y_5 - y_6 + g\left(\frac{n(n+1)}{r}\,y_3 - \frac{4}{r}\,y_1\right)\right) Y \end{aligned} \tag{C.104}$$

using Equations C.87 and C.73. On the other hand,

$$\begin{aligned}(\nabla\cdot\sigma)_r &= \frac{1}{r^2}\frac{\partial\left(r^2\,y_2\right)}{\partial r}\,Y + \frac{y_4}{r}\left(\frac{1}{\sin\theta}\,\frac{\partial}{\partial\theta}\left(\sin\theta\,\frac{\partial Y}{\partial\theta}\right) - \frac{m^2}{\sin^2\theta}\,Y\right)\\ &\quad - \frac{1}{r}\left((3\lambda+2\mu)\,\nabla\cdot\mathbf{u} - y_2\,Y\right)\\ &= \frac{dy_2}{dr}\,Y + \frac{2}{r}\,y_2\,Y - \frac{n(n+1)}{r}\,y_4\,Y - \frac{1}{r}\,(3\lambda+2\mu)\,\frac{y_2}{\bar{\sigma}}\,Y\\ &\quad - \frac{1}{r^2}\,(3\lambda+2\mu)\left(1-\frac{\lambda}{\bar{\sigma}}\right)\left(2y_1 - n(n+1)\,y_3\right)\,Y + \frac{1}{r}\,y_2\,Y\\ &= \frac{dy_2}{dr}\,Y + \frac{1}{r}\left(3 - \frac{3\lambda+2\mu}{\bar{\sigma}}\right)y_2\,Y - \frac{n(n+1)}{r}\,y_4\,Y\\ &\quad - \frac{1}{r^2}\,(3\lambda+2\mu)\left(1-\frac{\lambda}{\bar{\sigma}}\right)\left(2y_1 - n(n+1)\,y_3\right)\,Y\end{aligned} \tag{C.105}$$

using Equation C.96. Therefore,

$$\begin{aligned}\frac{dy_2}{dr} &= \rho\,\frac{n+1}{r}\,y_5 - \rho\,y_6 + \rho\,g\left(\frac{n(n+1)}{r}\,y_3 - \frac{4}{r}\,y_1\right) - \frac{1}{r}\left(3 - \frac{3\lambda+2\mu}{\bar{\sigma}}\right)y_2\\ &\quad + \frac{n(n+1)}{r}\,y_4 + \frac{1}{r^2}\,(3\lambda+2\mu)\left(1-\frac{\lambda}{\bar{\sigma}}\right)\left(2\,y_1 - n(n+1)\,y_3\right)\end{aligned} \tag{C.106}$$

But using Equation 2.34,

$$\begin{aligned}(3\lambda+2\mu)\left(1-\frac{\lambda}{\bar{\sigma}}\right) &= (3\lambda+2\mu)\left(\frac{\bar{\sigma}-\lambda}{\bar{\sigma}}\right) = 2\,\frac{(3\lambda+2\mu)\,\mu}{\bar{\sigma}}\\ &= 2\,\frac{\lambda^2+2\lambda\,\mu+\lambda\,\mu+2\mu^2-\lambda^2}{\bar{\sigma}}\\ &= 2\,\frac{\lambda\,(\lambda+2\mu)+\mu\,(\lambda+2\mu)-\lambda^2}{\bar{\sigma}} = 2\left(\lambda+\mu-\frac{\lambda^2}{\bar{\sigma}}\right) = 2\,\gamma\end{aligned} \tag{C.107a}$$

$$\begin{aligned}3-\frac{3\lambda+2\mu}{\bar{\sigma}} &= \frac{3\lambda+6\mu-(3\lambda+2\mu)}{\bar{\sigma}}\\ &= \frac{4\mu}{\bar{\sigma}} = 2\,\frac{2\mu}{\bar{\sigma}} = 2\,\frac{\bar{\sigma}-\lambda}{\bar{\sigma}} = -2\left(\frac{\lambda}{\bar{\sigma}}-1\right)\end{aligned} \tag{C.107b}$$

so that

$$\begin{aligned}\frac{dy_2}{dr} &= \rho\,g\,\frac{n(n+1)}{r}\,y_3 - \rho\,g\,\frac{4}{r}\,y_1 + \frac{2}{r}\left(\frac{\lambda}{\bar{\sigma}}-1\right)y_2\\ &\quad + \frac{4\gamma}{r^2}\,y_1 - \frac{2\gamma}{r^2}\,n(n+1)\,y_3 + \frac{n(n+1)}{r}\,y_4 + \rho\,\frac{n+1}{r}\,y_5 - \rho\,y_6\end{aligned} \tag{C.108}$$

that is,

$$\frac{dy_2}{dr} = \frac{4}{r^2}\left(\gamma - \rho\, g\, r\right) y_1 + \frac{2}{r}\left(\frac{\lambda}{\bar{\sigma}} - 1\right) y_2 + \frac{n(n+1)}{r^2}\left(\rho\, g\, r - 2\gamma\right) y_3 + \frac{n(n+1)}{r} y_4 + \rho\, \frac{n+1}{r}\, y_5 - \rho\, y_6 \tag{C.109}$$

which is another of the required equations.

Next, consider the ϕ-component of Equation C.85:

$$\begin{aligned}\left(\nabla\cdot\sigma\right)_\phi &= \rho\left(\nabla U\right)_\phi + \rho\, g\left(\nabla u_r\right)_\phi \\ &= \frac{\rho}{r\sin\theta}\left(\frac{\partial U}{\partial\phi} + g\,\frac{\partial u_r}{\partial\phi}\right) = \frac{\rho}{r\sin\theta}\left(g\, y_1 - y_5\right)\frac{\partial Y}{\partial\phi}\end{aligned} \tag{C.110}$$

using Equation C.1, whereas from Equation C.8,

$$\left(\nabla\cdot\sigma\right)_\phi = \frac{1}{r^2}\frac{\partial\left(r^2\sigma_{r\phi}\right)}{\partial r} + \frac{1}{r\sin\theta}\left(\frac{\partial\left(\sin\theta\,\sigma_{\theta\phi}\right)}{\partial\theta} + \frac{\partial\sigma_{\phi\phi}}{\partial\phi}\right) + \frac{1}{r}\left(\sigma_{r\phi} + \sigma_{\theta\phi}\cot\theta\right) \tag{C.111}$$

Equating the two expressions and multiplying by $r\sin\theta$,

$$i\,m\rho\left(g\, y_1 - y_5\right) Y = \frac{\sin\theta}{r}\frac{\partial\left(r^2\sigma_{r\phi}\right)}{\partial r} + \frac{\partial\left(\sin\theta\,\sigma_{\theta\phi}\right)}{\partial\theta} + \frac{\partial\sigma_{\phi\phi}}{\partial\phi} + \sigma_{r\phi}\sin\theta + \sigma_{\theta\phi}\cos\theta \tag{C.112}$$

We already know that

$$\sigma_{r\phi} = \frac{y_4}{\sin\theta}\frac{\partial Y}{\partial\phi} = \frac{i\,m\,y_4}{\sin\theta}\, Y \tag{C.113}$$

Let us then evaluate $\sigma_{\theta\phi}$ and $\sigma_{\phi\phi}$. Using Equation C.6,

$$\begin{aligned}\sigma_{\theta\phi} &= 2\mu\,\frac{1}{2}\left(\frac{y_3}{r\sin\theta}\frac{\partial}{\partial\phi}\frac{\partial Y}{\partial\theta} - \frac{y_3}{r\sin\theta}\cot\theta\,\frac{\partial Y}{\partial\phi} + \frac{y_3}{r}\frac{\partial}{\partial\theta}\left(\frac{1}{\sin\theta}\frac{\partial Y}{\partial\phi}\right)\right) \\ &= \frac{i\,m\,\mu\,y_3}{r\sin\theta}\left(\frac{\partial Y}{\partial\theta} - \cot\theta\, Y + \sin\theta\frac{\partial}{\partial\theta}\left(\frac{1}{\sin\theta}\, Y\right)\right) \\ &= \frac{i\,m\,\mu\,y_3}{r\sin\theta}\left(\frac{\partial Y}{\partial\theta} - \cot\theta\, Y + \frac{\partial Y}{\partial\theta} + \sin\theta\frac{\partial}{\partial\theta}\left(\frac{1}{\sin\theta}\right) Y\right) \\ &= \frac{2i\,m\,\mu\,y_3}{r\sin\theta}\left(\frac{\partial Y}{\partial\theta} - \cot\theta\, Y\right)\end{aligned} \tag{C.114}$$

and

$$\begin{aligned}\sigma_{\phi\phi} &= \lambda\,\nabla\cdot\mathbf{u} + 2\mu\,E_{\phi\phi}\\ &= \frac{\lambda}{\bar{\sigma}}\,y_2\,Y + \frac{1}{r}\left(\lambda - \frac{\lambda^2}{\bar{\sigma}}\right)\left(2y_1 - n(n+1)\,y_3\right)Y\\ &\qquad + 2\mu\left(\frac{y_3}{r\,\sin^2\theta}\,\frac{\partial^2 Y}{\partial\,\phi^2} + \frac{y_1}{r}\,Y + \frac{\cot\theta}{r}\,y_3\,\frac{\partial Y}{\partial\,\theta}\right)\\ &= \frac{\lambda}{\bar{\sigma}}\,y_2\,Y + \frac{1}{r}\,(\gamma-\mu)\left(2y_1 - n(n+1)\,y_3\right)Y\\ &\qquad + \frac{2\mu}{r}\left(y_1\,Y - \frac{m^2\,y_3}{\sin^2\theta}\,Y + \cot\theta\,y_3\,\frac{\partial Y}{\partial\,\theta}\right)\end{aligned} \tag{C.115}$$

Therefore,

$$\frac{\sin\theta}{r}\,\frac{\partial\left(r^2\sigma_{r\phi}\right)}{\partial\,r} + \sigma_{r\phi}\sin\theta = i\,m\,Y\left(\frac{1}{r}\,\frac{\partial\left(r^2\,y_4\right)}{\partial\,r} + y_4\right) = i\,m\,Y\left(r\,\frac{dy_4}{dr} + 3\,y_4\right) \tag{C.116}$$

and

$$\frac{\partial\,\sigma_{\phi\phi}}{\partial\,\phi} = i\,m\,\sigma_{\phi\phi} \tag{C.117}$$

and

$$\begin{aligned}\frac{\partial\left(\sin\theta\,\sigma_{\theta\phi}\right)}{\partial\,\theta} + \sigma_{\theta\phi}\cos\theta &= \frac{2i\,m\,\mu\,y_3}{r}\left(\frac{\partial^2 Y}{\partial\,\theta^2} + \csc^2\theta\,Y - \cot\theta\,\frac{\partial Y}{\partial\,\theta}\right.\\ &\qquad \left. + \cot\theta\,\frac{\partial Y}{\partial\,\theta} - \cot^2\theta\,Y\right)\\ &= \frac{2i\,m\,\mu\,y_3}{r}\left(\frac{\partial^2 Y}{\partial\,\theta^2} + Y\right)\end{aligned} \tag{C.118}$$

Substituting into Equation C.112 and dividing by $i\,m\,Y$:

$$\begin{aligned}\rho\,\left(g\,y_1 - y_5\right) = r\,\frac{dy_4}{dr} + 3\,y_4 + \frac{\lambda}{\bar{\sigma}}\,y_2 + \frac{1}{r}\,(\gamma-\mu)\left(2y_1 - n(n+1)\,y_3\right)\\ + \frac{2\mu}{r}\left(y_1 - \frac{m^2\,y_3}{\sin^2\theta} + y_3\,\frac{\cot\theta}{Y}\,\frac{\partial Y}{\partial\,\theta}\right) + \frac{2\mu}{r}\left(\frac{y_3}{Y}\,\frac{\partial^2 Y}{\partial\,\theta^2} + y_3\right)\end{aligned} \tag{C.119}$$

Dividing by r and rearranging,

$$\begin{aligned}\frac{dy_4}{dr} &= -\frac{\lambda}{\bar{\sigma}\, r}\, y_2 - \frac{3}{r}\, y_4 - \frac{\rho}{r}\, y_5 + \frac{\rho\, g}{r}\, y_1 + \frac{1}{r^2}\,(\mu-\gamma)\,(2y_1 - n(n+1)\, y_3) \\ &\qquad - \frac{2\mu}{r^2}\left(y_1 + \frac{y_3}{Y}\left(\frac{\partial^2 Y}{\partial\theta^2} + \cot\theta\,\frac{\partial Y}{\partial\theta} - \frac{m^2}{\sin^2\theta}\, Y\right) + y_3\right) \\ &= -\frac{\lambda}{\bar{\sigma}\, r}\, y_2 - \frac{3}{r}\, y_4 - \frac{\rho}{r}\, y_5 + \frac{\rho\, g}{r}\, y_1 + \frac{1}{r^2}\,(2\mu - 2\gamma)\, y_1 \\ &\qquad - \frac{1}{r^2}\,(\mu-\gamma)\, n(n+1)\, y_3 - \frac{2\mu}{r^2}\, y_1 + \frac{2\mu}{r^2}\, n(n+1)\, y_3 - \frac{2\mu}{r^2}\, y_3 \end{aligned} \tag{C.120}$$

or,

$$\frac{dy_4}{dr} = \frac{1}{r^2}\,(\rho\, g\, r - 2\gamma)\, y_1 - \frac{\lambda}{\bar{\sigma}\, r}\, y_2 + \frac{1}{r^2}\,(n(n+1)\,(\gamma+\mu) - 2\mu)\, y_3 - \frac{3}{r}\, y_4 - \frac{\rho}{r}\, y_5 \tag{C.121}$$

which is the last of the required equations.

Equations C.94, C.109, C.95, C.121, C.73, and C.84 constitute the system of equations to solve for spheroidal modes. In order to obtain Equation 2.32 in the main text from these, we only have to ignore the gravity terms and arrange the coefficients in a matrix.

C.6 Load Love numbers

Here we derive the equations in Section 2.7. Once again, unless otherwise stated, we use the symbols and the notation in the main text, as well as those introduced in this appendix.

The calculation of load Love numbers uses the equations of motion already derived in the previous section, Section C.5. However, the boundary conditions are modified to accommodate the presence of the load, that is, the water layer at the surface. The effect of the load are felt in two different ways: the load causes stress at the surface of the Earth due to its weight, and it contributes to the gravity field because of its mass.

The radial component of the stress, that is, the force per unit area on the surface of the Earth, is due the gravitational pull of the Earth on the load, acting downwards:

$$\hat{\mathbf{r}} \cdot T(r_\oplus, \theta, \phi) = -g(r_\oplus)\,\sigma\,\hat{\mathbf{r}} \tag{C.122}$$

that is,

$$\begin{aligned}\hat{\mathbf{r}} \cdot \sum_{nm} T_{nm}(r_\oplus, \theta, \phi) &= -g(r_\oplus) \sum_{nm} \sigma_{nm}\, \hat{\mathbf{r}}\, Y_{nm}(\theta, \phi) \\ &= -g(r_\oplus) \sum_{nm} \sigma_{nm}\, \mathbf{R}_{nm}(\theta, \phi) \end{aligned} \tag{C.123}$$

Here, to avoid confusion, we denote the stress tensor by T, even though the main text uses the symbol σ for it. The symbol σ in this appendix, however, stands for surface density of the water layer, as in Section 2.7. Comparing with the decomposition in Equation 2.30 rewritten in this notation,

$$\hat{\mathbf{r}} \cdot T^S_{nm}(r, \theta, \phi) = y^S_{2,nm}(r)\, \mathbf{R}_{nm}(\theta, \phi) + y^S_{4,nm}(r)\, \mathbf{S}_{nm}(\theta, \phi) \tag{C.124a}$$

$$\hat{\mathbf{r}} \cdot T^T_{nm}(r, \theta, \phi) = y^T_{2,nm}(r)\, \mathbf{T}_{nm}(\theta, \phi) \tag{C.124b}$$

we conclude that

$$y^S_{2,nm}(r_\oplus) = -g(r_\oplus)\, \sigma_{nm} \tag{C.125a}$$

$$y^S_{4,nm}(r_\oplus) = 0 \tag{C.125b}$$

$$y^T_{2,nm}(r_\oplus) = 0 \tag{C.125c}$$

Here, by Equation C.20,

$$g(r_\oplus) = \frac{G\, M_\oplus}{r_\oplus^2} \tag{C.126}$$

and we will refer to this value simply by g as in Section 2.7. Note that the boundary conditions on the toroidal modes force them to be identically zero, and therefore, the toroidal modes are irrelevant to this problem.

Now, the total perturbation U in the gravity field due to loading can be separated into two parts:

$$U = \widetilde{U} + V \tag{C.127}$$

where V is the load potential, that is, the gravitational potential created by the load directly because of its mass, and $\widetilde{U}$ is the change in gravitational potential due to deformation as in the previous section. Poisson's equation takes the form,

$$\nabla^2 \widetilde{U} = -4\pi\, G\, \nabla \cdot (\rho \mathbf{u}) \tag{C.128}$$

and

$$\nabla^2 V = 4\pi\, G\, \sigma\, \delta(r - r_\oplus) \tag{C.129}$$

for the two parts, and the sum of these equations provides the equation for the total potential. The consequences of the first of these two equations were derived in the previous section, so here we examine the second.

For both the inside ($r < r_\oplus$) and the outside ($r > r_\oplus$) of the Earth, Equation C.129 reduces to Laplace's equation,

$$\nabla^2 V = 0 \tag{C.130}$$

But consider a small flat cylinder, as in the previous section, with one base just above the Earth surface, and other just below. Integrating Equation C.129 over this cylinder and using Gauss' law we get,

$$\lim_{r \searrow r_\oplus} \frac{\partial V}{\partial r} - \lim_{r \nearrow r_\oplus} \frac{\partial V}{\partial r} = 4\pi\, G\, \sigma \tag{C.131}$$

where $\searrow$ and $\nearrow$ denote taking the limits from above and below, respectively.

We now expand the potentials in terms of their spherical harmonic components,

$$U = -\sum_{nm} y^S_{5,nm}\, Y_{nm} \tag{C.132a}$$

$$\widetilde{U} = -\sum_{nm} \widetilde{y}^S_{5,nm}\, Y_{nm} \tag{C.132b}$$

$$V = \sum_{nm} V_{nm}\, Y_{nm} = -\sum_{nm} x^S_{5,nm}\, Y_{nm} \tag{C.132c}$$

From now on, we consider a particular mode with fixed degree n and order m, and suppress these indices, along with the superscript S denoting spheroidal mode.

Following the developments in Section C.5, we define the variable,

$$y_6 = \frac{d\, y_5}{dr} - \Gamma\, y_1 + \frac{n+1}{r}\, y_5 \tag{C.133}$$

which is continuous except at $r = r_\oplus$. Since,

$$y_5 = \widetilde{y}_5 + x_5 \tag{C.134}$$

we have

$$y_6 = \frac{d\widetilde{y}_5}{dr} - \Gamma\, y_1 + \frac{n+1}{r}\,\widetilde{y}_5 + \frac{dx_5}{dr} + \frac{n+1}{r}\,x_5 = \widetilde{y}_6 + x_6 \tag{C.135}$$

where

$$\widetilde{y}_6 = \frac{d\widetilde{y}_5}{dr} - \Gamma\, y_1 + \frac{n+1}{r}\,\widetilde{y}_5 \tag{C.136}$$

is the y_6 from the last section due to deformation, and

$$x_6 = \frac{dx_5}{dr} + \frac{n+1}{r}\,x_5 \tag{C.137}$$

Reasoning similar to the previous section shows that

$$y_6 = \widetilde{y}_6 = x_6 = 0 \tag{C.138}$$

for $r > r_\oplus$, and also that the incorporation of the load potential leaves the equations of motion unchanged for $r < r_\oplus$, as it obeys Laplace's equation there. Thus the upshot of the presence of the load here is the boundary condition in Equation C.131, whose component form is,

$$\lim_{r \searrow r_\oplus} \frac{dx_5}{dr} - \lim_{r \nearrow r_\oplus} \frac{dx_5}{dr} = -4\pi\, G\, \sigma \tag{C.139}$$

And since the sums of the other terms in Equations C.137 and C.135 are continuous, we have,

$$\lim_{r \searrow r_\oplus} x_6 - \lim_{r \nearrow r_\oplus} x_6 = -4\pi\, G\, \sigma \tag{C.140}$$

$$\lim_{r \searrow r_\oplus} y_6 - \lim_{r \nearrow r_\oplus} y_6 = -4\pi\, G\, \sigma \tag{C.141}$$

But $x_6 = 0$ and $y_6 = 0$ for $r > r_\oplus$, which results in the boundary condition for our equations of motion inside the Earth,

$$y_6(r_\oplus) = 4\pi\, G\, \sigma \tag{C.142}$$

and also the relation

$$x_6(r_\oplus) = 4\pi\, G\, \sigma \tag{C.143}$$

Thus the deformation field due to the load of surface density σ_{nm} is given by the equations of motion of the previous section subject to the boundary conditions:

$$y^S_{2,nm}(r_\oplus) = -g\,\sigma_{nm} \tag{C.144}$$
$$y^S_{4,nm}(r_\oplus) = 0 \tag{C.145}$$
$$y^S_{6,nm}(r_\oplus) = 4\pi\,G\,\sigma_{nm} \tag{C.146}$$

for the spheroidal mode with degree n and order m.

Now, since the load potential V obeys Laplace's equation for $r < r_\oplus$,

$$x_5(r) = A\,r^n + B\,r^{-(n+1)} \tag{C.147}$$

by reasoning similar to that in the previous section, and we have resumed the suppression of subscripts and superscripts. However, since we require the solution to be regular at $r = 0$, we must have $B = 0$, and therefore,

$$x_5(r) = A\,r^n \tag{C.148}$$
$$x_6(r) = \frac{dx_5}{dr} + \frac{n+1}{r}\,x_5 = A\left(n\,r^{n-1} + (n+1)\,r^{n-1}\right) = A\,(2n+1)\,r^{n-1} \tag{C.149}$$

But using Equation C.143,

$$x_6(r_\oplus) = A\,(2n+1)\,r_\oplus^{n-1} = 4\pi\,G\,\sigma \tag{C.150}$$

and so,

$$x_5(r_\oplus) = A\,r_\oplus^n = \frac{4\pi\,G\,\sigma\,r_\oplus}{2n+1} \tag{C.151}$$

and consequently,

$$-\frac{V(r_\oplus)}{g} = \frac{x_5(r_\oplus)}{g} = \frac{4\pi\,r_\oplus^3}{M_\oplus}\,\frac{\sigma}{2n+1} \tag{C.152}$$

that is,

$$-\frac{V_{nm}(r_\oplus)}{g} = \frac{4\pi\,r_\oplus^3}{M_\oplus}\,\frac{\sigma_{nm}}{2n+1} \tag{C.153}$$

or Equation 2.90 in the notation of the main text.

We will retain the spherical harmonic indices and the subscript S for spheroidal modes for the rest of the section. In order to evaluate the load Love numbers, as explained in the main text, we can substitute

$$-\frac{V_{nm}(r_\oplus)}{g} = r_\oplus \tag{C.154}$$

into Equation 2.91,

$$y^S_{1,nm}(r_\oplus) = -h_n \frac{V_{nm}(r_\oplus)}{g} \tag{C.155a}$$

$$y^S_{3,nm}(r_\oplus) = -l_n \frac{V_{nm}(r_\oplus)}{g} \tag{C.155b}$$

to get

$$y^S_{1,nm}(r_\oplus) = h_n\, r_\oplus \tag{C.156a}$$

$$y^S_{3,nm}(r_\oplus) = l_n\, r_\oplus \tag{C.156b}$$

and also into Equation 2.92,

$$U_{nm}(r_\oplus) = (1+k_n)\, V_{nm}(r_\oplus) \tag{C.157}$$

to get

$$U_{nm}(r_\oplus) = -y^S_{5,nm}(r_\oplus) = -(1+k_n)\, g\, r_\oplus \tag{C.158}$$

Summarizing, we have,

$$y^S_{1,nm}(r_\oplus) = h_n\, r_\oplus \tag{C.159a}$$

$$y^S_{3,nm}(r_\oplus) = l_n\, r_\oplus \tag{C.159b}$$

$$y^S_{5,nm}(r_\oplus) = (1+k_n)\, g\, r_\oplus \tag{C.159c}$$

that is, Equation 2.97. Also, we have from Equation C.153,

$$r_\oplus = \frac{4\pi\, r_\oplus^3}{M_\oplus}\, \frac{\sigma_{nm}}{2n+1} \tag{C.160}$$

that is, the surface density corresponding to our specific values for the potential is,

$$\sigma_{nm} = (2n+1)\, \frac{M_\oplus}{4\pi\, r_\oplus^2} = (2n+1)\, \frac{g}{4\pi\, G} \tag{C.161}$$

Substituting this value into Equation C.144 we finally arrive at

$$y^S_{2,nm}(r_\oplus) = -\frac{(2n+1)\, g^2}{4\pi G} \tag{C.162a}$$

$$y^S_{4,nm}(r_\oplus) = 0 \tag{C.162b}$$

$$y^S_{6,nm}(r_\oplus) = (2n+1)\, g \tag{C.162c}$$

that is, Equation 2.96 in the main text.

Computationally, since the Love numbers do not depend on the order m, we can calculate their values by considering only the $m = 0$ components of σ_{nm} to be non-zero and given by Equation C.161 for each degree n. See *Farrell* [1972] for a nice physical interpretation of this surface density as a point mass.

Bibliography

Aki, K., and P. G. Richards (2002), *Quantitative Seismology*, University Science Books.

Altamimi, Z., and X. Collilieux (Eds.) (2013), *Reference frames for Applications in Geosciences*, Springer.

Altamimi, Z., P. Sillard, and C. Boucher (2002), ITRF2000: A new release of the International Terrestrial Reference Frame for earth science applications, *Journal of Geophysical Research: Solid Earth (1978–2012)*, *107*(B10), ETG–2.

Altamimi, Z., X. Collilieux, J. Legrand, B. Garayt, and C. Boucher (2007), ITRF2005: A new release of the International Terrestrial Reference Frame based on time series of station positions and Earth Orientation Parameters, *Journal of Geophysical Research: Solid Earth (1978–2012)*, *112*(B9).

Altamimi, Z., X. Collilieux, and L. Métivier (2011), ITRF2008: An improved solution of the International Terrestrial Reference Frame, *Journal of Geodesy*, *85*(8), 457–473.

Altamimi, Z., L. Métivier, and X. Collilieux (2012), ITRF2008 plate motion model, *Journal of Geophysical Research: Solid Earth*, *117*(B7).

Altamimi, Z., P. Rebischung, L. Métivier, and X. Collilieux (2016), ITRF2014: A new release of the International Terrestrial Reference Frame modeling non-linear station motions, *Journal of Geophysical Research: Solid Earth*.

Ammon, C., C. Ji, H. Thio, D. Robinson, S. Ni, V. Hjorleifsdottir, H. Kanamori, T. Lay, S. Das, D. Helmberger, et al. (2005), Rupture process of the 2004 Sumatra–Andaman earthquake, *Science*, *308*(5725), 1133.

Arfken, G. B., H. J. Weber, and F. E. Harris (2011), *Mathematical Methods for Physicists: A Comprehensive Guide*, Academic Press.

Argus, D. F., and R. G. Gordon (1991), No-net-rotation model of current plate velocities incorporating plate motion model NUVEL-1, *Geophysical Research Letters*, *18*(11), 2039–2042.

Banerjee, P., F. F. Pollitz, and R. Bürgmann (2005), The size and duration of the Sumatra–Andaman earthquake from far-field static offsets, *Science*, *308*(5729), 1769–1772.

Beckley, B., F. Lemoine, S. Luthcke, R. Ray, and N. Zelensky (2007), A reassessment of global and regional mean sea level trends from TOPEX and Jason-1 altimetry based on revised reference frame and orbits, *Geophysical Research Letters*, *34*(14).

Ben-Menahem, A., and S. J. Singh (2012), *Seismic Waves and Sources*, Springer Science & Business Media.

Ben-Menahem, A., S. J. Singh, and F. Solomon (1969), Static deformation of a spherical earth model by internal dislocations, *Bulletin of the Seismological Society of America*, *59*(2), 813–853.

Bevis, M., and A. Brown (2014), Trajectory models and reference frames for crustal motion geodesy, *Journal of Geodesy*, *88*(3), 283–311.

Blewitt, G. (2003), Self-consistency in reference frames, geocenter definition, and surface loading of the solid Earth, *Journal of Geophysical Research: Solid Earth (1978–2012)*, *108*(B2).

Blewitt, G., Z. Altamimi, J. Davis, R. Gross, C.-Y. Kuo, F. G. Lemoine, A. W. Moore, R. E. Neilan, H.-P. Plag, M. Rothacher, et al. (2010), Geodetic observations and global reference frame contributions to understanding sea-level rise and variability, *Understanding Sea-Level Rise and Variability*, pp. 256–284.

Bock, Y., and F. Webb (2012), MEaSUREs Solid Earth Science ESDR System, La Jolla, California and Pasadena, California USA, http://geoapp03.ucsd.edu/gridsphere/gridsphere.

Brown, K. Q. (1979), Geometric transforms for fast geometric algorithms, Ph.D. thesis, Carnegie-Mellon.

Caroli, M., P. M. de Castro, S. Loriot, O. Rouiller, M. Teillaud, and C. Wormser (2010), Robust and efficient Delaunay triangulations of points on or close to a sphere, in *International Symposium on Experimental Algorithms*, pp. 462–473, Springer.

Chao, B. F., and R. S. Gross (1987), Changes in the Earth's rotation and low-degree gravitational field induced by earthquakes, *Geophysical Journal International*, *91*(3), 569–596.

Chao, B. F., W. Chung, Z. Shih, and Y. Hsieh (2014), Earth's rotation variations: a wavelet analysis, *Terra Nova*, *26*(4), 260–264.

Collilieux, X., and G. Wöppelmann (2011), Global sea-level rise and its relation to the terrestrial reference frame, *Journal of Geodesy*, *85*(1), 9–22.

Collilieux, X., Z. Altamimi, J. Ray, T. van Dam, and X. Wu (2009), Effect of the satellite laser ranging network distribution on geocenter motion estimation, *Journal of Geophysical Research: Solid Earth*, *114*(B4).

Collilieux, X., Z. Altamimi, D. Coulot, T. van Dam, and J. Ray (2010), Impact of loading effects on determination of the International Terrestrial Reference Frame, *Advances in Space Research*, *45*(1), 144–154.

Crétaux, J.-F., L. Soudarin, F. J. Davidson, M.-C. Gennero, M. Bergé-Nguyen, and A. Cazenave (2002), Seasonal and interannual geocenter motion from SLR and DORIS measurements: Comparison with surface loading data, *Journal of Geophysical Research: Solid Earth*, *107*(B12).

Dahlen, F. A. (1968), The normal modes of a rotating, elliptical Earth, *Geophysical Journal International*, *16*(4), 329–367.

Delaunay, B. (1934), Sur la sphère vide, *Bulletin of Academy of Sciences of the USSR*, pp. 793–800.

Dermanis, A. (2004), The rank deficiency in estimation theory and the definition of reference systems, in *V Hotine-Marussi Symposium on Mathematical Geodesy*, edited by F. Sansò, pp. 145–156, Springer.

Dong, D., J. Dickey, Y. Chao, and M. Cheng (1997), Geocenter variations caused by atmosphere, ocean and surface ground water, *Geophysical Research Letters*, *24*(15), 1867–1870.

Dziewonski, A., T.-A. Chou, and J. Woodhouse (1981), Determination of earthquake source parameters from waveform data for studies of global and regional seismicity, *Journal of Geophysical Research: Solid Earth*, *86*(B4), 2825–2852.

Dziewonski, A. M., and D. L. Anderson (1981), Preliminary reference Earth model, *Physics of the Earth and Planetary Interiors*, *25*(4), 297–356.

Ekström, G., M. Nettles, and A. Dziewoński (2012), The global CMT project 2004–2010: Centroid-moment tensors for 13,017 earthquakes, *Physics of the Earth and Planetary Interiors*, *200*, 1–9.

Farrell, W. (1972), Deformation of the Earth by surface loads, *Reviews of Geophysics*, *10*(3), 761–797.

Fu, G., and W. Sun (2006), Global co-seismic displacements caused by the 2004 Sumatra–Andaman earthquake ($M_W = 9.1$), *Earth, Planets and Space*, *58*(2), 149.

Gilbert, F., and A. M. Dziewonski (1975), An application of normal mode theory to the retrieval of structural parameters and source mechanisms from seismic spectra, *Philosophical Transactions of the Royal Society of London A: Mathematical, Physical and Engineering Sciences*, *278*(1280), 187–269.

Gross, R. S., and B. F. Chao (2006), The rotational and gravitational signature of the December 26, 2004 Sumatran earthquake, *Surveys in Geophysics*, *27*(6), 615–632.

Han, S.-C., C. Shum, M. Bevis, C. Ji, and C.-Y. Kuo (2006), Crustal dilatation observed by GRACE after the 2004 Sumatra–Andaman earthquake, *Science*, *313*(5787), 658–662.

Haskell, N. A. (1953), The dispersion of surface waves on multilayered media, *Bulletin of the Seismological Society of America*, *43*(1), 17–34.

Herring, T., R. King, and S. McClusky (2002), GLOBK: Global Kalman filter VLBI and GPS analysis program Version 10.0, *Massachusetts Institute of Technology, Cambridge, MA*.

Herring, T., R. King, and S. McClusky (2008), Introduction to GAMIT/GLOBK, *Massachusetts Institute of Technology, Cambridge, MA*.

Kang, Z., B. Tapley, J. Chen, J. Ries, and S. Bettadpur (2009), Geocenter variations derived from GPS tracking of the GRACE satellites, *Journal of Geodesy*, *83*(10), 895–901.

Kovalevsky, J., I. I. Mueller, and B. Kolaczek (Eds.) (2012), *Reference frames: in Astronomy and Geophysics*, vol. 154, Springer Science & Business Media.

Kreemer, C., G. Blewitt, W. C. Hammond, and H.-P. Plag (2006), Global deformation from the great 2004 Sumatra–Andaman earthquake observed by GPS: Implications for rupture process and global reference frame, *Earth, Planets and Space*, *58*(2), 141–148.

Love, A. E. H. (1911), *Some problems of geodynamics*, Cambridge University Press.

Ma, C., E. Arias, T. Eubanks, A. Fey, A.-M. Gontier, C. Jacobs, O. Sovers, B. Archinal, and P. Charlot (1998), The International Celestial Reference Frame as realized by Very Long Baseline Interferometry, *The Astronomical Journal*, *116*(1), 516.

Mansinha, L., and D. Smylie (1971), The displacement fields of inclined faults, *Bulletin of the Seismological Society of America*, *61*(5), 1433–1440.

Melachroinos, S., F. Lemoine, N. Zelensky, D. Rowlands, S. Luthcke, and O. Bordyugov (2013), The effect of geocenter motion on Jason-2 orbits and the mean sea level, *Advances in Space Research*, *51*(8), 1323–1334.

Moore, M., C. Watson, M. King, S. Mcclusky, and P. Tregoning (2014), Empirical modelling of site-specific errors in continuous GPS data, *Journal of Geodesy*, *88*, doi: 10.1007/s00190-014-0729-5.

Moore, P., and J. Wang (2003), Geocentre variation from laser tracking of LAGEOS12 and loading data, *Advances in Space Research*, *31*(8), 1927–1933.

Nettles, M., G. Ekström, and H. C. Koss (2011), Centroid-moment-tensor analysis of the 2011 off the Pacific coast of Tohoku earthquake and its larger foreshocks and aftershocks, *Earth, Planets and Space*, *63*(7), 2.

Nishimura, T., H. Munekane, and H. Yarai (2011), The 2011 off the Pacific coast of Tohoku earthquake and its aftershocks observed by GEONET, *Earth, Planets and Space*, *63*(7), 22.

Okada, Y. (1985), Surface deformation due to shear and tensile faults in a half-space, *Bulletin of the Seismological Society of America*, *75*(4), 1135–1154.

Okubo, S., and T. Endo (1986), Static spheroidal deformation of degree 1 – consistency relation, stress solution and partials, *Geophysical Journal International*, *86*(1), 91–102.

Panet, I., V. Mikhailov, M. Diament, F. Pollitz, G. King, O. De Viron, M. Holschneider, R. Biancale, and J.-M. Lemoine (2007), Coseismic and post-seismic signatures of the Sumatra 2004 December and 2005 March earthquakes in GRACE satellite gravity, *Geophysical Journal International*, *171*(1), 177–190.

Plag, H.-P., and M. Pearlman (Eds.) (2009), *Global Geodetic Observing System: Meeting the requirements of a global society on a changing planet in 2020,* Springer Science & Business Media.

Pollitz, F. F. (1992), Postseismic relaxation theory on the spherical earth, *Bulletin of the Seismological Society of America*, *82*(1), 422–453.

Pollitz, F. F. (1996), Coseismic deformation from earthquake faulting on a layered spherical Earth, *Geophysical Journal International*, *125*(1), 1–14.

Press, F. (1965), Displacements, strains, and tilts at teleseismic distances, *Journal of Geophysical Research*, *70*(10), 2395–2412.

Renka, R. J. (1997), Algorithm 772: STRIPACK: Delaunay triangulation and Voronoi diagram on the surface of a sphere, *ACM Transactions on Mathematical Software*, *23*(3), 416–434, doi: 10.1145/275323.275329.

Rothacher, M., G. Beutler, T. A. Herring, and R. Weber (1999), Estimation of nutation using the Global Positioning System, *Journal of Geophysical Research: Solid Earth*, *104*(B3), 4835–4859.

Rummel, R., M. Rothacher, and G. Beutler (2005), Integrated Global Geodetic Observing System (IGGOS) —- science rationale, *Journal of Geodynamics*, *40*(4), 357–362.

Sabadini, R., and B. Vermeersen (2004), *Global Dynamics of the Earth: Applications of Normal Mode Relaxation Theory to Solid-Earth Geophysics*, Springer Science & Business Media.

Saito, M. (1967), Excitation of free oscillations and surface waves by a point source in a vertically heterogeneous earth, *Journal of Geophysical Research*, *72*, 3689.

Saito, M. (1974), Some problems of static deformation of the Earth, *Journal of Physics of the Earth*, *22*(1), 123–140.

Santamaría-Gómez, A., and A. Mémin (2015), Geodetic secular velocity errors due to interannual surface loading deformation, *Geophysical Journal International*, *202*(2), 763–767.

Shestakov, N. V., H. Takahashi, M. Ohzono, A. S. Prytkov, V. G. Bykov, M. D. Gerasimenko, M. N. Luneva, G. N. Gerasimov, A. G. Kolomiets, V. A. Bormotov, et al. (2012), Analysis of the far-field crustal displacements caused by the 2011 great Tohoku earthquake inferred from continuous GPS observations, *Tectonophysics*, *524*, 76–86.

Smylie, D., and L. Mansinha (1971), The elasticity theory of dislocations in real earth models and changes in the rotation of the earth, *Geophysical Journal International*, *23*(3), 329–354.

Stein, S., and M. Wysession (2009), *An Introduction to Seismology, Earthquakes, and Earth Structure*, John Wiley & Sons.

Steketee, J. (1958), On Volterra's dislocations in a semi-infinite elastic medium, *Canadian Journal of Physics*, *36*(2), 192–205.

Sun, W., and J. Dong (2014), Geo-center movement caused by huge earthquakes, *Journal of Geodynamics*, *76*, 1–7.

Sun, W., and S. Okubo (1993), Surface potential and gravity changes due to internal dislocations in a spherical earth – I. Theory for a point dislocation, *Geophysical Journal International*, *114*(3), 569–592.

Swenson, S., D. Chambers, and J. Wahr (2008), Estimating geocenter variations from a combination of GRACE and ocean model output, *Journal of Geophysical Research: Solid Earth*, *113*(B8).

Takeuchi, H., and M. Saito (1972), Seismic surface waves, *Methods in Computational Physics*, *11*, 217–295.

Tanimoto, T. (1986), The Backus–Gilbert approach to the 3-D structure in the upper mantle – II. SH and SV velocity, *Geophysical Journal International*, *84*(1), 49–69.

Tapley, B., J. Ries, S. Bettadpur, D. Chambers, M. Cheng, F. Condi, and S. Poole (2007), The GGM03 mean earth gravity model from GRACE, in *AGU Fall Meeting Abstracts*, vol. 1, p. 03.

Tapley, B. D., S. Bettadpur, M. Watkins, and C. Reigber (2004), The gravity recovery and climate experiment: Mission overview and early results, *Geophysical Research Letters*, *31*(9).

Tregoning, P., C. Watson, G. Ramillien, H. McQueen, and J. Zhang (2009), Detecting hydrologic deformation using GRACE and GPS, *Geophysical Research Letters*, *36*(15).

Tregoning, P., R. Burgette, S. McClusky, S. Lejeune, C. Watson, and H. McQueen (2013), A decade of horizontal deformation from great earthquakes, *Journal of Geophysical Research: Solid Earth*, *118*(5), 2371–2381.

Trupin, A. S., M. F. Meier, and J. M. Wahr (1992), Effect of melting glaciers on the Earth's rotation and gravitational field: 1965–1984, *Geophysical Journal International*, *108*(1), 1–15.

Voronoi, G. F. (1908), Nouvelles applications des paramètres continus à la théorie des formes quadratiques. Premier mémoire: Sûr quelques propriétés des formes quadratiques positives parfaits, *Journal für die Reine und Angewandte Mathematik*, *133*, 97–178, doi: 10.1515/crll.1908.133.97.

Wason, H. R., and S. J. Singh (1972), Static deformation of a multilayered sphere by internal sources, *Geophysical Journal International*, *27*(1), 1–14.

Wu, X., D. F. Argus, M. B. Heflin, E. R. Ivins, and F. H. Webb (2002), Site distribution and aliasing effects in the inversion for load coefficients and geocenter motion from GPS data, *Geophysical Research Letters*, *29*(24).

Wu, X., X. Collilieux, Z. Altamimi, B. Vermeersen, R. Gross, and I. Fukumori (2011), Accuracy of the International Terrestrial Reference Frame origin and Earth expansion, *Geophysical Research Letters*, *38*(13).

Wu, X., J. Ray, and T. van Dam (2012), Geocenter motion and its geodetic and geophysical implications, *Journal of Geodynamics*, *58*, 44–61.

Xu, C., and B. F. Chao (2015), Seismological versus geodetic reference frames for seismic dislocation: consistency under momentum conservations, *Geophysical Journal International*, *200*(2), 998–1002.

Zannat, U. J., and P. Tregoning (2017a), Estimating network effect in geocenter motion: Theory, *Journal of Geophysical Research: Solid Earth*, *122*, doi: 10.1002/2017JB014246.

Zannat, U. J., and P. Tregoning (2017b), Estimating network effect in geocenter motion: Applications, *Journal of Geophysical Research: Solid Earth*, *122*, doi: 10.1002/2017JB014247.

Zhang, X., and S. Jin (2014), Uncertainties and effects on geocenter motion estimates from global GPS observations, *Advances in Space Research*, *54*(1), 59–71.

Zhou, J., W. Sun, and J. Dong (2015), A correction to the article "Geo-center movement caused by huge earthquakes" by Wenke Sun and Jie Dong, *Journal of Geodynamics*, *87*, 67–73.

Zhou, J., W. Sun, S. Jin, H. Sun, and J. Xu (2016), Rotation change in the orientation of the center-of-figure frame caused by large earthquakes, *Geophysical Journal International*, p. 182.

Zou, R., J. T. Freymueller, K. Ding, S. Yang, and Q. Wang (2014), Evaluating seasonal loading models and their impact on global and regional reference frame alignment, *Journal of Geophysical Research: Solid Earth*, *119*(2), 1337–1358.